LABORATORY STUDIES OF ATMOSPHERIC REACTIONS USING INFRARED CAVITY RINGDOWN SPECTROSCOPY

Thesis by
Eva Rose Garland

In Partial Fulfillment of the Requirements
for the Degree of
Doctor of Philosophy

California Institute of Technology
Pasadena, California
2002
(Submitted August 14, 2001)

ACKNOWLEDGEMENTS

My memories of my graduate studies in the Okumura group will be dominated by all of the generous assistance that was extended to me throughout my time here. When I arrived at Caltech, I heard a rumor that the Okumura group was filled with the "nicest" people. Little did I know what an understatement that was. Mitchio is the source of this unique climate, as he routinely extends his untiring support and assistance late into the night and early in the morning; his enthusiasm for chemistry is addictive, and his dedication to us graduate students has given us a very rewarding graduate school experience. Mitchio's personality has shaped the group into what has been an enormous resource throughout my time here: whether it was Jim sacrificing 3 days to fix my dye laser; or Alex letting me borrow his crystals despite my propensity to break them; or Julio teaching me how to use the mill; or Claire sharing her expertise in kinetics and dedicating countless hours to helping me finish my thesis work; or Andrei loaning me practically everything in his lab; or Lance volunteering to drive a ridiculous number of miles for the Free Radicals Symposium; or the abundant assistance from Paul, Sam, and Jen; or conversations and advice from Sergei, David, Brian, and Fernando - everyone in this group has so freely given me the tools that have made my graduate school experience fruitful and enjoyable.

I am fortunate that all of my graduate work was in collaboration with Dr. Stan Sander at JPL. Stan's wealth of knowledge, enthusiasm, and support kept the project on target, as he always found ways to surmount the many obstacles we encountered.

I would like to extend a special thanks to Dr. Claire Morrell. From her I have learned a multitude about the dedication and determination necessary to complete a project. Much of the work presented in this thesis would not have been completed had it not been for Claire's guidance and assistance. I also thank Dr. Coleen Roehl for teaching me how to use FACSIMILE. For their expertise and helpfulness, I thank Mike, Ray, and Guy in the machine shop; Tom in the electronics shop; Dave Natzic at JPL; Rick in the Caltech glass shop; and Jurgen in the JPL glass shop.

I am indebted to my undergraduate advisor, the late Professor Brian Bent, for welcoming me into his lab as a freshman and for his guidance throughout my college years. Brian will always be an inspiration to me and to the many others whose lives he touched.

My family has given me the opportunity and self-confidence to reach for and fulfill my dreams. Thanks to my dad for teaching me electronics in a weekend, although I regret that I didn't inherit his natural aptitude for the subject! My mom has always been so wonderful at putting everything in perspective: the ups and downs of grad school were not quite so dramatic when I was able to see them through her eyes. My brother Harry has been more than a welcome email companion; he has taught me everything I know about computer programming. Although I don't have a chance to see them often enough, I would like to thank Roberta, Ken, and Brad for their love and support.

I cannot begin to express my appreciation to all of my friends who have supported me over these past few years, and I am grateful to all of them. Special thanks to Antonia, Denise, Tina, Lina, Greg, and the rest of the "softball team".

Christian - you know I could never put into words what you mean to me. As a husband, a teacher, and a friend, you have made each moment precious, each day extraordinary, and have filled my life with happiness. Thank you.

ABSTRACT

Infrared cavity ringdown spectroscopy provides for sensitive spectroscopic detection with a time scale of microseconds. This thesis discusses the implementation of infrared cavity ringdown spectroscopy for studies of atmospheric reactions.

Chapter 1 details the infrared cavity ringdown spectrometer assembled in our laboratory. Pulsed infrared radiation was generated by pumping an optical parametric amplifier (OPA) with 532 nm light from a doubled Nd:YAG laser, and a tunable dye laser provided the signal frequency. The ringdown decay was fit to an exponential curve to extract a ringdown time from which concentrations of absorbing species could be determined. Initial measurements indicated that our apparatus is a highly sensitive spectroscopic probe of infrared transitions of molecules with absorption linewidths greater than 1 cm^{-1}. Our detection limit for the j = 7 line of the ν_3 band of methane in a 43 inch cell was 10^{13} molec/cc of methane.

Chapter 2 describes initial kinetics experiments performed with our apparatus for the reactions of $HO_2 + HO_2$ and $HO_2 + ClO$. Our results for the rates of the $HO_2 + HO_2$ reaction and the $HO_2 + ClO$ reaction agree well with literature values, demonstrating the capabilities of our system for use in kinetic studies. We were unable to observe the formation of the postulated HOOOCl intermediate from the reaction of $HO_2 + ClO$ due to spectral interference from H_2O_2 in the region where HOOOCl is predicted to absorb.

Chapter 3 discusses studies of the reaction pathways undergone by alkoxy radicals. We found that photolysis of the alkyl nitrite precursor at 248 nm resulted in an unexpectedly high rate of decomposition of the alkoxy radicals, and we attributed this result to excess energy in the alkoxy radicals following photolysis at this wavelength.

With photolysis at 351 nm, no decomposition products were detected. At this wavelength, we observed an -OH peak at 3675 cm^{-1} for the n-butoxy and n-pentoxy radicals, which is evidence of the isomerization channel. For the n-butoxy radical, we determined that the ratio of the rate for its reaction with O_2 versus its isomerization (k_{O2}/k_{isom}) was $(4.0\pm0.1)*10^{-20}$ cm^3 $molec^{-1}$ when probing the isomerization product milliseconds after the generation of the n-butoxy molecule and $(3.6\pm1.4)*10^{-20}$ cm^3 $molec^{-1}$ when probing the isomerization product 10-20 μs after the generation of the n-butoxy radical. For the n-pentoxy radical, we placed an upper limit on the ratio of k_{O2}/k_{isom} of $5.6*10^{-21}$ cm^3 $molec^{-1}$.

TABLE OF CONTENTS

For Christian

CHAPTER 1

INFRARED CAVITY RINGDOWN SPECTROMETER

1.1 INTRODUCTION

Understanding the complex network of reactions in the earth's atmosphere is of utmost importance. Current areas of interest include quantifying the effect of anthropogenic emissions on the environment, controlling levels of stratospheric and tropospheric species such as ozone, and predicting future trends in the atmosphere. Atmospheric studies can be addressed on three fronts: 1) *in situ* detection of atmospheric species and reactions, 2) modeling studies, and 3) controlled kinetic studies in laboratory settings. These three approaches have proven to be complimentary, yielding abundant information about the atmosphere in recent years.[1]

One role of laboratory studies is to simplify the atmospheric reactions to a level in which quantitative information such as reaction rates and branching ratios can be garnered. Field studies can determine the concentrations and trends of various molecules in the atmosphere. Models can then be designed to incorporate the kinetic information obtained in laboratory studies in order to gain an understanding of the chemistry of species observed by the *in situ* studies. As models and *in situ* measurements improve, it is necessary to obtain more precise data from laboratory studies.

There are many challenges presented when one attempts to study atmospheric reactions in a laboratory setting. Some of the most reactive and chemically interesting species in the atmosphere are radicals that are created from the sun's photolysis of stable species. For example, the destruction of ozone in the stratosphere is a result of reactions with radicals such as Cl, ClO, OH, and NO. Due to the high reactivity of radicals, they can be difficult to prepare and study in a controlled manner. While it is often

advantageous to study a single radical-radical reaction in order to obtain unambiguous data, it is usually difficult to control side reactions undergone by these reactive species. Radicals may undergo reactions with many species present in the reaction mixture, such as with reactant precursors and reaction products, in addition to the reaction that is being studied. At lower pressures and lower radical concentrations, side reactions can be minimized; however, lower concentrations of radicals demand more sensitive detection techniques.

The work described in this thesis utilizes a highly sensitive laser spectroscopic method for probing atmospheric reactions in the laboratory called infrared cavity ringdown spectroscopy (IR-CRDS). Cavity ringdown is a powerful spectroscopic tool which has been used in a variety of applications.[3] The superior sensitivity of IR-CRDS, compared to traditional detection methods, has allowed us to extend this technique to the kinetic studies of atmospheric reactions and the detection of low concentrations of reactants, intermediates, and products.

1.2 OVERVIEW OF CAVITY RINGDOWN SPECTROSCOPY

Cavity ringdown spectroscopy (CRDS) is a method for obtaining high spectroscopic sensitivity on a timescale of microseconds. The technique was first reported by O'Keefe and Deacon in 1988,[2] and it has been successfully implemented for studies of low concentrations and weak spectroscopic transitions of molecules.[3,4,5] Cavity ringdown spectroscopy has been applied to a wide range of systems, such as detection of HCN overtones,[6] measurement of the absorption of methyl radicals[7] and water clusters[8],

and for kinetic studies of gas phase reactions.[9,10] CRDS has been implemented in wavelengths spanning the infrared, visible, and ultraviolet spectral regions.[4]

In traditional absorption spectroscopy, the amount of light absorbed by a sample is measured by subtracting the amount of light that passes through the sample from the amount of light that was sent into the sample. Beer's law can then be used to determine the concentration of a species with a known absorption coefficient. While this form of spectroscopy has been widely used, it is limited to cases in which sensitive measurements of the incident and output radiation can be made. When absorptions are very small ($\sim 10^{-4}$), other techniques must be used to obtain accurate absorption measurements. Direct absorption spectroscopy often is not sufficiently sensitive for studies of low concentrations of species or species with small absorption cross sections.

In cavity ringdown spectroscopy, mirrors are placed on both ends of the absorbing species, forming a highly reflective cavity. Light is injected into this cavity and bounces back and forth between the mirrors, with a small amount escaping on each pass (Figure 1.1). The energy of the output radiation decays exponentially, and the rate of the exponential decay is dependent on the reflectivity of the mirrors and on the amount of absorbance within the cavity. As absorption inside the cavity increases, the output signal will decay more quickly. A significant advantage of CRDS is that it is a direct absorption technique that does not rely on a knowledge of the energy of the incident radiation, since the only measured parameter is the rate of decay of the output radiation.

The ringdown time, τ, is defined as the time at which the ringdown signal has decayed to 1/e of its initial value. Straightforward algebra can relate τ to the reflectivity

(R) of the mirrors bordering an empty cavity (where c is the speed of light and L is the length of the cavity):

$$\tau = \frac{L}{c\,(1-R)}$$

Addition of an absorbing species between the ringdown mirrors modifies the above equation, so that if the mirror reflectivity is known, the absorbance (A) can be determined based on the ringdown time:

$$\tau = \frac{L}{c\,[(1-R) + A]}$$

In practice, one can determine the mirror reflectivities based on the ringdown time of an empty cavity of length L. Then, an absorbing species can be placed between the ringdown mirrors so that the value for A can be determined. The absorbance can be related to the molecule's cross section (σ) and concentration (c) with a known pathlength (L) with Beer's Law: $A=\sigma cL$. Therefore, if the absorption cross section is known for the species, then its concentration can be determined; conversely, a cross section can be extracted if the concentration of the species is known.

Scherer et al.[11] pioneered the use of CRDS in the infrared region (IR-CRDS), obtaining spectra of methane in the 3μm range. Subsequently, infrared CRDS was used to determine the absolute concentrations of water dimers, trimers, tetramers, and pentamers in a pulsed supersonic expansion by Paul and coworkers.[8] Recent applications of IR-CRDS include detection and characterization of alkyl peroxy radicals[12] and of alcohol clusters[13].

1.3 INFRARED CAVITY RINGDOWN SPECTROMETER

Our apparatus combined infrared cavity ringdown spectroscopy with a gas kinetics reaction cell in order to study reactions of importance in the stratosphere and troposphere. Absorption in the infrared was used to fingerprint the molecule(s) of interest, and the cavity ringdown spectrometer provided for highly sensitive detection of reactants, products, and intermediates. The kinetics cell facilitated the generation of radical reactants via photolysis of precursors by an excimer laser.

A. Generation of pulsed infrared radiation via optical parametric amplification

One disadvantage of cavity ringdown spectroscopy is that most of the incident light is lost as it is injected into the cavity through the front mirror. For example, if the mirrors are 99.99% reflective, then only 0.01% of the incident radiation will penetrate the mirror and enter the cavity. Therefore, a high-energy light source is needed to overcome the losses inherent in cavity ringdown. While high-energy pulsed lasers are commercially available in the visible and UV regions, they are not available in the mid-infrared region. Our experiments also required a light source that would be tunable over a broad range so that we could scan the infrared spectra of several molecules. To this end, we generated pulsed infrared radiation by building an optical parametric amplifier (OPA) which converted visible radiation into infrared radiation.

An OPA takes advantage of the optical properties of nonlinear crystals to convert a single photon of pump radiation into two photons, designated the signal and the idler, where the sum of the frequencies of the signal and idler is equal to the frequency of the

pump beam in compliance with the law of conservation of energy.[14] The pump radiation and small energies of the signal radiation are sent into the nonlinear crystal, and some of the pump photons are converted to photons at the signal and idler frequencies. In order for this conversion to occur, conservation of momentum dictates that vector addition of the momentum of the resultant signal and idler radiation must equal the momentum of the pump radiation.[15] Satisfying this condition is termed phase matching and can be achieved by manipulating the polarizations and input angles of the beams into the crystal, taking advantage of the asymmetry of the crystal's index of refraction. Our setup, based on the configuration reported by Reid,[14] used Type II phase matching, in which the polarizations of the pump beam and the idler beam are oriented parallel to the axis of crystal rotation (termed "ordinary"), and the polarization of the signal beam is oriented perpendicular to the axis of crystal rotation (termed "extraordinary"). A depiction of our OPA setup is shown in Figure 1.2.

We chose potassium titanyl phosphate (KTP) for our OPA crystals because KTP has a relatively high damage threshold (>250 MW/cm^2), and it does not absorb the idler frequencies that we required (2.5 - 3.5 microns). The crystals were cut at 44 degrees off the z-axis in the x-z plane; the face of the crystals were 7 mm x 7 mm, and they were 15 mm in length (Crystal Technologies). We used two KTP crystals in series in order to obtain a higher conversion of pump to signal and idler radiation. The angle of each KTP crystal was controlled with a stepper motor (Superior Electric Slo Syn MO61-LSO2E) mounted on a translation stage. A rod was attached to the top of the translation stage, and a spring was used to hold a 10 cm long lever in contact with the rod. The other end of

this lever was attached to ball bearings (Barden Precision) mounted to the crystal holder so that rotating the stepper motors provided for fine rotation of the KTP crystals.

A schematic of our experimental setup is shown in Figure 1.3. Our pump beam consisted of 532 nm radiation generated by doubling the output of a Nd:YAG laser (Spectra Physics GCR 130). Typical energies obtained were around 130 mJ for an 8 ns 532 nm pulse with the YAG running at 10 Hz. After exiting the YAG laser, the 532 nm beam passed through a quarter wave plate and a half wave plate before approximately 20% was diverted to pump a dye laser (Spectra Physics PDL3), which produced the signal radiation. Rotating the quarter and half wave plates adjusted the polarization of the 532 nm radiation, so that the amount of light that was sent to the dye laser could be controlled. The pump beam then passed through a delay line, the length of which was adjusted to optimize the temporal overlap of the pump and probe beams at the OPA. The polarization of the beam was then adjusted with another half wave plate so that it entered the OPA horizontal to the plane of the laser table (in keeping with the requirements for phase matching).

The dye laser produced the signal beam with vertical polarization and approximately 1 mJ of energy. With DCM {2-[2-[4-(dimethylamino)phenyl]ethenyl]-6-methyl-4H-pyran-4-ylidene]-propanedinitrile} dye, the output wavelength could be varied from 600 to 660 nm. After exiting the dye laser, the beam was reduced with telescoping optics to approximately half of its original size before it was combined with the 532 nm beam and sent into the OPA. Reducing the beam size, and thus increasing the intensity per unit area of the beam, was found to improve the conversion efficiency of the

OPA. We decided not to reduce substantially the size of the pump beam because the high energy of this beam could damage the KTP crystals if it were focused too tightly.

With typical input energies of 110 mJ of 532 nm light and 1 mJ of 632 nm light, our OPA produced approximately 0.5 - 1.5 mJ of infrared radiation. The output energy fluctuated throughout the day and was very sensitive to the exact orientation of the beams entering the KTP crystals. As the YAG laser warmed up throughout the day, the conversion efficiency tended to increase even though the output energy of the YAG laser remained constant. This is likely a result of a changing transverse mode pattern of the YAG laser as a function of temperature. Therefore, we typically allowed the YAG to warm up for one to two hours before beginning experiments.

The linewidth of the output radiation from an OPA is limited by the larger of the linewidths of the pump or signal beam. Generally, our experiments did not require narrow linewidth infrared radiation, and so we did not seed the YAG laser. The PDL3 dye laser specifies a linewidth of 0.07 cm^{-1}. The linewidth of the unseeded YAG laser was approximately 1 cm^{-1}, and thus the linewidth of the infrared radiation was approximately 1 cm^{-1}. When the YAG laser was seeded, its linewidth was narrowed to approximately 0.1 cm^{-1}, but the energy of the YAG was reduced by 20-30%, and the OPA was operating near its threshold for conversion. It was therefore difficult to obtain enough infrared radiation to observe a ringdown signal. Recently, replacement of the YAG flashlamps has increased the energy of the YAG laser by approximately 20%, and so performing CRDS experiments with the seeded YAG laser will be a viable option for future experiments.

Visual Basic programs were written to move the two stepper motors that controlled the angles of the OPA crystals and the stepper motor that controlled the dye laser wavelength. The stepper motors controlling the OPA crystal angles were interfaced to the computer with a Keithley Instruments PIO-12 Digital I/O board, and the stepper motor controlling the dye laser wavelength was computer-interfaced with a Keithley 1800HR Data Acquisition board. The 1800HR was more reliable than the PIO-12, but it did not have enough output ports for all three stepper motors. (Each stepper motor required two signals: one to control the direction of movement, and one to supply the steps.)

The relationship between the dye laser wavelength and the angle the KTP crystals required for maximum IR conversion at each wavelength was found empirically to be linear for our wavelength range. Therefore, a program was written to automatically adjust the angles of the crystals whenever the wavelength of the dye laser was adjusted. The computer interface allows the user to adjust the "b" value of the $y = mx + b$ equation used in the correlation of the dye wavelength and the stepper motor, where y is the crystal position (arbitrary units), m is the empirically-determined slope, and x is the dye wavelength in units that appear on the dye laser dial (40 * the wavelength in nm). Typical values for m and b were -55 and 1,000,000, respectively. The values for b required large adjustments whenever the OPA hardware was altered.

B. Ringdown Cavity

After passing through the OPA, the green and red beams were picked off with two sapphire optics with AR coating centered at 532 nm and 630 nm, respectively.

Remaining traces of the red and green light were eliminated by passing the beams through a polished silicon optic placed at Brewster's angle (74 degrees) so as to allow for maximum transmission of the IR light. The infrared light was then directed into the ringdown cavity with a 45 degree mirror. We found that with a longer ringdown cell, it was helpful to loosely focus (100 cm FOC CaF_2 lens) the light into the cavity. However, with shorter cells of approximately 30 inches in length, focusing the light into the cavity did not make a noticeable difference in the intensity or profile of the ringdown signal.

For the experiments reported here, we used ringdown mirrors whose reflectivity was centered at 2.7 microns (Los Gatos Research). Good reflectivity of $> 99.99\%$ was obtained from 2.5 through 3.0 microns, and typical ringdown times for an evacuated 50 cm cell were on the order of 10 microseconds. We also obtained a set of mirrors with peak reflectivity centered at 3.3 microns which were used in initial sensitivity determinations. The ringdown mirrors required cleaning approximately once a week while running experiments. The procedure for cleaning the mirrors was to remove them from their mounts, blow air over them to remove particulate matter, and then to wipe them carefully with lens paper and drops of methanol followed by acetone. (The final rinse with acetone removes residue that can remain after the methanol washing.)

The mirror mounts, also purchased from Los Gatos Research, were compatible with our vacuum cell as the mirrors were mounted against an o-ring and could be angle-tuned with three adjustment screws. Stainless steel holders were machined so that the mirrors were situated seven inches above the laser table, which corresponded to the height of the laser beams. Holes were drilled and tapped into the sides of the mirror

mounts so that we could purge the ringdown mirrors with inert gas to prevent reactive chemicals from reaching and damaging the mirror surfaces.

The ringdown mirrors were aligned by sending the infrared radiation through two irises that were placed several inches apart in front of the InSb detector. Then a HeNe laser was sent through the irises so that we could visualize the pathway taken by the IR. The rear ringdown mirror was placed a few inches in front of the InSb detector with the HeNe light hitting the middle of the mirror, and the angle of the mirror was adjusted so that the HeNe radiation was reflected directly back into the HeNe laser. Next, the front ringdown mirror was situated and adjusted so that the reflection of the HeNe off the back of this mirror was directed back to the HeNe laser. At this point, the two ringdown mirrors were aligned parallel to each other and perpendicular to the path of the incident IR radiation.

When the ringdown cavity was pumped out so that low-pressure experiments could be performed, the vertical tilt of the mirrors needed to be adjusted by approximately 1/8 turn of the vertical adjustment screw. It was often challenging to align the mirrors so that all of the light was collected by the detector. When only some of the transverse modes of the ringdown signal were collected, the ringdown signal oscillated as it decayed. The primary method for eliminating the oscillations was to realign the ringdown mirrors, and when this did not correct the problem, other IR optics typically needed adjustments.

C. Gas Kinetics Cell

Several iterations of gas kinetics cells were used in our apparatus, based on the demands of the experiments. The simplest cells consisted of a single quartz tube of 17 - 30 inches in length with a one inch diameter (Figure 1.4). A one inch diameter was necessary for the cells so that the IR radiation would not be clipped by the cell walls as it passed back and forth between the ringdown mirrors. Ports with teflon valves connecting to the vacuum pump (Welch 1398, 53 cfm), the Baratron (MKS 1000 Torr), and the thermocouple gauge (Varian) were inserted into the ends of the cell. The thermocouple gauge measured pressures of 1-2000 mTorr and was used to check for leaks in the cell. Measurements of the cell pressures used for our experiments of approximately 50-700 Torr were facilitated by the Baratron. Gases were introduced into the cell via a manifold oriented perpendicular to the main cell and connected to the cell with an o-ring seal. The ringdown mirror mounts were fitted with metal-to-glass seals terminating in a glass o-ring joint which then could be connected to either end of the main cell.

A more complex cell was built to achieve low temperatures (Figure 1.5). This cell had three jackets: reactants were introduced into the inner tube; the middle tube contained the methanol coolant, and the outer tube served as a vacuum jacket to prevent frosting on the outside of the cell. Construction of the cell was simplified by placing the vacuum jacket around only the photolysis region of the cell. The coolant jacket was extended upward toward the gas inlets to ensure that the gases had sufficient time to reach thermal equilibrium before entering the experimental region. In regions where the coolant jacket was not enclosed by the vacuum jacket, insulation was required to prevent buildup of frost while running the experiments at low temperature. Additionally, it was

necessary to purge the outside of the cell in the photolysis region with dry air generated with a compressed air dryer (Balston Model 75912-BX) to prevent condensation. A chiller (FTS Systems Model MC-A-80A-1) controlled the temperature of the methanol coolant, and temperatures as low as -80°C could be achieved.

Before being introduced into the cell, the gases passed through mass flow meters (Edwards-831 10sccm, 100sccm, 1slm, and 5slm models), and their flow rates were controlled with needle valves (Swagelok). A Visual Basic program interfaced with a data acquisition board (Keithley 1800HR) provided for computer readout of the flow rates and automatically adjusted for the different calibrations of the various gases used in our experiments. The gas lines consisted of 1/4" stainless steel, copper, or teflon tubing, and Swagelok fittings were used for all metal joints. The gas lines were joined to 1/4" ports on the glass manifold with either teflon Swagelok or Ultratorr fittings.

Our experimental conditions typically called for approximately 4000 sccm of total gas flow and a cell pressure of around 400 Torr. Since the gas flow pathlength within the 1 inch diameter cells ranged from 15 to 30 inches, the calculated and experimentally observed residence time of the gases in the cell was on the order of 0.5 to 1 second. Therefore, we normally used repetition rates between 1-2 Hz so that the cell would be thoroughly flushed between experiments.

D. Photolysis

The reactions that we chose to study generally required radical reactants, as radical species are some of the most reactive and chemically important species in the troposphere and stratosphere. Because lifetimes of radicals are often very short, and

since they are extremely reactive, it can be difficult to prepare them and then flow them into a kinetics cell without substantially depleting the desired reactant and possibly complicating the reaction to be studied by introducing unwanted impurities into the cell along with the reactant. Therefore, we chose to photolyze stable precursors *in situ* while the precursor gases were in the cell so that we could generate radical reactants and probe the reactions immediately afterwards in order to minimize the adverse effects of side reactions on the reliability of our data.

We photolyzed species such as O_3, Cl_2O, and alkoxy nitrites at 248 nm or 351 nm with the output beam from a Lambda Physik EMG 101-104 MSC excimer laser. The excimer laser generally produced 250 mJ of energy per shot at 248 nm and 100 mJ at 351 nm. The laser was evacuated and filled with the appropriate mixture of Ne/Kr/F (248 nm) or Ne/Xe/F (351 nm) approximately every two weeks to maintain satisfactory pulse energies.

Mirrors were used to elevate the excimer beam above the reaction cell and then send the beam vertically down into the cell through the optically transparent quartz cell walls. For some experiments, a negative focal length cylindrical lens was placed in the excimer beam's path shortly before it entered the cell in order to expand the beam along the axis of the cell. This provided for a larger photolysis region that was rectangular in shape and approximately 10 cm x 0.5 cm. By expanding the excimer beam, we were able to photolyze a relatively large number of molecules without creating a region in which excessively high concentrations of radicals could lead to side reactions. For experiments where the precursor photolysis cross sections were relatively small, we did not expand

the excimer beam in order to achieve a high intensity of UV light in the cell so that we could generate a desired amount of radical reactants.

E. Data Acquisition and Processing

The output light from the ringdown cavity was focused onto an InSb detector (EG&G Judson) with a 2 inch focal length CaF_2 lens, and the signal was amplified by passing it through a series of two Comlinear CLC401 and CLC425 OpAmps, resulting in a gain of approximately 100. Excessive noise was introduced into the signal when we attempted to use commercial OpAmps that required 120V AC power, despite efforts to filter the input AC power, and so it was necessary to use the CLC amplifiers. The amplified signal passed through a high frequency filter (cut off frequency = 62 GHz) and a ferrite choke before it was sent to an oscilloscope (Tektronix TDS 3032). A GPIB interface (National Instruments) was used to connect the scope to a computer.

TTL pulses from two digital delay generators (SRS model DG535 and EG&G Princeton Research Model 9650) were used to synchronize the timing of the lasers and the data collection. The two DDGs were necessary because the YAG performed optimally while operating at 10 Hz, and so the EG&G DDG always operated at 10 Hz, and the SRS DDG operated at the repetition rate needed for the current experiment. A diagram of the timing scheme used in our experiments is shown in Figure 1.6. An initial pulse was sent from the EG&G DDG to the SRS DDG. At a specified delay time, a pulse was sent from the SRS DDG to fire the excimer laser. This pulse was also sent to inhibit the excimer from charging until shortly before it would fire again, which extended the lifetime of the excimer and alleviated some of the noise that was present while ringdown

curves were acquired. Two additional pulses were sent from the EG&G DDG to the YAG laser, spaced 180 microseconds apart. The first pulse charged the flashlamps, and the second pulse triggered the Q-switch. A fourth pulse was sent from the SRS DDG to trigger the oscilloscope so that it would begin data collection. The relative timing between the excimer pulse and the other pulses determined the time delay between the preparation of reactants (via photolysis) and the probing of reactants, reaction intermediates and products with infrared cavity ringdown spectroscopy.

A Visual Basic program was written to collect the ringdown curves, fit them to an exponential decay, and determine the ringdown time. Typically, between 8 and 32 ringdown curves were averaged on the scope before being sent to the computer. The Visual Basic Program then used a Levenberg-Marquardt algorithm, translated from a Fortran program,[16] to fit the exponential curve and determine the ringdown time. The curve and the fit parameters were then saved as a comma delimited (.csv) file in the directory ringdown.spectra, and the file was named based on the current date followed by the lowest letter that was not currently in use for that day (e.g. 040501f.csv). A plot of a representative ringdown curve and its calculated fit are shown in Figure 1.7.

Scanning over several cm^{-1} was also facilitated by the Visual Basic program. With the user-entered initial and final cm^{-1} values and the step size, the program obtained a ringdown curve at the initial value, moved the dye laser and OPA crystals to the new setting, obtained another ringdown curve, and repeated this routine until it reached the final cm^{-1}. These files were saved with an "s" preceding the current date and the lowest available letter alphabetically (e.g. s040501f.csv).

In obtaining kinetic data, it was necessary to obtain ringdown curves at varying time delays between the excimer laser (preparation of reactants) and the YAG laser (probe) to determine the concentrations of species as a function of time. Therefore, a routine was written to enable the user to enter the initial and final delay times at which ringdown curves were desired as well as the time difference between subsequent delay scans. The time difference could be linear (i.e. 2, 4, 6, 8, ... milliseconds) or could grow as an exponential term (e. g. 2, 4, 8, 16, ... milliseconds for a squared term). Analogous to the scan files, these delay files were saved with a "d" preceding the current date and the lowest available letter.

A schematic of the various devices used in this experiment that are controlled with Visual Basic programming is depicted in Figure 1.8. The convenience of being able to cater the interface program to our specific needs led us to write our own programs in Visual Basic, rather than purchasing a pre-packaged option. Future modifications to the program can be made expediently in the Visual Basic Programming environment.

F. Signal-to-Noise Considerations

The noise in our baseline signal was limited by the digitization of the data points with our oscilloscope. The oscilloscope digitized at 9 bits, and we typically averaged 16 shots on the oscilloscope before transferring the data to the computer. The oscilloscope screen contained 8 divisions, and its smallest scale was 1 mV / division. With these parameters, the smallest distinguishable increment by the oscilloscope was $2*10^{-6}$ mV. The standard deviation of a set of baseline points for the 1 mV / division scale was found to be $7*10^{-7}$ mV. As the scale of the oscilloscope was changed, the standard deviation of

a set of baseline points was found to rise considerably, so that at the 200 mV / division scale, the standard deviation was an order of magnitude larger than it was at the 1 mV / division scale. A plot of the standard deviation of a set of baseline points as a function of the scale of the oscilloscope is shown in Figure 1.9. As the scale of the oscilloscope was increased, the standard deviation of the baseline points increased, implying that digitization was indeed limiting our resolution. Current work is underway to increase the resolution of our data collection by switching to a 12-bit A/D converter in order to minimize the digitizing noise that is evident in Figure 1.9.

Typical maximum signal voltage after amplification of the ringdown curves ranged from 20 mV to 200 mV. The ringdown curves were fit to a single exponential decay ($y = a*e^{bx}$) as described in the previous section. The variance of the fit from the actual ringdown curve taken in an evacuated cell was investigated by subtracting an actual ringdown trace from its fitted exponential curve, and the result of four such residual plots are shown in the top chart of Figure 1.10. The ringdown curves were then fit using a bi-exponential formula, $y = a*e^{bx} + c*e^{dx}$, and the residuals for the bi-exponential fits are shown in the bottom chart in Figure 1.10. The similarity in the residual spectra for the single exponential and bi-exponential fits suggests that the bi-exponential fit is not a significantly better representation of the actual data than the single exponential fit.

We found that the most important factor in obtaining close fits to the actual data was the alignment of the IR beam into the ringdown cell. The factors involved in achieving a good alignment (defined as a signal whose ringdown curve that is fit well with a single exponential decay) include sending the IR beam through the center of the

front ringdown mirror and ensuring that it exits through the center of the rear mirror; aligning the ringdown mirrors so that they are parallel to each other and perpendicular to the path of the incident IR beam; and adjusting the position of the 2 inch FOC lens in front of the InSb detector to ensure that all of the light that exits the rear ringdown mirror is collected by the detector. Focusing the IR beam prior to sending it into the ringdown cavity had little effect on the quality of the ringdown decay. However, spatial filtering the incident beam produced a slightly better ringdown decay. Unfortunately, spatial filtering resulted in a significant loss of beam energy, and so it was not practical to spatially filter the IR beam before sending it into the ringdown cavity.

1.4 PROOF OF CONCEPT EXPERIMENTS

A. Methane detection

For an initial calibration experiment, we obtained the spectrum of the ν_3 band of methane centered at 3017 cm^{-1}. With 0.1 Torr of methane in the 30 inch long ringdown cell, the Q branch of the methane spectrum was saturated and the rotational lines could be clearly observed (Figure 1.11) For this data, 32 scans were averaged by the scope at each wavelength before the averaged decay curve was sent to the computer. The primary purpose of this experiment was to calibrate the wavelength of our infrared radiation in relation to the counter on the dye laser. By fitting our data to HITRAN spectra, we were able to obtain an empirical relationship between the dye counter setting and the true infrared wavelength:

$$(\text{wavelength in } cm^{-1}) = 10^7 * \{(1 / 532) - [40 / (\text{counter setting} - 12.5)]\}$$

The secondary purpose of the methane experiments was to obtain an estimate of our apparatus' sensitivity. The standard deviation of the ringdown time for a single point was approximately 1% of the value for the ringdown time. This was determined by taking several consecutive ringdown signals and determining the standard deviation of their values. For the methane spectrum in Figure 1.11, the standard deviation for the baseline inverse ringdown time was 3000 s^{-1}. The signal for each of the rotational lines was approximately 200000 s^{-1} larger than the baseline ringdown time. Thus, for a signal to noise of approximately 1, the lower limit of methane concentration for which we can identify the P and R branches is 0.001 Torr, corresponding to $3*10^{13}$ molecules/cc. Our sensitivity for the Q branch of methane is expected to be significantly better than this since the individual lines of the Q branch have larger cross sections and are more densely spaced than in the P and R branches. We did not pursue the limits of our sensitivity for the Q branch of methane since it was difficult to measure very small amounts of methane in the reaction cell, and for small concentrations of methane, the Q branch was quickly saturated.

B. HCl Detection

The initial system that we had aimed to study with our CRDS apparatus was the branching ratio of the HCl product from the reaction of OH + ClO. Reactive chlorine molecules, such as Cl and ClO, are implicated in ozone destruction, and HCl is a chlorine reservoir that serves to trap the chlorine in a less reactive form. The OH + ClO reaction is important in determining the relative amounts of reactive and unreactive chlorine in the stratosphere, and it is believed to have two product channels: HO_2 + Cl is the major

channel, and HCl + O_2 is thought to be a minor channel (Reaction 1.1 and Reaction 1.2).[17,18,19]

$$OH + ClO \rightarrow HO_2 + Cl \quad (1.1)$$

$$OH + ClO \rightarrow HCl + O_2 \quad (1.2)$$

An HCl channel from the reaction of OH + ClO could be an important mechanism for removing reactive chlorine from the stratosphere, which would lead to a decrease in the rate of ozone destruction.

Before studying the OH + ClO reaction, we attempted to detect HCl at 3.3 microns with our IR-CRDS apparatus. However, we did not observe any decrease in ringdown time with as much as $3*10^{15}$ molecules/cc of HCl in our cell. We determined that the reason we could not detect HCl is because the linewidth of HCl under our conditions (~.01 cm^{-1}) is approximately a factor of 100 narrower than our laser linewidth of 1 cm^{-1}. Thus, even if we were to saturate the transition of HCl, it would only have a minimal effect on our ringdown curve. In fact, if the narrow band of radiation corresponding to the linewidth of HCl was completely absorbed by the HCl on the first several passes of the radiation through the ringdown cell, the resultant change in the ringdown curve would only occur over the first few points on the exponential decay. Nearly the entire exponential decay that we would be fitting would be a result of the nonabsorbing radiation.

We then seeded the YAG laser so that our laser linewidth of 0.1 cm^{-1} would be reduced to a factor of 12 larger than the HCl absorption. Seeding the YAG laser reduced our infrared energy by approximately a factor of 10, leading to a low signal to noise ratio for our ringdown curves. With the seeded YAG laser, we were still unable to observe

any absorption due to HCl. Had we been able to increase the energy of our probe light, we may have been able to observe a small amount of HCl absorption, however, we realized that if it would be difficult to see an absorption from 10^{15} molecules/cc of HCl, it would be extremely challenging to observe the 10^{9} molecules/cc that we expected to generate from our proposed OH + ClO reaction conditions.

According to Zalicki and Zare,[20] cavity ringdown spectroscopy leads to an exponential decay only when the laser linewidth is much narrower than the linewidth of the absorption. In our attempts to detect HCl, our laser linewidth was much broader than the HCl transition, and so an important factor in the high sensitivity of CRDS was not satisfied. The long timescale for detection skewed our results so that we were mainly collecting non-absorbed radiation outside of the narrow transition of the HCl molecule. Because of the difficulties associated with our laser linewidth being significantly broader than the HCl transition, we concluded that our apparatus was not well-suited to HCl detection.

C. Conclusions regarding the optimal systems to study with our IR-CRDS apparatus

Our proof of concept experiments have confirmed that our apparatus is a highly sensitive spectroscopic probe of infrared transitions. Sensitivity measurements indicate that we can detect the rotational lines of methane with 10^{13} molecules/cc of methane, and our expected sensitivity for the Q branch of methane is significantly higher since the Q branch consists of stronger absorption bands spaced more closely together.

Based on the difficulties we faced when attempting to detect a narrow-linewidth species (HCl), we have concluded that our IR-CRDS apparatus functions optimally when implemented for the detection of molecules with absorption linewidths greater than one cm^{-1}. When the absorption linewidth is narrower than our laser linewidth, the ringdown signal is dominated by the portion of the light that is not absorbed by the molecule. An advantage of our apparatus is that it is broadly tunable over a range limited only by the reflectivity of our ringdown mirrors (approximately 600 cm^{-1} with a single set of mirrors), and so it is an excellent probe of molecules with broad absorption features.

1.5 REFERENCES

[1] Scientific Assessment of Ozone Depletion: 1998. Washington, DC: National Oceanic and Atmospheric Administration : National Aeronautics and Space Administration; Nairobi, Kenya: United Nations Environment Programme; Geneva, Switzerland: World Meteorological Organization; Brussels, Belgium: European Commission (1999).

[2] A. O'Keefe and D. A. G. Deacon, *Rev. Sci. Instrum.*, **59 (12)**, 2544 (1988).

[3] J. J. Scherer, J. B. Paul, A. O'Keefe, R. J. Saykally, *Chem. Rev.* **97**, 25 (1997), and references therein.

[4] G. Berden, R. Peeters, G. Meijer, *Int. Rev. Phys. Chem.*, **19 (4)**, 565 (2000).

[5] M. D. Wheeler, S. M. Newman, A. J. Orr-Ewing, M. N. R. Ashfold, *J. Chem. Soc. Farad. Trans.*, **94 (3)**, 337 (1998).

[6] D. Romanini and K. K. Lehmann, *J. Chem. Phys.*, **99**, 6287 (1993).

[7] P. Zalicki, Y. Ma, R. N. Zare, E. H. Wahl, J. R. Dadamio, T. G. Owano, C. H. Kruger, *Chem. Phys. Lett.*, **234**, 269 (1995).

[8] J. B. Paul, C. P. Collier, R. J. Saykally, J. J. Scherer, A. O'Keefe, *J. Phys. Chem.*, **101**, 5211 (1997).

[9] T. Yu and M. C. Lin, *J. Am. Chem. Soc.*, **155**, 4371 (1993).

[10] D. B. Atkinson and J. W. Hudgens, *J. Phys. Chem. A*, **101**, 3901 (1997).

[11] J. J. Scherer, D. Voelkel, D. J. Rakestraw, J. B. Paul, C. P. Collier, R. J. Saykally, A. O'Keefe, *Chem. Phys. Lett.* **245**, 273 (1995).

[12] M. B. Pushkarsky, S. J. Zalyubovsky, T. A. Miller, *J. Chem. Phys.*, **112 (24)**, 10695 (2000).

[13] R. A. Provencal, R. N. Casaes, K. Roth, J. B. Paul, C. N. Chapo, R. J. Saykally, G. S. Tschumper, H. F. Schaefer, *J. Phys. Chem. A*, **104**, 1423 (2000).

[14] S. Reid, *Appl. Optics* **35(9)**, 1473 (1996).

[15] A. Yariv, Optical Electronics (Fourth Edition), Saunders College Publishing (1991).

[16] W. H. Press, S. A. Teukolsky, W. T. Vetterling, and B. P. Flannery, Numerical Recipes in Fortran (Second Edition), Cambridge University Press (1992).

[17] J. B. Lipson, M. J. Elrod, T. W. Beiderhase, L. T. Molina, M. J. Molina, *J. Chem. Soc. Farad. Trans.* **93 (16)** 2665 (1997).

[18] J. B. Lipson, T. W. Beiderhase, L. T. Molina, M. J. Molina, M. Olzmann, *J. Phys. Chem. A* **103 (33)**, 6540 (1999).

[19] H. A. Michelson, R. J. Salawitch, M. R. Gunson, C. Aellig, N. Kampfer, M. M. Abbas, M. C. Abrams, T. L. Brown, A. Y. Chang, A. Coldman, F. W. Irion, M. J. Newchurch, C. P. Rinsland, G. P. Stiller, R. Zander, *Geophys. Res. Lett.* **23 (17)**, 2361 (1996).

[20] P. Zalicki and R. N. Zare, *J. Chem. Phys.* **102 (7)**, 2708 (1995).

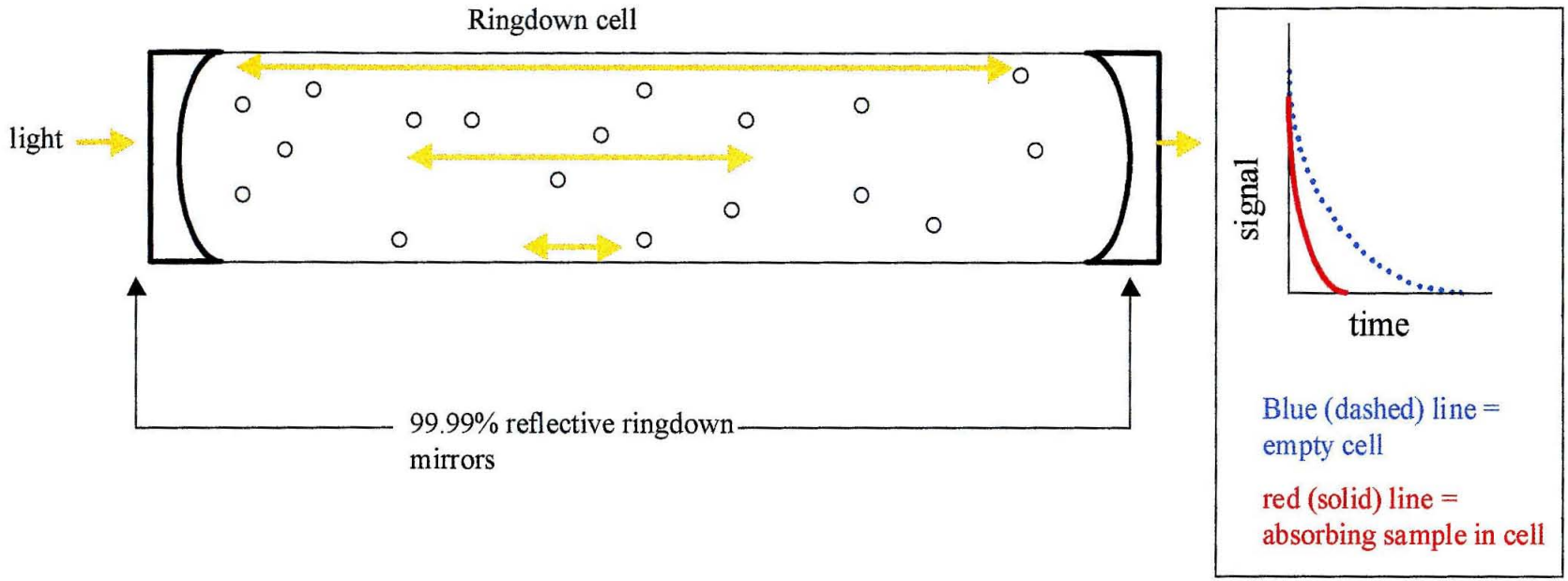

Figure 1.1. Depiction of cavity ringdown spectroscopy. Light enters the cavity and is reflected by the ringdown mirrors. A small amount of light escapes on each pass, and the rate of decay of the output light is dependent on the reflectivity of the mirrors and on the absorption of light by species in the cell.

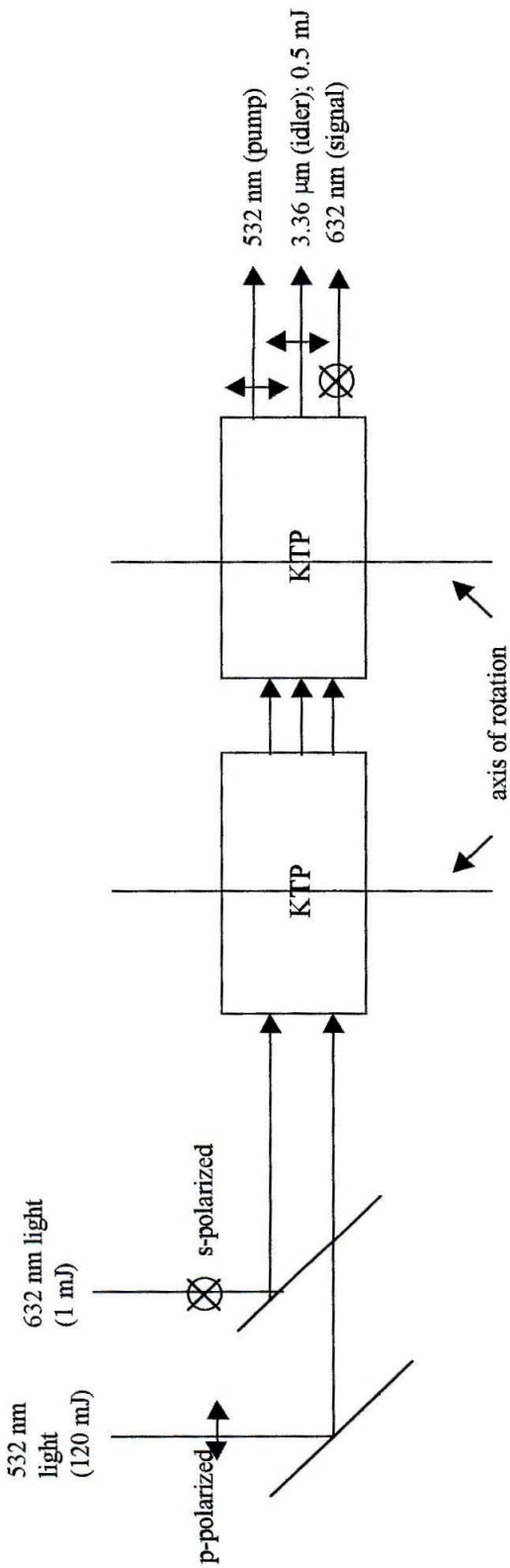

Figure 1.2. OPA setup to generate pulsed infrared radiation.

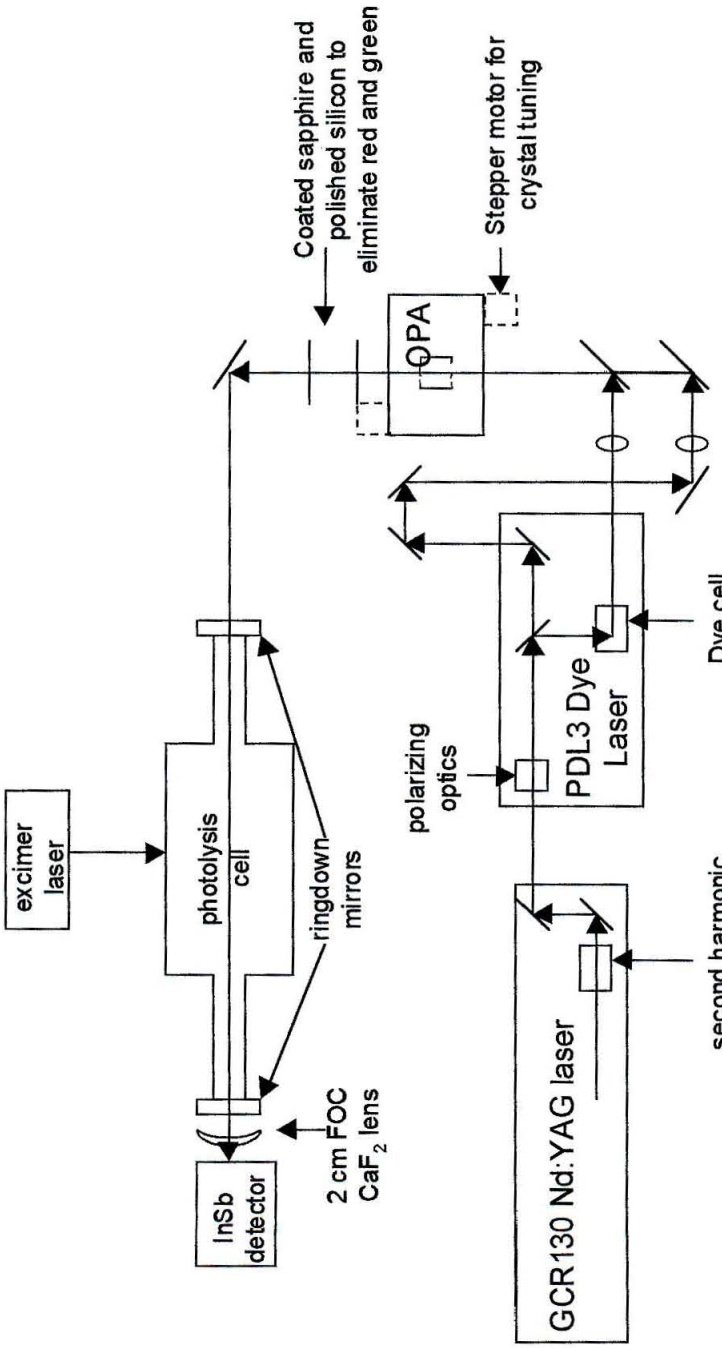

Figure 1.3. Experimental setup for infrared cavity ringdown spectroscopy.

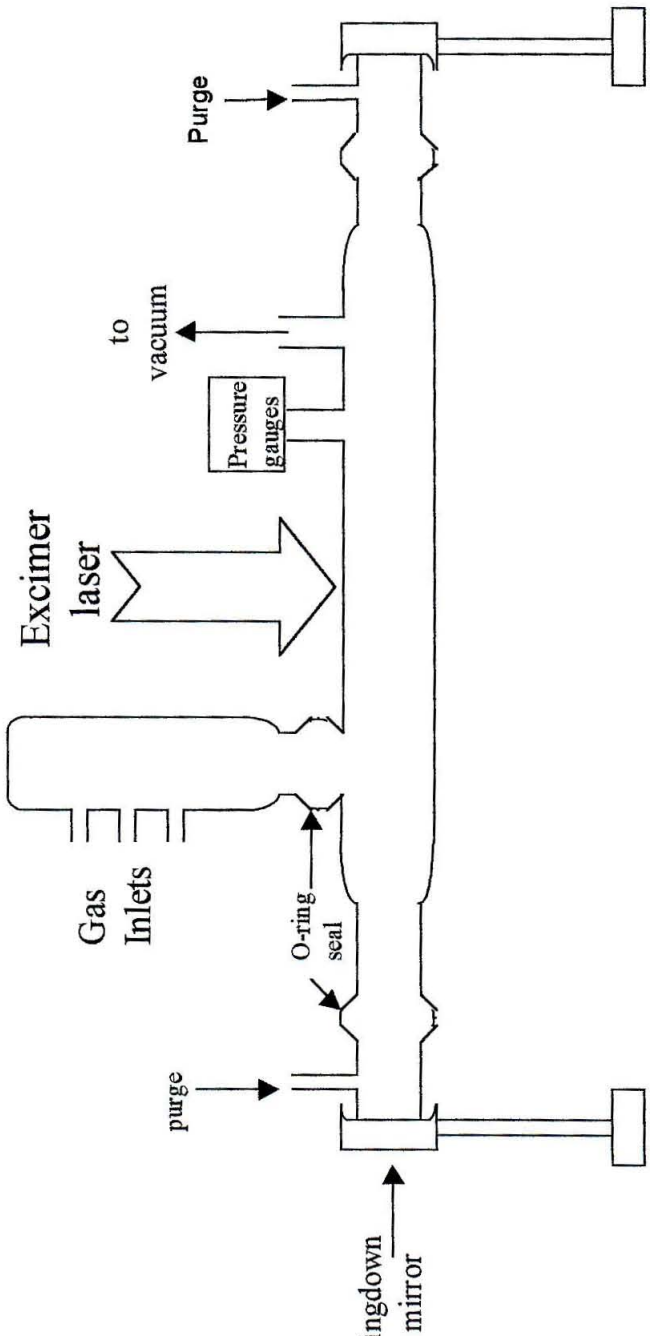

Figure 1.4. Infrared kinetics cell used for room temperature experiments.

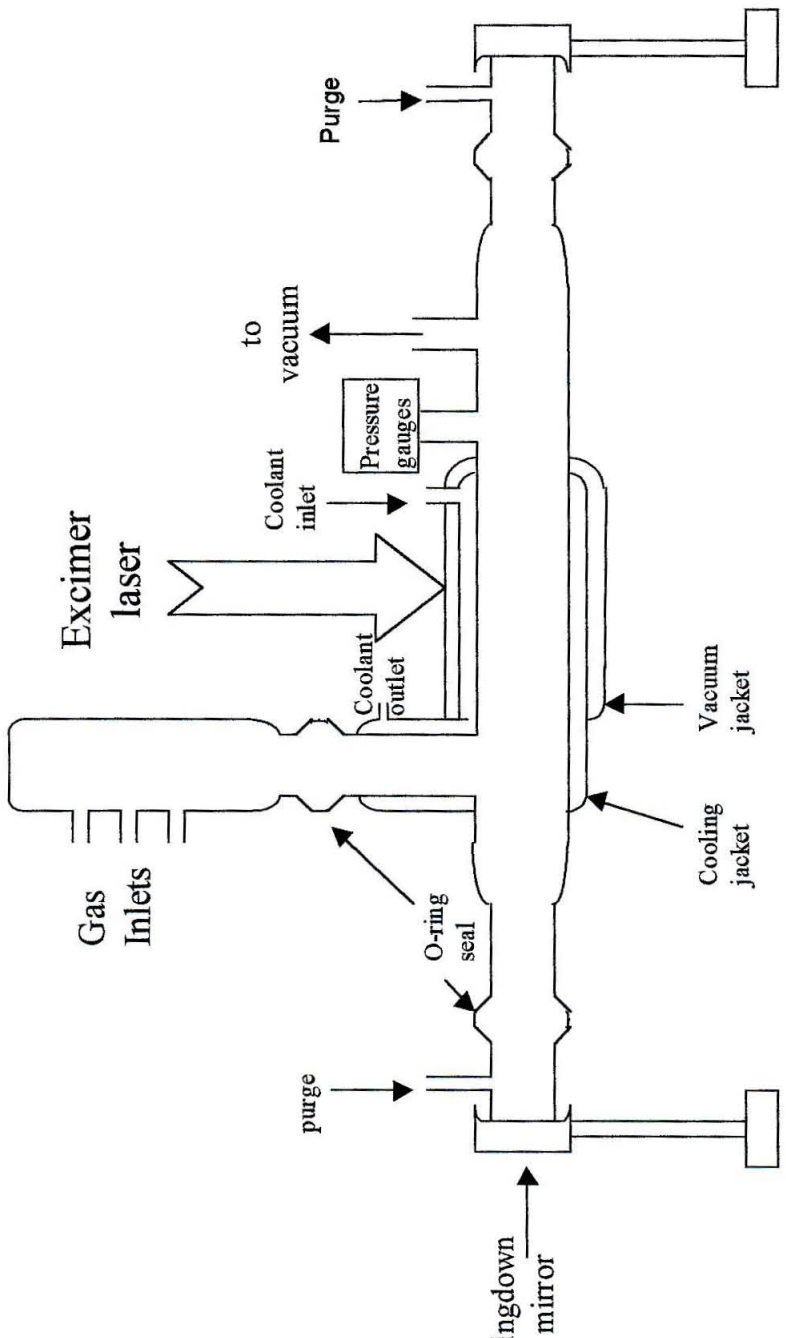

Figure 1.5. Cooled infrared kinetics cell used for experiments ranging from 193 K to 300 K.

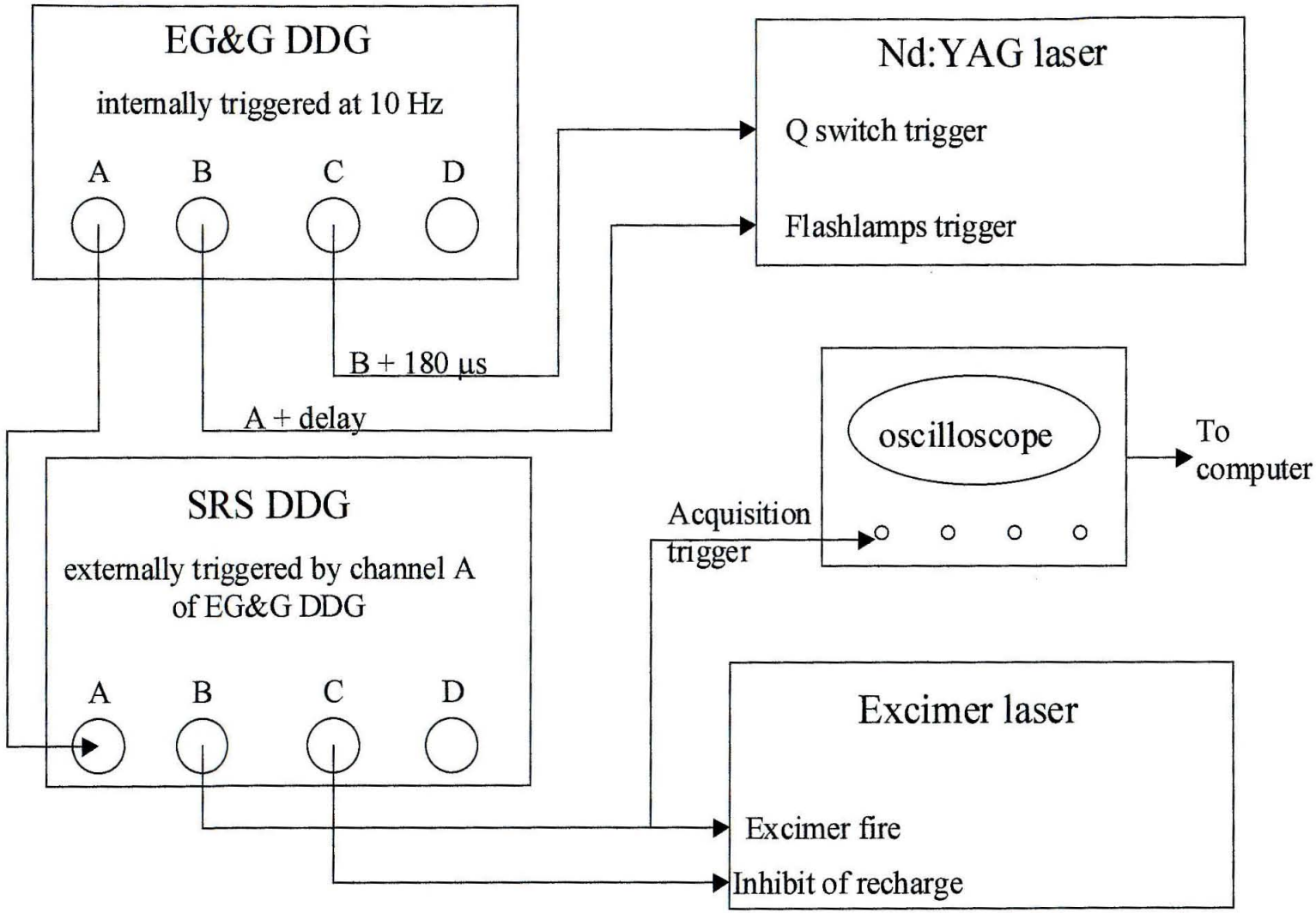

Figure 1.6. Diagram of timing synchronization for IR-CRDS experiments.

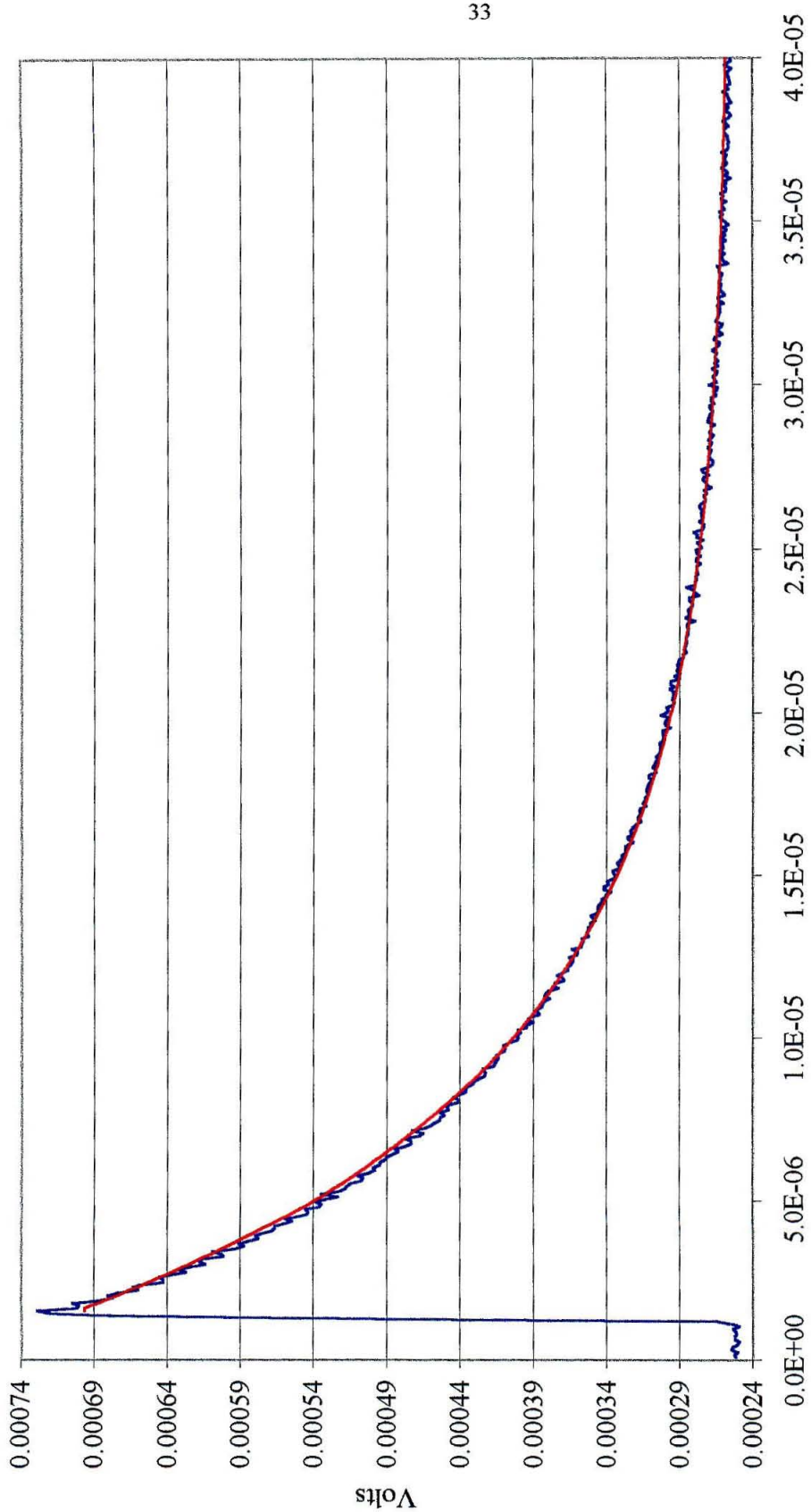

Figure 1.7. Representative experimental ringdown decay (blue) of an empty cell and fit (red).

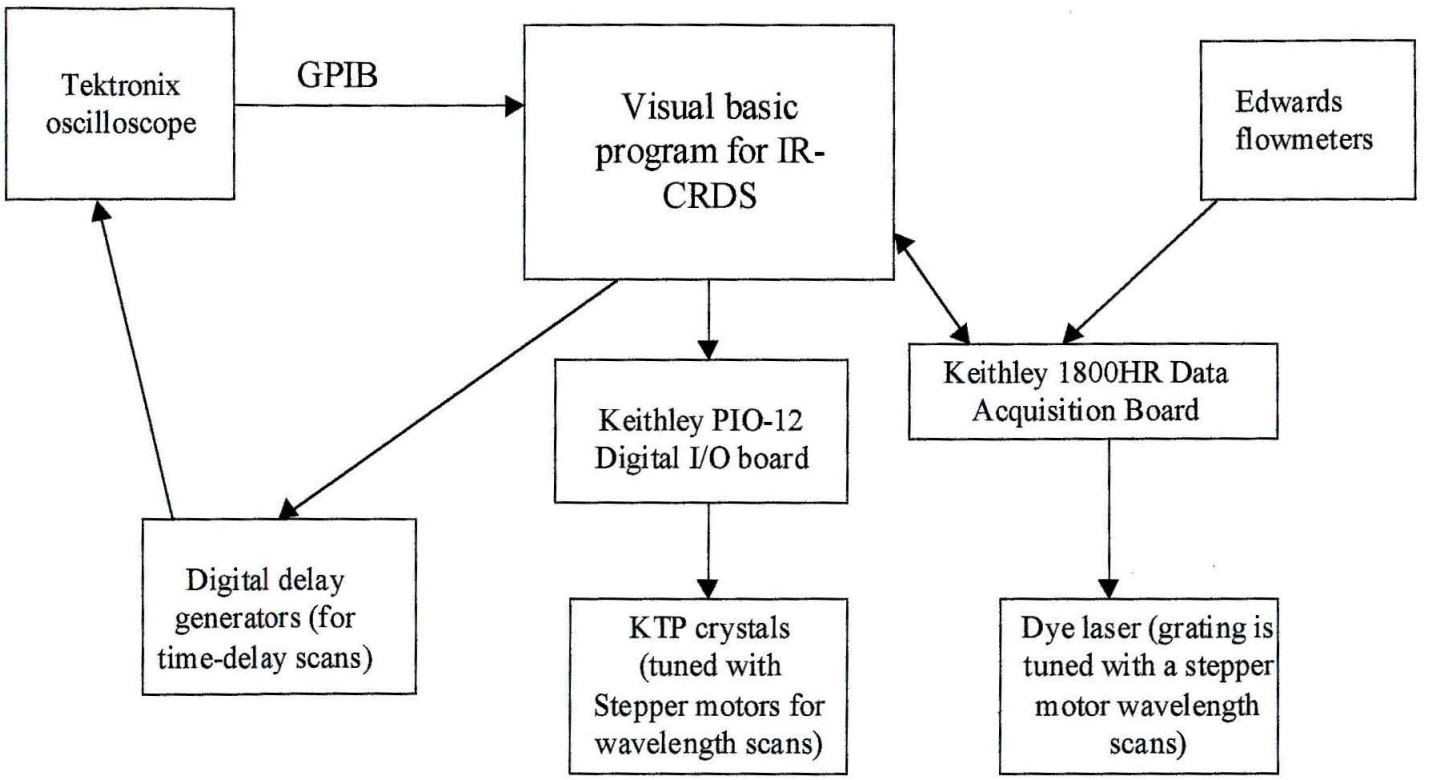

Figure 1.8. Schematic of the functions of Visual Basic program for use with IR-CRDS apparatus.

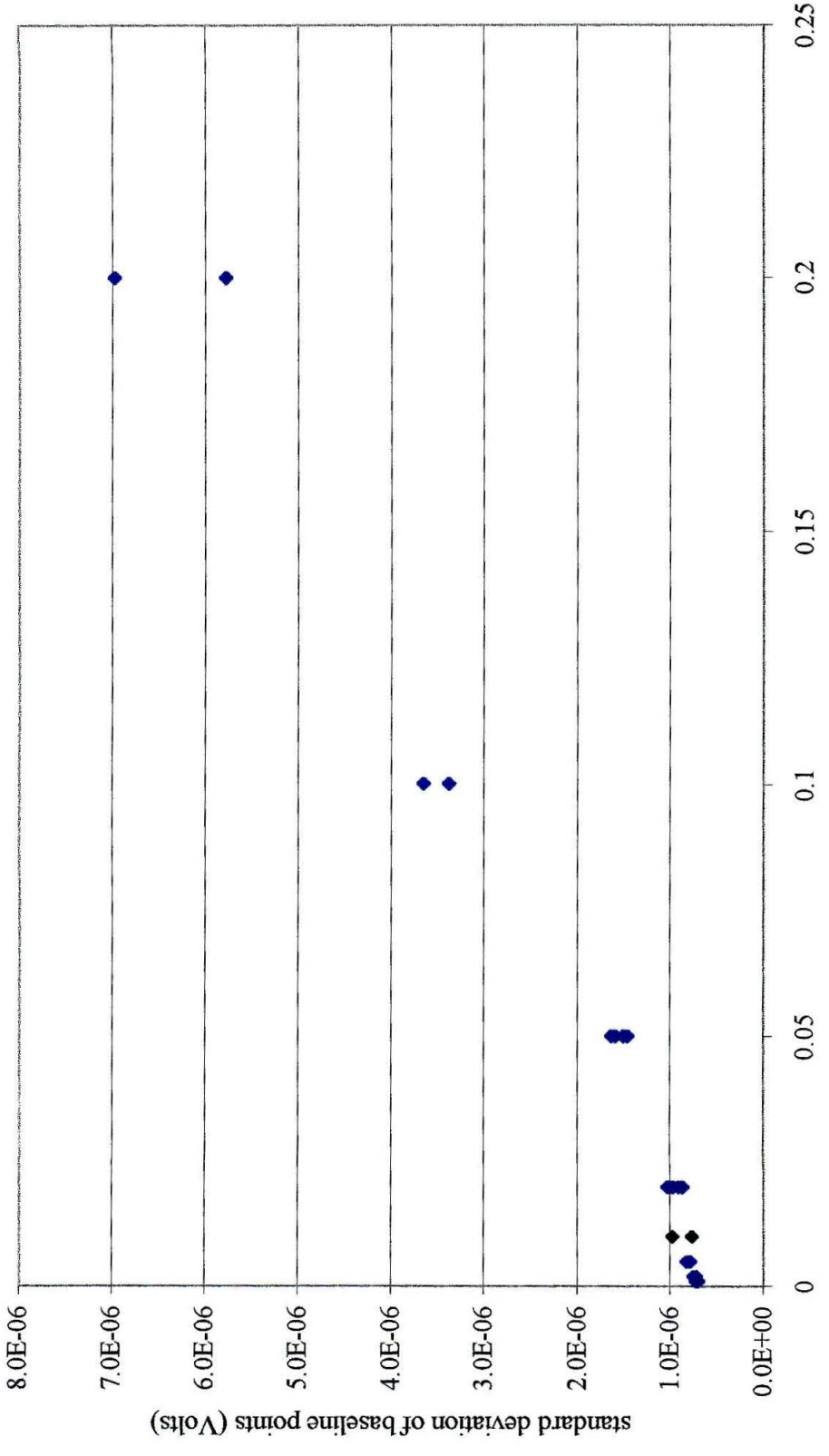

Figure 1.9. Noise in baseline points as a function of the scale of the oscilloscope.

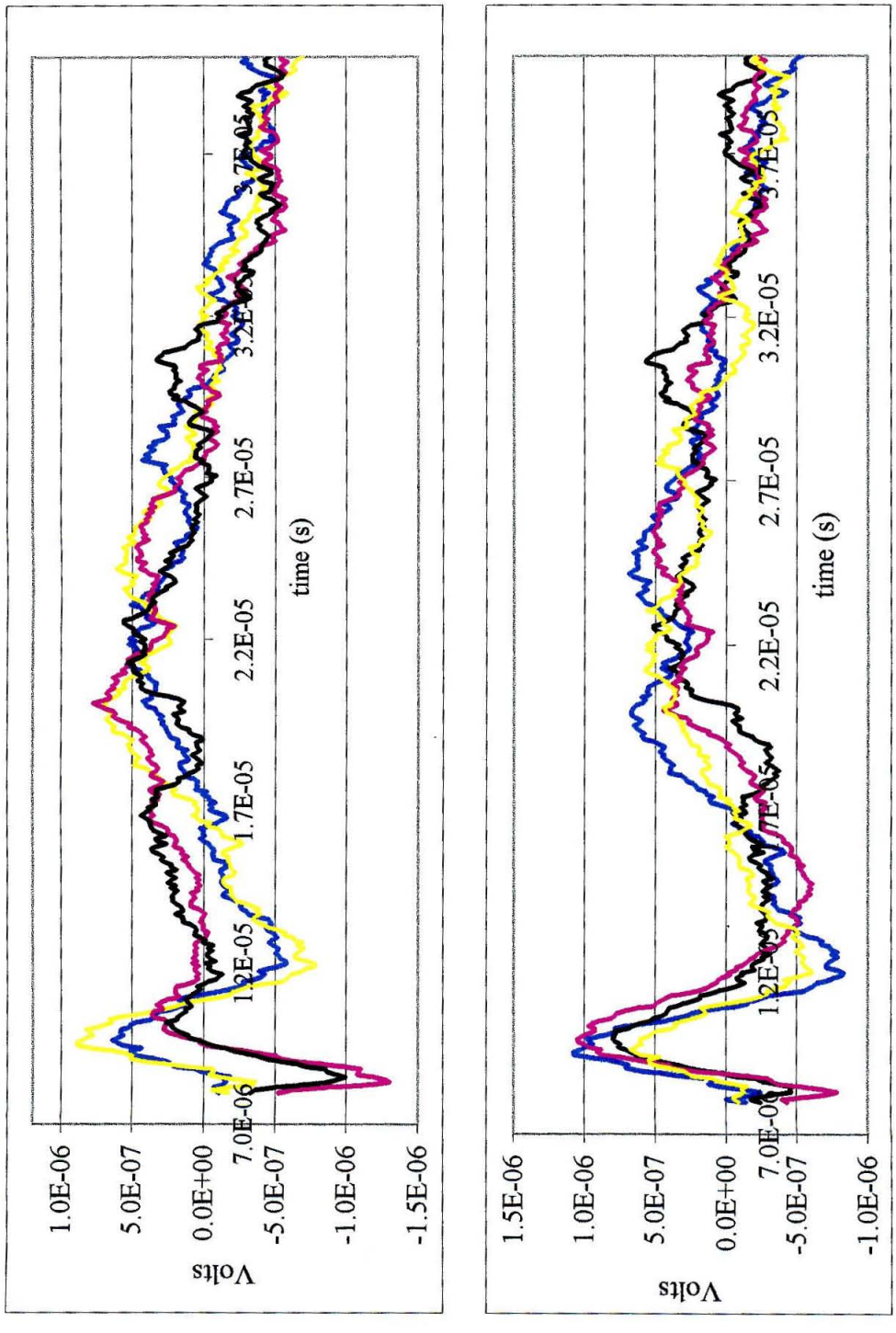

Figure 1.10. Sets of residual spectra from a single-exponential fit to ringdown curves (top graph) and a bi-exponential fit to ringdown curves (lower graph).

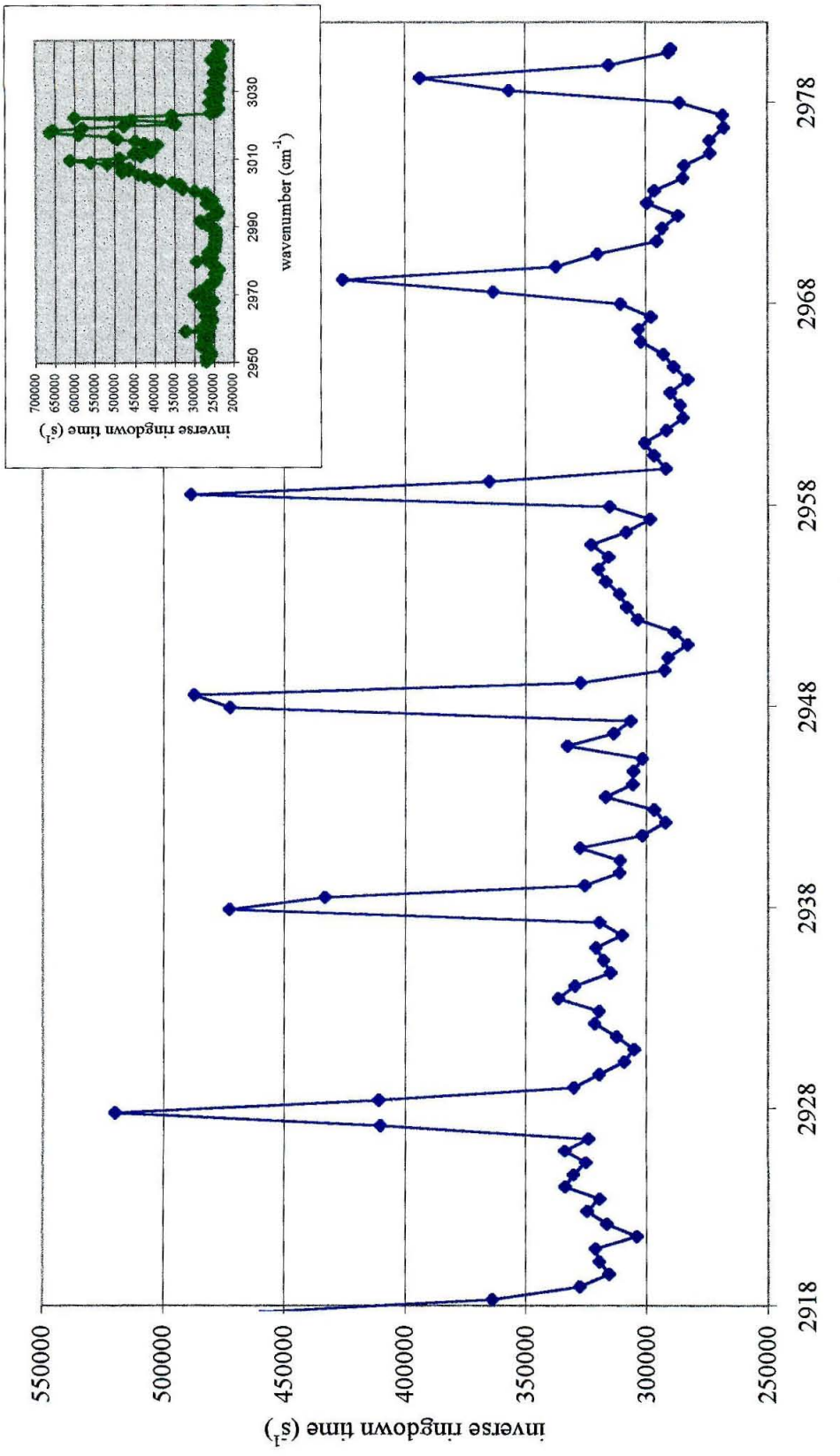

Figure 1.11. Cavity ringdown spectrum of 0.1 Torr methane. Inset depicts location and relative intensity of the Q branch.

CHAPTER 2

STUDIES OF THE REACTION OF HO_2 + ClO

2.1 INTRODUCTION

Reactive chlorine (ClO_x) and hydrogen oxide (HO_x) species play an integral role in reactions that affect ozone levels in the stratosphere. One of the major sources of stratospheric chlorine is anthropogenic emissions from compounds such as chlorofluorocarbons (CFCs). An understanding of the precise chemistry undergone by HO_x and ClO_x is necessary to determine mechanisms and possible remedies for ozone depletion in the stratosphere.

HO_x and ClO_x reaction cycles that lead to the destruction of ozone include:[1]

$$O + HO_2 \rightarrow OH + O_2 \quad (2.1)$$

$$OH + O_3 \rightarrow HO_2 + O_2 \quad (2.2)$$

$$O + ClO \rightarrow Cl + O_2 \quad (2.3)$$

$$Cl + O_3 \rightarrow ClO + O_2 \quad (2.4)$$

The reaction between HO_2 and ClO has been shown to produce predominantly HOCl and O_2 (Reaction 2.5). There also may be a minor channel of the HO_2 + ClO reaction that yields HCl and O_3 (Reaction 2.6).

$$HO_2 + ClO \rightarrow HOCl + O_2 \quad (2.5)$$

$$HO_2 + ClO \rightarrow HCl + O_3 \quad (2.6)$$

The HOCl + O_2 channel of the HO_2 + ClO reaction (Reaction 2.5) has no net effect on the levels of HO_x and ClO_x in the stratosphere since HOCl is readily photolyzed to OH and Cl which are involved in ozone destruction via reactions 2.2 and 2.4. However, the HCl + O_3 channel of the HO_2 + ClO reaction (Reaction 2.6) traps the chlorine in an unreactive form, namely HCl, and generates O_3. Because Reaction 2.6 eliminates radicals that may be involved in many cycles of ozone depletion, even a small

branching ratio for reaction 2.6 could have a large impact on O_3 levels in the stratosphere. In fact, Chance et al. suggest that a branching ratio of a few percent for reaction 2.6 could help resolve conflicts between measurements and models that overpredict the rate of ozone depletion and underpredict the ratio of HCl/ClO in the stratosphere.[2]

Many studies of the kinetics of the HO_2 + ClO reaction have taken place in the past 25 years. Table 2.1 summarizes the kinetic parameters obtained to date.[3,4,7,8,5,1,12,10] The JPL 97-4 Data Evaluation[6] recommendation for the temperature-dependent rate constant is $4.8*10^{-13}\ \exp(700\pm{}^{250}{}_{700})/T\ cm^3\ s^{-1}$, and the recommended value for the rate constant at 298 K is $5.0*10^{-12}\ cm^3\ s^{-1}$. A recent study by Knight et al.[12] using discharge flow / mass spectrometry at pressures of 1.1 to 1.7 Torr obtained a rate constant of $(7.1 \pm 0.4)*10^{-12}\ \exp\{(-16 \pm 17)/T\}\ cm^3\ s^{-1}$ corresponding to a 298 K rate constant of $(7.1 \pm 1.8)*10^{-12}\ cm^3\ s^{-1}$. Another recent study by Nickolaisen et al.[10] using flash photolysis / UV absorption at pressures of 50-700 Torr obtained a rate constant of $2.84*10^{-12}\ \exp\{[312 \pm 60)/T\}\ cm^3\ s^{-1}$, corresponding to a 298 K rate constant of $(8.1\pm1.6)*10^{-12}\ cm^3\ s^{-1}$. The room temperature rate constants obtained by Knight et al. and Nickolaisen et al. are within the error ranges of each other.

Several attempts to determine the branching ratio for Reaction 2.6 have demonstrated the difficulties involved in obtaining precise measurements of the HCl + O_3 channel from the reaction of HO_2 + ClO. Experiments reported in 1980 by Leck et al. attempted to detect O_3 by mass spectrometry at 298 K and pressures of 2-6 Torr; however, they did not observe any O_3 and put an upper limit of 2% on the branching ratio for reaction 2.6 based on the limits of their instrument sensitivity.[7] Shortly thereafter, Burrows and Cox used a chemiluminescent analyzer to monitor O_3 production from

Reaction 2.6 at 300 K and 1 atm.[8] They found that a significant amount of ozone was produced from the following series of reactions beginning with ClO disproportionation:

$$ClO + ClO \rightarrow Cl + OClO \quad (2.7)$$

$$OClO + h\nu \rightarrow O + ClO \quad (2.8)$$

$$O + O_2 + M \rightarrow O_3 + M \quad (2.9)$$

After accounting for this channel and for other side reactions leading to O_3 production, Burrows and Cox were able to place an upper limit on the $HCl + O_3$ channel from the reaction of $HO_2 + ClO$ of 0.3% at 300 K. In 1995, Finkbeiner et al. monitored ozone production with matrix isolation FTIR. Although they had difficulties overcoming side reactions that led to the production of ozone, primarily from the aforementioned reactions initialized by ClO disproportionation, they were able to report an upper limit of 1% for the $HCl + O_3$ channel at 300 K, and branching ratios of 2 ± 1 % at 240 K, and 5 ± 2% at 210 K.[1]

Theoretical studies have shown that the $HO_2 + ClO$ reaction can proceed on either a triplet or singlet surface.[9,10,11] On the triplet surface, hydrogen abstraction leads to the $HOCl + O_2$ products. The singlet surface involves a stable HOOOCl intermediate which can then decompose to generate $HCl + O_3$ or $HOCl + O_2(^1\Delta)$. The reaction of $HO_2 + ClO$ to produce HOOOCl is exothermic by 15.4 kcal/mol, suggesting that the lifetime of HOOOCl may be sufficiently long for the species to be experimentally observed. No successful identification of HOOOCl has occurred to date. Knight et al. attempted to detect HOOOCl and its possible fragments with mass spectrometry at temperatures of 215-298 K and pressures ranging from 1.1-1.7 Torr.[12] They did not observe any signal at m/e = 84 or 86 for the parent ions or at m/e = 83, 85, 68, or 49 for the fragments.

We utilized our infrared cavity ringdown apparatus, described in Chapter 1 of this thesis, to study the kinetics of the HO_2 + ClO reaction. Additionally, we searched for the formation of the HOOOCl intermediate. Recently, Francisco and Sander[11] calculated the harmonic frequencies for HOOOCl, and their calculated value for the ν_1 stretch is 3551 cm^{-1}. Our cavity ringdown apparatus is an ideal instrument to use in probing the absorption of HOOOCl at 3551 cm^{-1}. The apparatus is tunable over a broad range from 3300 - 3750 cm^{-1} with a single set of ringdown mirrors. The expected 20 cm^{-1} linewidth of the HOOOCl stretch at 3551 cm^{-1} is optimal for detection with our 1 cm^{-1} linewidth laser system.

Before performing experiments aimed at elucidating the kinetics and possible formation of HOOOCl from the HO_2 + ClO reaction, we studied the HO_2 self-reaction to demonstrate the capabilities of our apparatus for use in kinetic studies. Our studies of the HO_2 + HO_2 reaction are detailed in Section 2.2, and our studies of the HO_2 + ClO reaction are reported in Section 2.3.

2.2 THE REACTION OF HO_2 + HO_2

A. Experimental Relevance

As an initial kinetics experiment with our cavity ringdown apparatus, we synthesized HO_2 in our reaction cell and then followed the decay of the HO_2 infrared signal as a function of time. The HO_2 + HO_2 reaction has been extensively studied, and the products have been identified as H_2O_2 and O_2:[13,14,15,16]

$$HO_2 + HO_2 \rightarrow H_2O_2 + O_2 \quad (2.10)$$

The JPL 97-4 Data Evaluation[6] recommendation for the rate constant of the reaction is $2.3*10^{-13}$ exp{(600±200)/T} for the bimolecular reaction, and the recommended rate constant for the third-body mediated reaction is $1.7*10^{-33}$[M] exp{(1000±400)/T}.

Because reaction 2.10 is well-characterized and experimentally straightforward, we investigated the kinetics of this reaction in order to determine the capabilities of our cavity ringdown apparatus for kinetic studies. Furthermore, the HO_2 self-reaction is in competition to the HO_2 + ClO reaction that is the main interest of this chapter. Therefore, it was advantageous to study reaction 2.10 prior to examining the HO_2 + ClO reaction.

B. Experimental

HO_2 was formed in situ from the photolysis of ozone at 248 nm in the presence of H_2 and O_2. $O(^1D)$ was generated from the photolysis of ozone, and then the $O(^1D)$ reacted with H_2 to form OH and H. The H then reacted with O_2 to form HO_2, as shown in the following scheme:

$$O_3 + h\nu \rightarrow 0.9\ O(^1D) + 0.1\ O(^3P) + O_2 \quad (2.11)$$

$$O(^1D) + H_2 \rightarrow OH + H \quad (2.12)$$

$$H + O_2 \rightarrow HO_2 \quad (2.13)$$

Two methods were used to generate ozone. In the first setup, ozone was synthesized by flowing O_2 through a glass tube and dissociating it with a Tesla Coil. The ozone was then trapped in a glass u-tube filled with coarse silica gel and immersed in a dry ice / acetone slush. Ozone was removed from the silica gel by flowing O_2 through the tube. This method of preparation was difficult to employ for quantitative experiments because there was a decrease of ozone concentration in the O_2 flow as a function of time

as the amount of ozone trapped on the silica gel decreased. The second ozone synthesis method utilized a commercial ozonizer (Ozotech Model OZ2SS-SS). We calibrated the setting of the ozone generator with the concentration of ozone obtained with a flow of 500 sccm of oxygen through the generator, and the results are shown in Figure 2.1. Ozone concentrations were determined by measuring ozone's absorption of 254 nm radiation generated by a mercury lamp (UVP Model UVG-11) and detected with a silicon photodiode (ThorLabs). Beer's Law was employed to determine the ozone concentration based on its cross section of $1.15*10^{-17}$ cm^2 at 254 nm.[6] Ozone that was not photolyzed or consumed in the reactions was destroyed after exiting the reaction cell by passing it through a copper mesh heated to 200 °C.

Research grade hydrogen and oxygen gases were obtained from Air Liquide, and their flow rates were monitored with flow meters. Argon was used to purge the ringdown mirrors in the experiment. Hydrogen, oxygen, and argon were flowed from the cylinders to the cell in 1/4" copper tubing; ozone was flowed through 1/4" stainless steel tubing. The total pressure in the cell was controlled with a stopcock located at the gas exit of the cell.

C. Modeling of Reaction Conditions

Our reaction conditions were modeled with FACSIMILE software to determine optimal reaction conditions and to account for any side reactions. The initial concentrations of the reactants and rate constants for all reactions were entered into the FACSIMILE program. Then, the program generated an output file containing the concentrations of desired species as a function of time.

Table 2.2 displays the reactions and rate constants used in our FACSIMILE models of the $HO_2 + HO_2$ reaction. A typical output curve for the decay of HO_2 as a function of time is displayed in Figure 2.2. Based on our FACSIMILE modeling, we chose to use concentrations of $2.4*10^{18}$ molec/cc of O_2, $2*10^{14}$ molec/cc of O_3, $1*10^{19}$ molec/cc of H_2, and $4*10^{17}$ molec/cc of Ar for our studies of the $HO_2 + HO_2$ reaction. These initial concentrations were expected to yield an initial HO_2 concentration of 10^{14} molec/cc, assuming a 9% photolysis of ozone. A 9% ozone photolysis was used in the models based on the cross section for ozone of $1.08*10^{-17}$ cm^2 at 248 nm and the approximation that 125 mJ of 248 nm radiation would enter the reaction cell.

We chose to probe HO_2 absorption at 3417 cm^{-1} because there was minimal interference from other species, such as water and H_2O_2, at that wavelength. Based on our sensitivity experiments for methane reported in Chapter 1 of this thesis, we estimated the detectivity limit of HO_2 at 3417 cm^{-1} with our CRDS apparatus. First, we added the cross sections of the individual bands of CH_4 and HO_2 that are reported in HITRAN within a one cm^{-1} range, which is the approximate linewidth of our probe radiation. Then we compared the summation of the cross sections for CH_4 and HO_2. For the CH_4 j = -7 line at 2928 cm^{-1}, our experimentally determined detectivity limit is approximately 10^{12} molecules/cc, and the summation of the HITRAN cross sections within the one wavelength centered at 2927.5 cm^{-1} is $1.4*10^{-19}$ cm^2. The summation of the HO_2 cross sections from 3416.4 to 3417.4 cm^{-1} is $7*10^{-21}$ cm^2. Therefore, based on the relative cross sections, we would expect our detectivity for HO_2 would be 20 times lower than for CH_4. Due to the reflectivity of the ringdown mirrors, our background ringdown time for methane detection at 2938 cm^{-1} was approximately 3.3 μs, and our background ringdown

time for HO_2 detection at 3417 cm^{-1} was 10 μs, resulting in approximately three times greater sensitivity at the HO_2 detection wavelength. Combining the effects of relative cross sections and mirror reflectivities for CH_4 and HO_2 detection, we estimated our detection limit for HO_2 at $7*10^{12}$ molecules/cc. This detection limit was expected to facilitate detection of the anticipated 10^{14} molecules/cc of HO_2 from the aforementioned experimental conditions for studies of the self-reaction of HO_2.

D. Results

HO_2 Spectrum

Figure 2.3 depicts a difference spectrum of data taken with the excimer on (500 microsecond delay between the excimer firing and the IR probe beam entering the ringdown cavity) minus a spectrum taken with the excimer off. In addition to the experimental spectrum, spectra taken from the HITRAN database for HO_2 and H_2O are plotted. The experimental data has peaks in the 3375 - 3380 cm^{-1} range at the same locations as the reference HO_2 data; however, water absorption due to impurities in the precursor gases causes the spectrum to have a poor signal/noise ratio. Since background water absorption made the acquisition of a complete spectrum of HO_2 difficult to achieve with our ringdown apparatus, we shifted our focus to observing individual HO_2 peaks.

Figure 2.4 shows excimer on and excimer off spectra in the wavelength range of 3413 to 3425 cm^{-1}. The peak at 3421 cm^{-1} is due to water absorption, and is evident in both spectra. The peak at 3417 cm^{-1} is only present when the excimer laser is firing, and so this peak can be assigned to HO_2. Since there is no water absorption at 3417 cm^{-1}, and the HO_2 absorption at this wavelength is readily observable with our apparatus, we

decided to monitor this wavelength in order to probe the kinetics of the $HO_2 + HO_2$ reaction.

Kinetic Studies of $HO_2 + HO_2$

We monitored the decay of HO_2 as a function of time at 3417 cm^{-1}. The delay between the time the excimer laser was fired and the IR probe beam was sent into the ringdown cavity was varied in order to obtain the time dependence of the HO_2 concentration. At each time delay, 32 ringdown decays were averaged and the ringdown time was calculated. This procedure was repeated four times to obtain four datapoints of the ringdown time at each time delay.

Figure 2.5 displays the change in the inverse ringdown time at 3417 cm^{-1} as a function of time. The change in the inverse ringdown time is proportional to the concentration of HO_2, as is evidenced in the following equation, where τ_0 is the ringdown time before photolysis occurs, τ is the ringdown time at a specific time after photolysis, c is the speed of light, L is the length of the cavity, and A is the sample absorption (due to HO_2 absorption):

$$1/\tau - 1/\tau_0 = (cA)/L$$

Since $A = \varepsilon CL$, according to Beer's Law, where ε is the wavelength-dependent absorption cross section of the absorbing species, C is its concentration, and L is the path length, the change in the inverse ringdown time with and without the presence of HO_2 in the cell is directly proportional to the concentration of HO_2, and in many cases the concentration of a species can be determined in this manner. Unfortunately, since the linewidth of HO_2 is much narrower than the linewidth of our probe IR radiation, we could

not obtain an accurate value for the HO_2 absorption cross section, and so we could not directly elucidate the concentration of HO_2 from our ringdown data.

We used FACSIMILE modeling to determine the relationship between our ringdown data and the absolute value of the concentration of HO_2 as a function of time. In our experiment, the initial concentrations of all reaction precursors, the total pressure, and the rate of HO_2 decay were known. The percent of ozone photolysis was not known because the amount of UV radiation from the excimer laser that penetrated the quartz cell wall could not be determined. Therefore, we ran FACSIMILE models to obtain the best possible fit to our data, with the amount of ozone photolysis as a variable.

The best FACSIMILE fit to our data is shown in Figure 2.6. This fit utilized a 9% photolysis of ozone. At 248 nm, the cross section for ozone is $1.08 * 10^{-17}$ cm^2. Therefore, a 9% dissociation would correspond to a value of $8.3*10^{15}$ photons/cm^2 of 248 nm radiation, which in turn corresponds to 6.6 mJ/cm^2 of 248 nm energy. The excimer beam was expanded to approximately 19 cm x 1 cm, and so the total energy of the excimer beam in the reaction cell is 125 mJ, according to the model. The initial energy of the excimer beam (directly after exiting the excimer laser) is approximately 250 mJ, and so our results suggest that half of the energy of the beam is lost by the time it enters the cell. This amount of loss was considered reasonable if one accounts for the number of optics and the distance traveled by the excimer beam before it reaches the cell as well as reflection and absorption of the UV radiation by the quartz cell wall.

We were able to extract our observed absorption cross section for the HO_2 molecule at 3417 cm^{-1} based on the kinetic equation for a second order reaction, where A

is the concentration of the species at time t, $[A]_o$ is the initial concentration of the species, and k is the rate constant:

$$1/[A] - 1/[A]_o = 2kt$$

In our case, we plotted $1/\tau - 1/\tau_o$ versus time, from which the following equation can be obtained, where τ_o is the background ringdown time, τ is the ringdown time at time t, k is the rate constant, c is the speed of light, σ is the cross section for HO_2, L_{cell} is the length of the ringdown cell, and L_{phot} is the length of the photolysis region of the ringdown cell:

$$(1/\tau - 1/\tau_o)^{-1} = \{(2kL_{cell})/(c\sigma L_{phot})\}t + \{L_{cell}/c\sigma[A]_o L_{phot}\}$$

The plot of $(1/\tau - 1/\tau_o)^{-1}$ versus time, shown in Figure 2.7, was fit to a line with a least squares fit. The slope of this line is $\{2kL_{cell}\}/\{c\sigma L_{phot}\}$, and all of these parameters are known except for σ. Inserting the values for the known parameters ($k = 2.3*10^{-12}$ cm^3 s^{-1}, $L_{cell} = 84$ cm, $L_{phot} = 19$ cm, $c = 3*10^{10}$ cm s^{-1}, slope = 0.0103), we obtained a value of $6.6*10^{-20}$ cm^2 for σ. Based on the y-intercept, we obtained a value of $3*10^{-13}$ for $[A]_o$. The summation of cross sections from the HITRAN database over the range of 3416.4 to 3417.4 cm^{-1} is $7*10^{-21}$ cm^2. Since the exact wavelength profile of our laser is not known, and because our laser linewidth is much wider than the absorption linewidth for HO_2, we cannot compare our observed cross section directly to cross sections reported in HITRAN. It is reasonable that we observed a larger effective cross section than the summation of cross sections within the one wavelength range reported in HITRAN because we adjusted the wavelength of our laser to obtain a maximum HO_2 absorption, which likely resulted in a large overlap of the wavelength profile of our laser with strong HO_2 absorption bands. Although our sensitivity varied significantly from day to day, a

typical minimum detection (signal/noise = 1) for HO_2 under these conditions was $5*10^{12}$ molecules*cm^{-3}.

We found that our calculated value for the absorption cross section of HO_2 was very sensitive to the background subtraction of the ringdown time of the cell with no HO_2. A change of one standard deviation in the background ringdown time lead to a 10% change in the calculated value for the absorption cross section. The background ringdown time fluctuated over the course of the experiments due to fluctuations in the profile of the IR beam entering the cell and likely inhomogeneities in the ringdown mirrors' reflectivity.

Our analysis of the HO_2 self-reaction with our cavity ringdown apparatus demonstrated the capabilities of our setup for use in kinetics studies. We were able to determine the concentration of HO_2 as a function of time based on FACSIMILE modeling with a known rate constant for the HO_2 self-reaction. Our results also reinforced our earlier conclusion (see Chapter 1) that quantitative data on cross sections could only be obtained if the linewidth of the molecule being probed were larger than our laser linewidth. Finally, the importance of obtaining a precise value for the empty-cell ringdown time was shown to be crucial in order to extract kinetic information from our data. The conclusions reached based on our studies of the $HO_2 + HO_2$ reaction prepared us for our main goal of studying the reaction of $HO_2 + ClO$.

2.3 THE REACTION OF HO_2 + ClO

A. Experimental Conditions

The experimental setup for our studies of the reaction of HO_2 and ClO was an extension of our previously described setup for the HO_2 self-reaction. HO_2 was formed in the same manner as before, and ClO was formed from the photolysis of Cl_2O at 248 nm. Cl_2O was synthesized by flowing Cl_2 over HgO, followed by trapping the Cl_2O in a tube immersed in an ethanol/liquid nitrogen slush.[17] The Cl_2O was purified by placing the resulting crude product under reduced pressure for several hours to remove excess Cl_2. Then, the Cl_2O was introduced into the reaction cell by bubbling helium through liquid Cl_2O immersed in a dry ice/acetone bath. The concentration of Cl_2O was determined by measuring its absorption of 254 nm radiation from a mercury lamp based on the cross section of $1.9*10^{-18}$ cm^2 for Cl_2O absorption at 254 nm.[6] After the Cl_2O entered the reaction cell, ClO was generated by photolyzing the Cl_2O at 248 nm; the cross section for Cl_2O photolysis at 248 nm is $1.9*10^{-18}$ cm^2.[6]

To search for the formation of HOOOCl at low temperatures, we employed the cooled kinetics cell discussed and depicted in Chapter 1 of this thesis. This cell consisted of three jackets: the inner jacket contained the contents of the cell, the middle jacket contained the methanol coolant, and the outer jacket held a vacuum to prevent frosting of the cooled jacket. The photolysis beam was sent through all three jackets, and each quartz layer was specified to transmit 91% of the incident UV radiation. The methanol and impurities in the methanol may have increased losses due to scattering and

absorption, and we estimated a total loss of 50% of our excimer beam in travelling from the outer jacket to the center of the cell.

B. Modeling of Reaction Conditions

As with the HO_2 self-reaction, we used FACSIMILE models to determine appropriate reaction conditions for our studies of HO_2 + ClO. The rate equations used in this model were obtained from the JPL 97-4 Data Evaluation[6] and are shown in Table 2.3. Our initial goal was to observe an increase in the decay rate of $[HO_2]$ due to the presence of ClO since the reaction of HO_2 + ClO will cause $[HO_2]$ to decrease more rapidly than in the absence of ClO. A second objective was to observe the grow-in of HOCl as a product of the reaction of HO_2 + ClO $\rightarrow$ HOCl + O_2. Therefore, we generated an output file from FACSIMILE displaying the concentrations of HO_2, ClO, and HOCl as a function of time. In addition, we modeled the concentrations of H_2O because of its potential spectroscopic interference with the other molecules. The results of this model, shown in Figure 2.8, indicate that HOCl should grow in slowly in the first 5 ms following the firing of the excimer laser. The concentration of HO_2 should peak immediately and decrease to half its initial value approximately 1.5 ms after the firing of the excimer laser.

After examining the kinetics of the HO_2 + ClO reaction, our aim was to search for the possible formation of HOOOCl. Based on data presented in the introduction of this chapter, it is expected that lower temperatures would favor the formation of HOOOCl. Therefore, we performed experiments in a cooled infrared kinetics cell that probed for HOOOCl formation at temperatures of -60 °C. A FACSIMILE model of the expected HOOOCl formation at -60 °C is presented in Figure 2.9. This model includes rate

constants for all reactions listed in Table 2.3, and all temperature-dependent rates in the model are adjusted to their values at -60 °C.

C. Results

HO_2 Decay

As predicted in our FACSIMILE models, we found that the rate of HO_2 decay increased as Cl_2O was added to the reaction mixture. Figure 2.10 shows our data for the concentration of HO_2 as a function of time with and without Cl_2O. FACSIMILE fits to the data are also included in Figure 2.10. For this experiment, concentrations of $1.1*10^{19}$ molec/cc of H_2, $7.0*10^{14}$ molec/cc of O_3, $2.6*10^{18}$ molec/cc of O_2, $1.5*10^{18}$ molec/cc of He, and $4.5*10^{17}$ molec/cc of Ar (for purging the ringdown mirrors) were used. The total cell pressure was 400 Torr. Cl_2O was added to the mixture by bubbling 800 Torr of He through Cl_2O, and the concentration of Cl_2O in the cell was determined to be $4.5*10^{15}$ molec/cc based on its absorption at 253 nm prior to entering the reaction cell.

The FACSIMILE models shown in Figure 2.10 were constructed via several steps. First, the percent of O_3 photolysis in the model was adjusted to obtain a good fit for the experimentally observed decay of HO_2 from the $HO_2 + HO_2$ reaction with no Cl_2O in the cell. Then, the percent of Cl_2O photolysis was calculated based on the relative cross sections of O_3 and Cl_2O at 248 nm. Finally, the FACSIMILE model was run incorporating Cl_2O, ClO, and the reactions listed in Table 2.3 in order to model the experimental data obtained with Cl_2O in the reaction cell. The best fit to the $HO_2 + HO_2$ data utilized an ozone photolysis yield of 5%. The ratio of the absorption cross section of

ozone to that of Cl_2O at 248 nm is 6:1, and so we calculated that 0.8% of the Cl_2O would dissociate under our conditions.

Three FACSIMILE models for the time-dependent decay of HO_2 are shown in Figure 2.10 using rate constants for the reaction of HO_2 + ClO of $5*10^{-12}$ cm^3 s^{-1} (JPL 97 recommendation),[6] $7*10^{-12}$ cm^3 s^{-1} (Knight et al.),[12] and $8*10^{-12}$ cm^3 s^{-1} (Nickolaisen et al.).[10] We found that all of these rate constants for the reaction of HO_2 + ClO gave reasonable fits to our data, and the scatter in our data points precludes a precise determination of the rate constant. Since our main goal was the search for the possible formation of HOOOCl, we did not pursue generating more data in order to obtain a more precise value of the rate constant for the reaction of HO_2 + ClO.

HOCl Formation

The formation of HOCl from the reaction of HO_2 + ClO was monitored at 3507 cm^{-1}. Figure 2.11 shows the grow-in of HOCl compared to the decay of HO_2 and the FACSIMILE fits to the data. As expected, the increase in HOCl mirrors the decrease in HO_2. The initial concentrations of gases used in this experiment were $9.2*10^{18}$ molec/cc of H_2, $1.6*10^{18}$ molec/cc of O_2, $1.2*10^{18}$ molec/cc of He, $1.5*10^{15}$ molec/cc of O_3, and $3.5*10^{15}$ molec/cc of Cl_2O. Again, there is a close corroboration between our data and the FACSIMILE fits. Since we do not know the exact cross section of either Cl_2O or HO_2 (because the transition linewidths are narrower than our laser linewidth, as discussed in Chapter 1), we could not estimate the percent of HO_2 that was being converted into HOCl. Thus, we could not calculate the branching ratio for Reaction 2.5 based on the experimentally observed formation of HOCl.

Detection of HOOOCl

Our initial experiments to detect HOOOCl formation were performed at room temperature. Spectra were taken from 3515 to 3567 cm^{-1} (Figure 2.12) since HOOOCl is predicted to absorb at 3551 cm^{-1}.[10] The data were taken 800 μs after the firing of the excimer laser because this is the time at which approximately half of the HO_2 had reacted, and so we would expect a significant amount of HOOOCl formation to have occurred by this time. To check for the possibility of HOOOCl formation in the spectrum, we first subtracted the spectrum with the excimer off from the spectrum with the excimer on. Then, reference curves for HO_2, HOCl, and H_2O were weighted and fit to the resulting data. Lastly, the weighted reference curve was subtracted from the (excimer on - excimer off) data. The residual spectrum, shown in Figure 2.13, did not contain any noticeable peaks that could be attributable to HOOOCl.

Low temperature spectra were taken at -60 °C, and they were manipulated as described in the room temperature experiments. The residual spectrum, shown in Figure 2.14, is expected to contain spectra of molecules other than HO_2, HOCl, and H_2O formed after the photolysis of O_3 and Cl_2O. The residual spectrum in Figure 2.14 shows a broad peak around 3550 cm^{-1}, and so we investigated the possibility that this peak could be due to HOOOCl. Since HOOOCl is not a stable molecule, it is not expected to be long-lived. However, time profiles of the peak at 3550 cm^{-1} indicate that the peak grows in and remains present over the length of the gases' residence time in the cell (Figure 2.15). Therefore, the observed peak was unlikely to be absorption due to HOOOCl. Further analysis showed that the peak was present even when there was no Cl_2O in the cell.

Subsequently, it was determined that the peak was attributable to H_2O_2, and Figure 2.16 shows an acquired spectrum of H_2O_2 overlaid on the HO_2 + ClO residual spectrum. The comparison in Figure 2.16 indicates that the H_2O_2 spectrum very closely matches the spectrum we obtained.

The observed H_2O_2 peak led us to revisit our FACSIMILE models to determine the relative amounts of H_2O_2 and HOOOCl expected to form in the reaction of HO_2 and ClO at -60 °C. The results of the model, shown in Figure 2.17, indicate that six times more H_2O_2 than HOOOCl is formed in the first millisecond after the photolysis of the reaction precursors. The source of this H_2O_2 is the self-reaction of HO_2, which generates the products H_2O_2 and O_2. We concluded that because of the large amount of H_2O_2 formed in this reaction and the overlap between the H_2O_2 spectrum and the predicted location of the HOOOCl band at 3551 cm^{-1}, it would be particularly difficult to detect HOOOCl in this wavelength region.

2.4 CONCLUSIONS

Initial kinetics experiments with our infrared cavity ringdown apparatus monitored the kinetics of the reaction of HO_2 + HO_2 at 298 K. FACSIMILE models were used to simulate our reaction conditions and generate expected concentrations of HO_2 as a function of time. Our data is fit well with a model incorporating the JPL-97 recommended rate constant of $1.7*10^{-12}$ cm^3 s^{-1}.[6] The results of our studies of the HO_2 + HO_2 reaction demonstrated the capabilities of our system for use in kinetic studies.

The kinetics of the reaction of HO_2 + ClO were probed at 298 K. Good fits to our data were generated with FACSIMILE models using rate constants for the HO_2 + ClO reaction ranging from $5*10^{-12}$ cm^2 s^{-1} (JPL-97 recommendation)[6] to $8*10^{-12}$ cm^2 s^{-1} (Knight et al.).[12] The formation of HOOOCl was not observed at 298 K. At 208 K, the possible formation of HOOOCl at 3551 cm^{-1} could not be detected at due to spectral interference by H_2O_2. Future experiments aimed at HOOOCl detection may be facilitated by probing different transitions of the HOOOCl molecule that are not subject to interference by other molecules.

2.5 REFERENCES

[1] M. Finkbeiner, J. N. Crowley, O. Horie, R. Muller, G. K. Moortgat, and P. J. Krutzen, *Journal of Physical Chemistry*, 99, 16264 (1995).

[2] K. Chance, W. A. Traub, D. G. Johnson, K. W. Jucks, P. Ciarpallini, R. A. Stachnik, R. J. Salawitch, and H. A. Michelsen, *Journal Geophysical Research - Atmospheres*, 101 (D4), 9031 (1996).

[3] B. Riemann and F. Kaufman, *Journal of Chemical Physics*, 69, 2925 (1978).

[4] R. Stimpfle, R. Perry, and C. J. Howard, *Journal of Chemical Physics*, 71, 5183 (1979).

[5] F. C. Cattell and R. A. Cox, *Journal of the Chemical Society Faraday Transactions*, 2 (82), 1413 (1986).

[6] W. B. DeMore, S. P. Sander, D. M. Golden, R. F. Hampson, M. J. Kurylo, C. J. Howard, A. R. Ravishankara, C. E. Kolb, and M. J. Molina, *Chemical Kinetics and Photochemical Data for Use in Stratospheric Modeling*, No. 11, Jet Propulsion Laboratory, Pasadena, CA (1997).

[7] T. J. Leck, J. E. Cook, and J. W. Brooks, *Journal of Chemical Physics*, 72 (4), 2364 (1980).

[8] J. P. Burrows and R. A. Cox, *Journal of the Chemical Society Faraday Transactions*, 77, 2465 (1981).

[9] D. Buttar and D. M. Hirst, *Journal of the Chemical Society Faraday Transactions*, 90 (13), 1811 (1994).

[10] S. J. Nickolaisen, C. M. Roehl, L, K. Blakeley, R. R. Friedl, J. S. Francisco, R. Liu, and S. P. Sander, *Journal of Physical Chemistry A*, 104, 308 (2000).

[11] J. S. Francisco and S. P. Sander, *Journal of Physical Chemistry*, 100, 573 (1996).

[12] G. P. Knight, T. Beiderhase, F. Helleis, G. K. Moortgat, and J. N. Crowley, *Journal of Physical Chemistry A*, 104, 1674 (2000).

[13] M. J. Kurylo, P. A. Ouellette, and A. H. Laufer, *Journal of Physical Chemistry*, 90, 437 (1986).

[14] C. C. Kircher and S. P. Sander, *Journal of Physical Chemistry*, 88, 2082 (1984).

[15] G. A. Takacs and C. J. Howard, *Journal of Physical Chemistry*, 88, 2110 (1984).

[16] G. A. Takacs and C. J. Howard, *Journal of Physical Chemistry*, 90, 687 (1986).

[17] M. Schmeisser, *Inorganic Synthesis*, 9, 127 (1967).

Authors	Rate constant (cm^3s^{-1})	Branching Ratio for $HCl + O_3$ product	Ref-erence
Riemann and Kaufman	$(3.8 \pm .5)*10^{-12}$ [298 K]		3
Stimpfle et al.	$(6.3 \pm 1.3)*10^{-12}$ [298 K] $3.3*10^{-11}exp(-850/T) + 4.5*10^{-12}(T/300)^{-3.7}$		4
Leck et al.	$(4.5 \pm 0.9)*10^{-12}$ [298 K]	<2% [298 K]	7
Burrows and Cox	$5.4*10^{-12}$ [300 K]	<0.3% [300 K]	8
Catrell and Cox	$(6.2 \pm 1.5)*10^{-12}$ [298 K]		5
Finkbeiner et al.		<1% [300 K], (2 ± 1)% [240 K], (5 ± 2)% [210 K]	1
Knight et al.	$(7.1 \pm 1.8)*10^{-12}$ [298 K] $(7.1 \pm 0.4)*10^{-12} exp\{(-16 \pm 17)/T\}$	< 1%	12
Nickolaisen et al.	$8.1*10^{-12}$ [298 K] $2.84*10^{-12} exp\{(312 \pm 60)/T\}$		10

Table 2.1. Measured rate constants and branching ratios for the reaction of $HO_2 + ClO$.

REACTION	RATE CONSTANT (cm^3 $molec^{-1}$ s^{-1})
$O(^1D) + H_2 = OH + H$	$1.1*10^{-10}$
$H + O_2 + M = HO_2 + M$	$5.7*10^{-32}*(T/300)$
$H + O_3 = OH + O_2$	$1.4*10^{-10}*EXP(-470.0/T)$
$O(^1D) + N_2 = O + N_2$	$4.0*10^{-11}$
$O(^1D) + O_2 = O + O_2$	$4.0*10^{-11}$
$OH + H_2 = H_2O + H$	$5.5*10^{-12}*EXP(-2000.0/T)$
$OH + O_3 = HO_2$	$1.5*10^{-12}*EXP(-880.0/T)$
$HO_2 + O_3 = OH + O_2 + O_2$	$2.0*10^{-14}*EXP(-680.0/T)$
$HO_2 + HO_2 = H_2O_2 + O_2$	$2.3*10^{-12}$
$HO_2 + HO_2 + M = H_2O_2 + O_2 + M$	$1.7*10^{-33}*EXP(1000/T)$
$OH + HO_2 = H_2O + O_2$	$4.8*10^{-11}*EXP(250.0/T)$
$OH + OH + M = H_2O_2$	$7.0*10^{-31}$
$OH + OH = H_2O + O$	$4.2*10^{-12}*EXP(-240.0/T)$
$O + O_3 = O_2 + O_2$	$8.0*10^{-12}*EXP(-2060.0/T)$
$O(^1D) + O_3 = O_2 + O_2$	$1.2*10^{-10}$
$O + O_2 + M = O_3 + M$	$6.0*10^{-34}$
$O + OH = H + O_2$	$2.2*10^{-11}*EXP(120.0/T)$
$O + HO_2 = OH + O_2$	$3.0*10^{-11}*EXP(200.0/T)$

Table 2.2. Reactions and rate constants used in FASCIMILE modeling of the reaction of $HO_2 + HO_2$.

REACTION	RATE CONSTANT
$O(^1D) + H_2 = OH + H$	$1.1*10^{-10}$
$H + O_2 + M = HO_2 + M$	$5.7*10^{-32}*(T/300)$
$H + O_3 = OH + O_2$	$1.4*10^{-10}*EXP(-470.0/T)$
$H + Cl_2O = HCl + ClO$	$4.1*10^{-11}$
$O(^1D) + N_2 = O + N_2$	$4.0*10^{-11}$
$O(^1D) + O_2 = O + O_2$	$4.0*10^{-11}$
$OH + H_2 = H_2O + H$	$5.5*10^{-12}*EXP(-2000.0/T)$
$OH + O_3 = HO_2 + O_2$	$1.5*10^{-12}*EXP(-880.0/T)$
$OH + Cl_2O = HOCl + ClO$	$7*10^{-12}$
$HO_2 + O_3 = OH + O_2$	$2.0*10^{-14}*EXP(-680.0/T)$
$HO_2 + HO_2 = H_2O_2 + O_2$	$2.3*10^{-12}$
$HO_2 + HO_2 + M = H_2O_2 + O_2 + M$	$1.7*10^{-33}*EXP(1000/T)$
$OH + HO_2 = H_2O + O_2$	$4.8*10^{-11}*EXP(250.0/T)$
$OH + OH + M = H_2O_2$	$7.0*10^{-31}$
$OH + HCl = H_2O + Cl$	$2.6*10^{-12}*EXP(-350/T)$
$OH + HOCl = H_2O + ClO$	$3*10^{-12}*EXP(-500/T)$
$OH + Cl_2 = HOCl + Cl$	$1.4*10^{-12}*EXP(-900/T)$
$OH + ClO = HO_2 + Cl$	$0.9*1.1*10^{-11}*EXP(120/T)$
$OH + ClO = HCl + O_2$	$0.1*1.1*10^{-11}*EXP(120/T)$
$OH + OH = H_2O + O$	$4.2*10^{-12}*EXP(-240.0/T)$
$O + O_3 = O_2 + O_2$	$8.0*10^{-12}*EXP(-2060.0/T)$
$O(^1D) + O_3 = O_2 + O_2$	$1.2*10^{-10}$
$O + O_2 + M = O_3 + M$	$6.0*10^{-34}$
$O + OH = H + O_2$	$2.2*10^{-11}*EXP(120.0/T)$
$O + HO_2 = OH + O_2$	$3.0*10^{-11}*EXP(200.0/T)$
$O + ClO = Cl + O_2$	$3.0*10^{-11}*EXP(70.0/T)$
$O + Cl_2O = ClO + ClO$	$2.7*10^{-11}*EXP(-530/T)$
$Cl + Cl_2O = ClO + Cl_2$	$6.2*10^{-11}*EXP(130/T)$
$Cl + O_3 = ClO + O_2$	$2.9*10^{-11}*EXP(-260/T)$
$Cl + H_2 = HCl + H$	$3.7*10^{-11}*EXP(-2300/T)$
$Cl + H_2O_2 = HCl + HO_2$	$1.1*10^{-11}*EXP(-980/T)$
$Cl + O_2 + M = ClOO + M$	$2.7*10^{-33}*(T/300)@-1.5$
$ClO + HO_2 = HOCl + O_2$	$4.8*10^{-13}EXP(700/T)$
$ClO + HO_2 + M = HOOOCl + M$	$70*10^{-33}$
$Cl + HO_2 = HCl + O_2$	$1.8*10^{-11}*EXP(170/T)$
$Cl + HO_2 = ClO + OH$	$4.1*10^{-11}*EXP(-450/T)$
$ClO + ClO = ClOOCl$	$1.7*10^{-13}$
$ClO + ClO = Cl_2 + O_2$	$1.0*10^{-12}*EXP(-1590/T)$
$ClO + ClO = Cl + Cl + O_2$	$3*10^{-11}*EXP(-2450/T)$
$ClO + ClO = OClO + Cl$	$3.5*10^{-13}*EXP(-1370/T)$
$Cl + OClO = ClO + ClO$	$3.4*10^{-12}*EXP(160/T)$

Table 2.3. Equations and rate constants used for FACSIMILE modeling of the reaction of $HO_2 + ClO$.

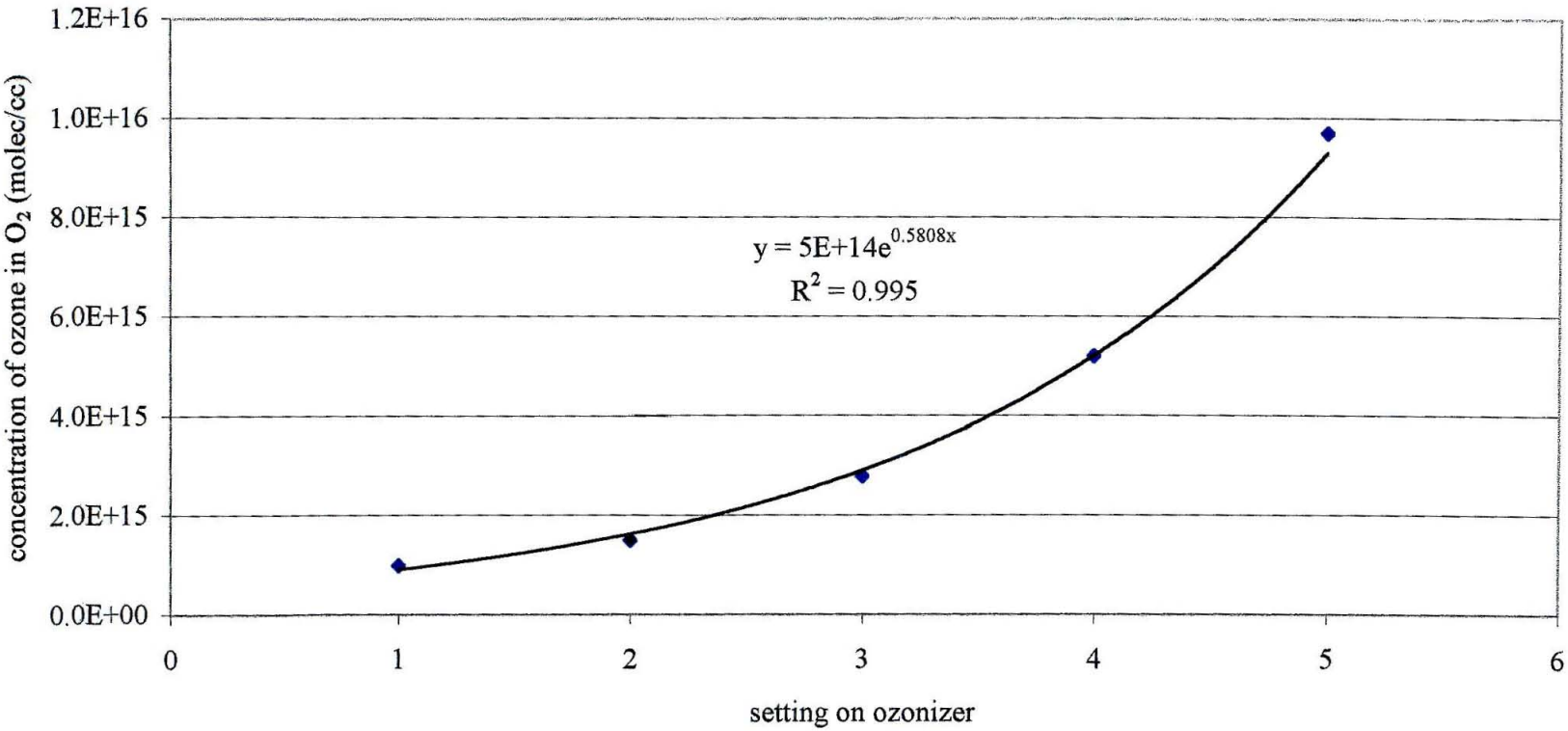

Figure 2.1. Calibration of ozotech ozonizer with 500 sccm flow of O_2.

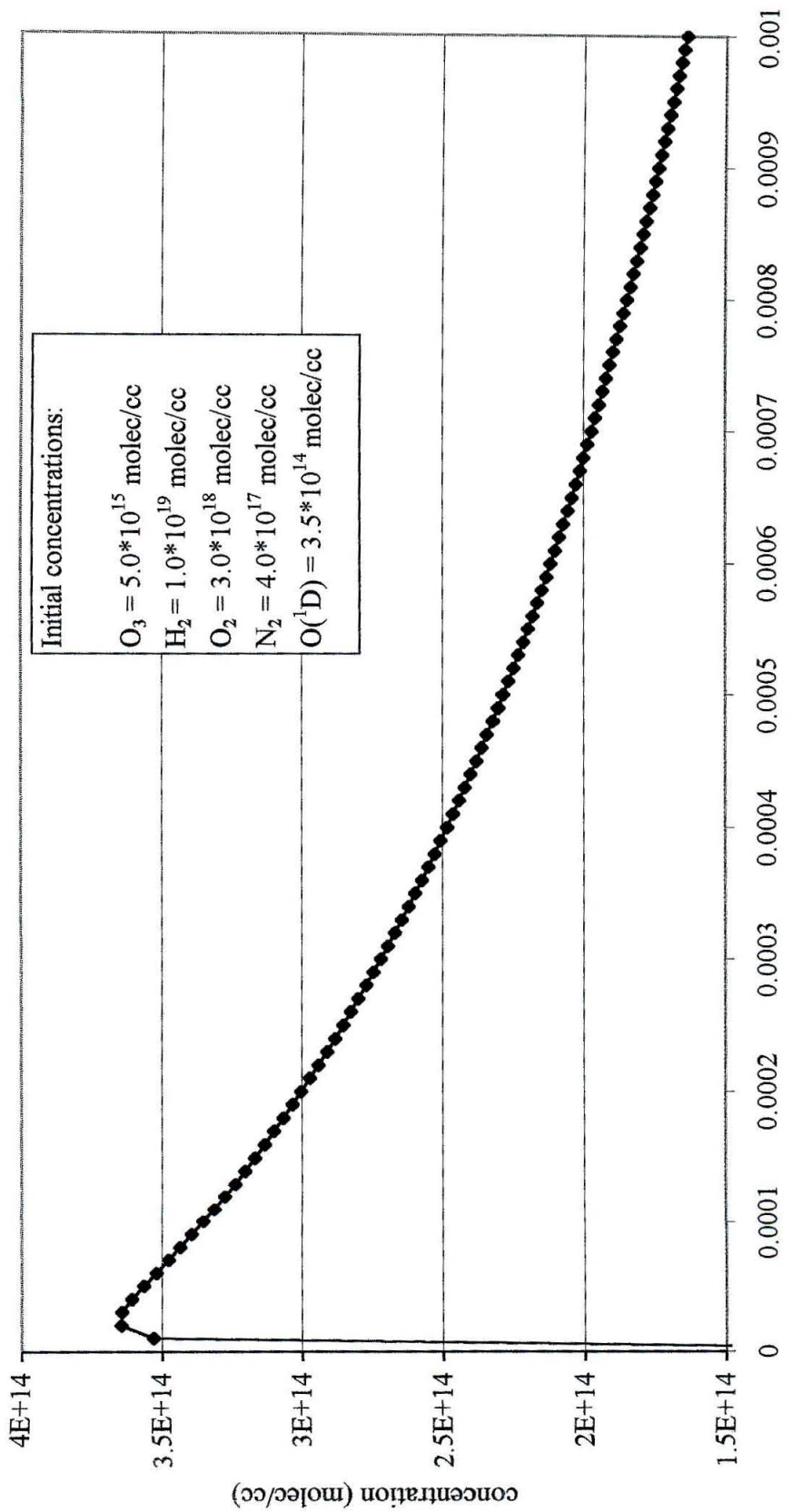

Figure 2.2. Typical FACSIMILE output of HO_2 decay as a function of time.

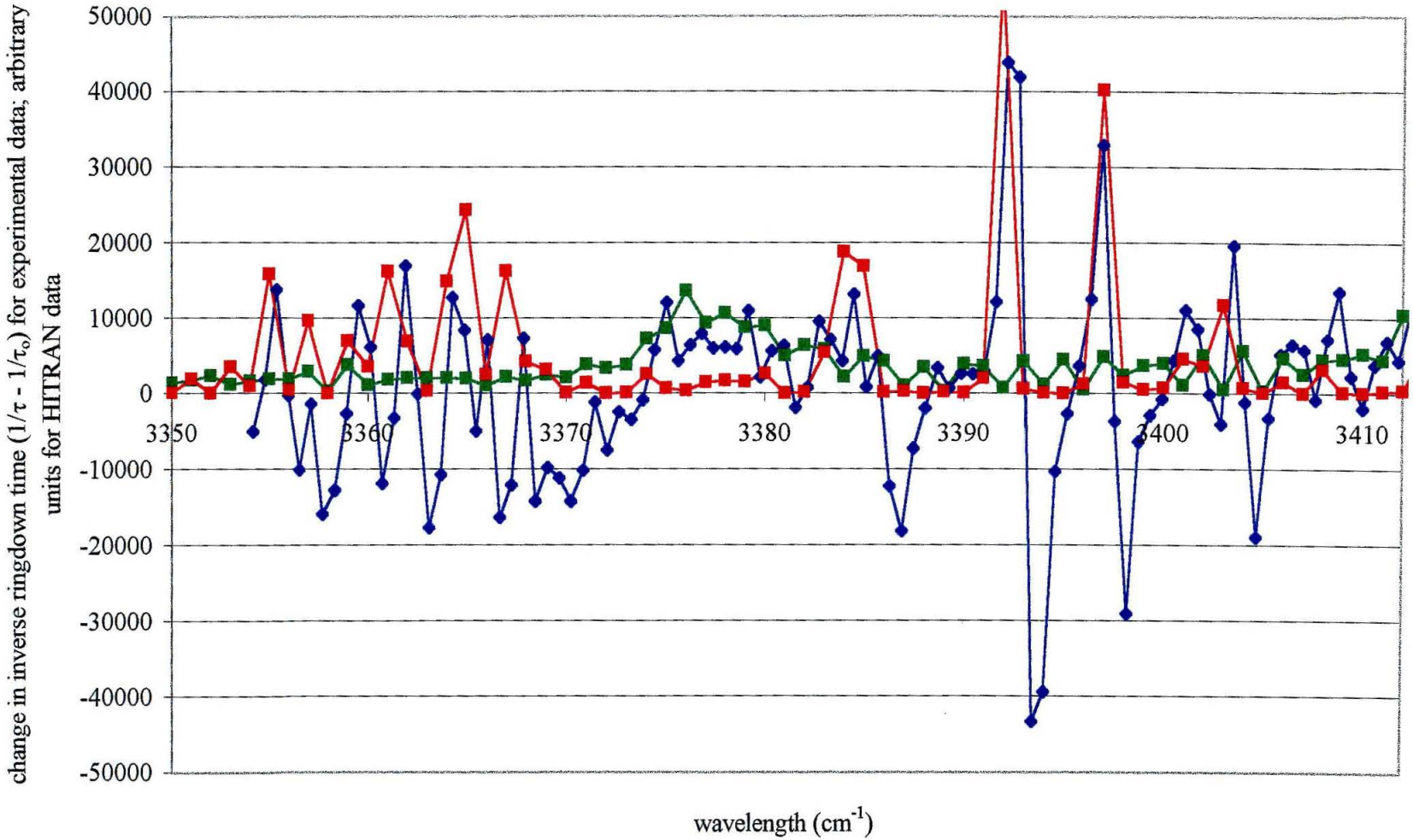

Figure 2.3. Blue data is residual (excimer on - excimer off) inverse ringdown times from the photoylsis of O_3 in the presence of H_2 and O_2. Red data is an H_2O reference spectrum and green data is an HO_2 reference spectrum (from HITRAN).

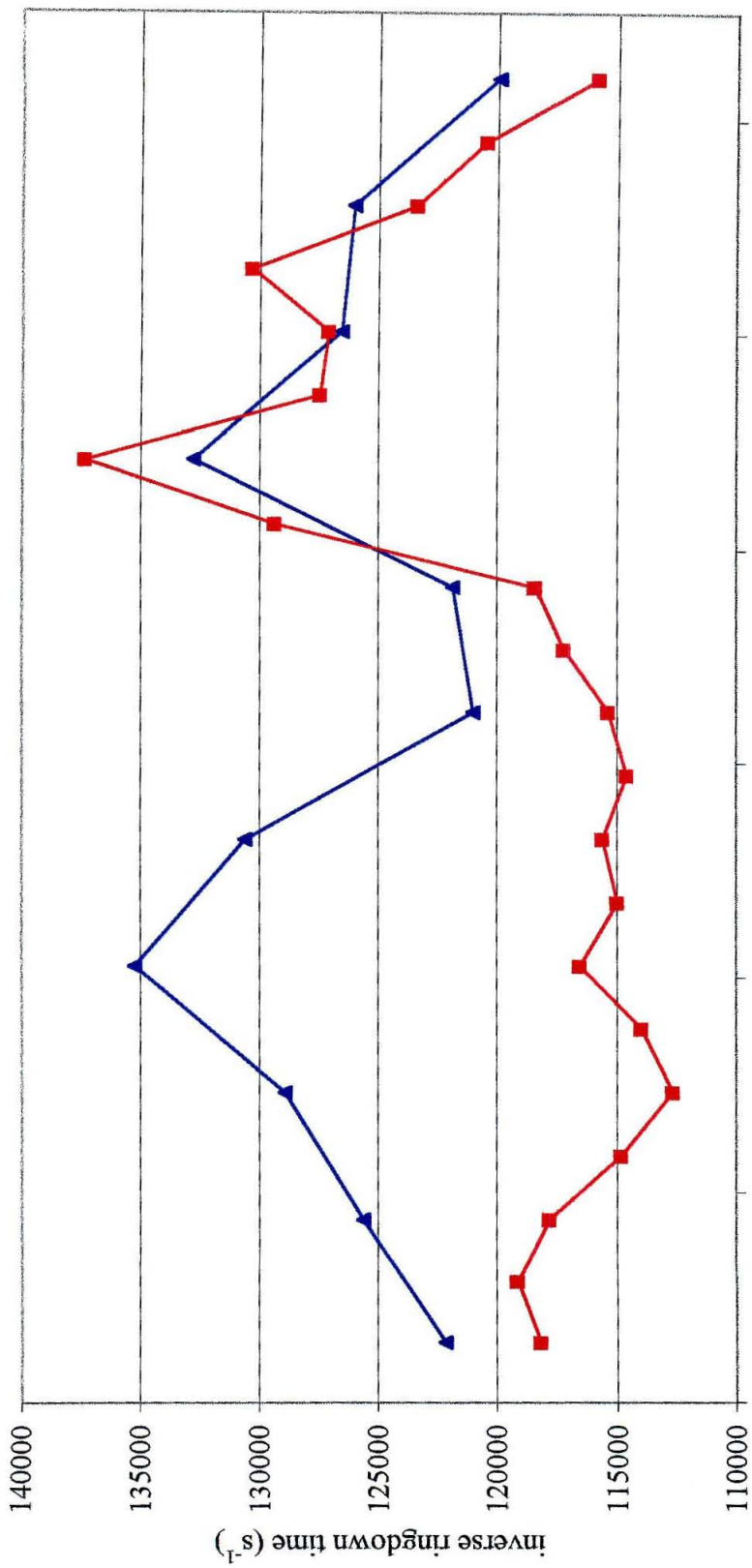

Figure 2.4. Scans of a mixture of O_3, H_2, and O_2 with IR-CRDS. Blue data (triangles) is with the excimer on and red scan (squares) is with the excimer off. The peak at 3423 cm^{-1} is due to H_2O absorption, and the peak at 3417 cm^{-1} in the blue scan is due to HO_2 absorption.

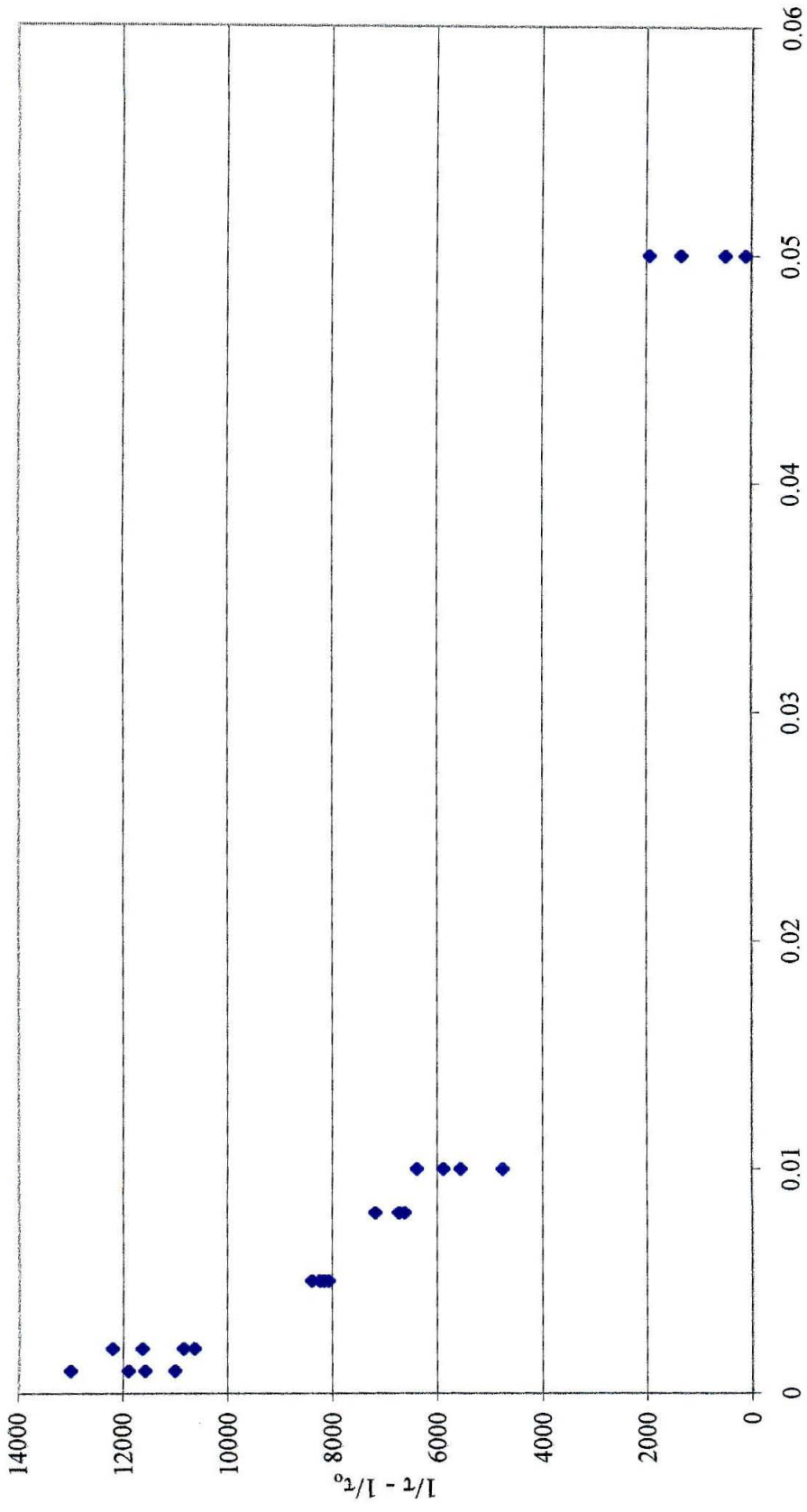

Figure 2.5. Decrease in the concentration of HO_2 versus time due to the $HO_2 + HO_2$ reaction. The change in the inverse ringdown time as a function of delay between excimer firing and IR ringdown probe at 3417 cm^{-1} is plotted.

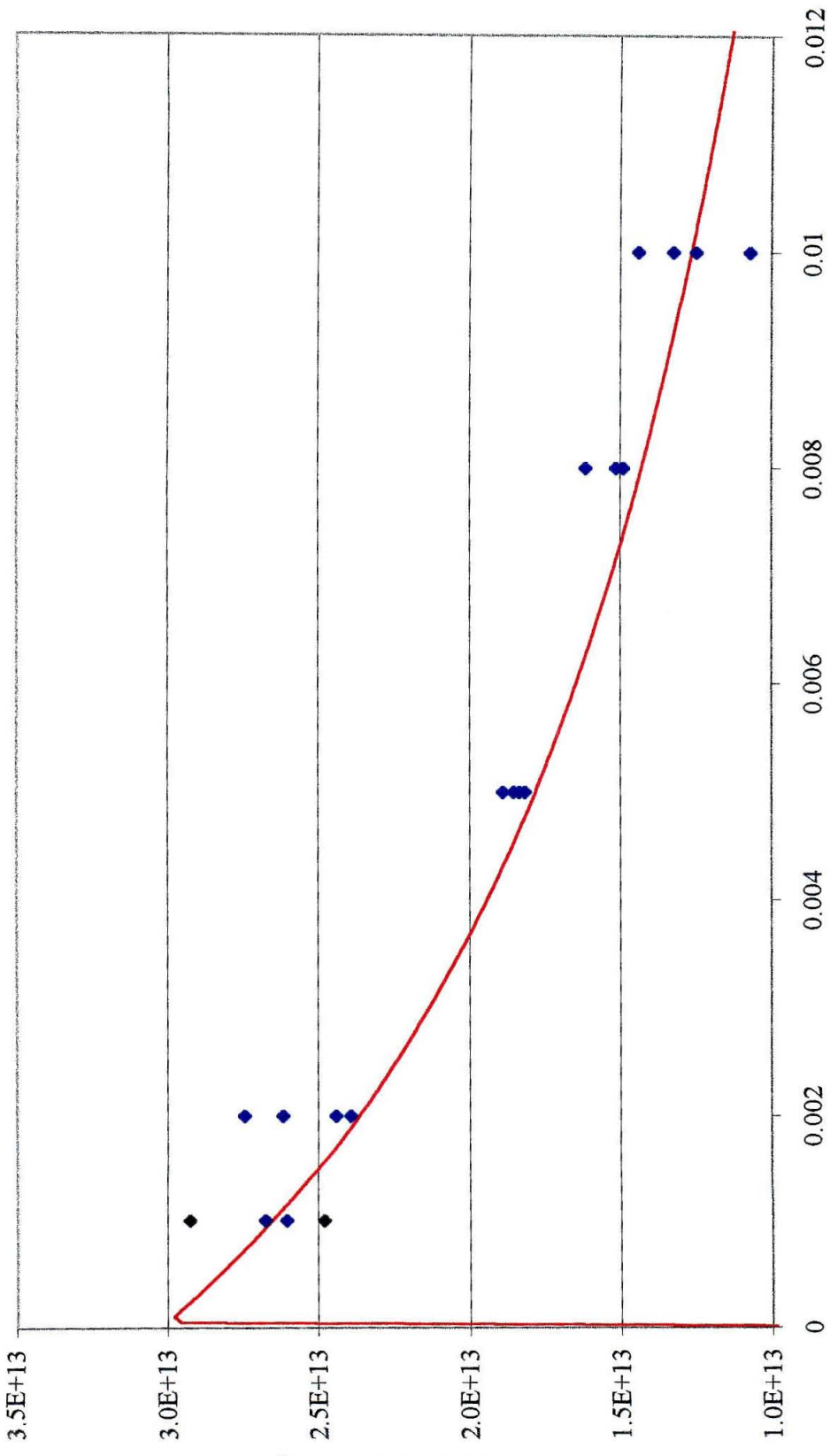

Figure 2.6. FACSIMILE model of the concentration of HO_2 as a function of time with 9% ozone photolysis (red line) is compared to experimental data (blue points).

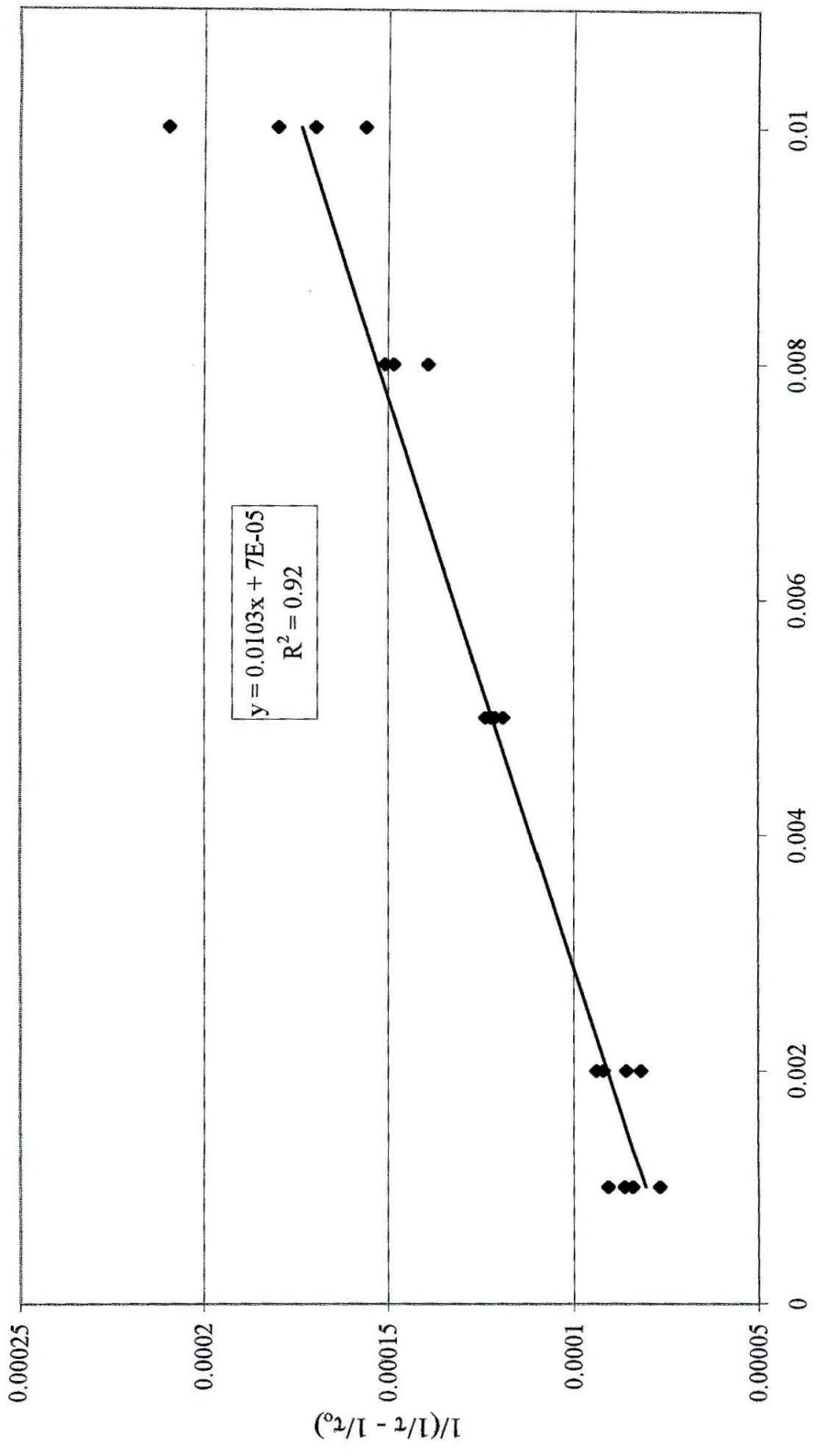

Figure 2.7. Plot of $1/(1/\tau - 1/\tau_o)$ as a function of time and a least squares fit line for the determination of kinetic parameters for the $HO_2 + HO_2$ reaction.

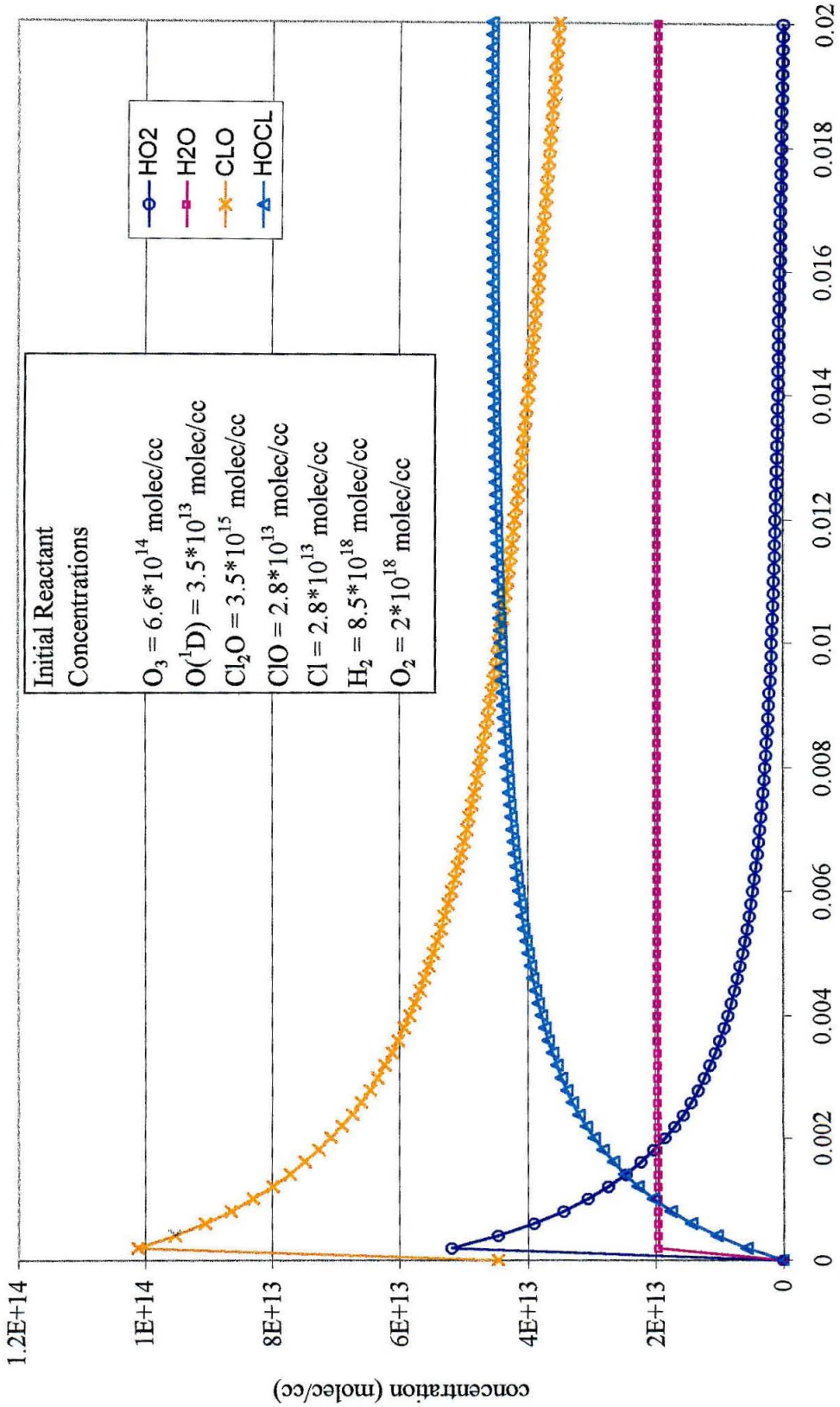

Figure 2.8. FACSIMILE output for the reaction of HO_2 + ClO.

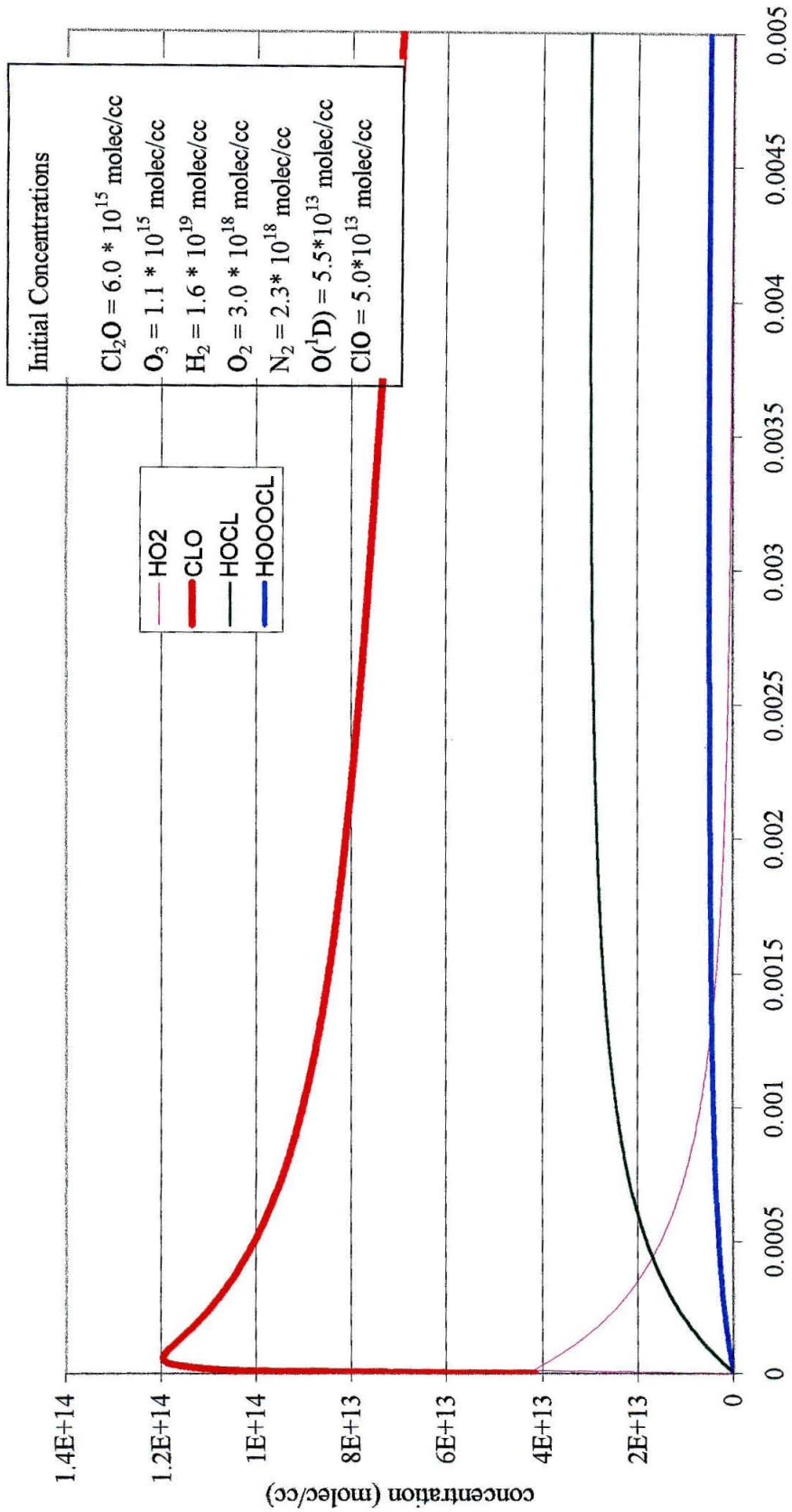

Figure 2.9. FACSIMILE model of the HO_2 + ClO reaction at 208 K.

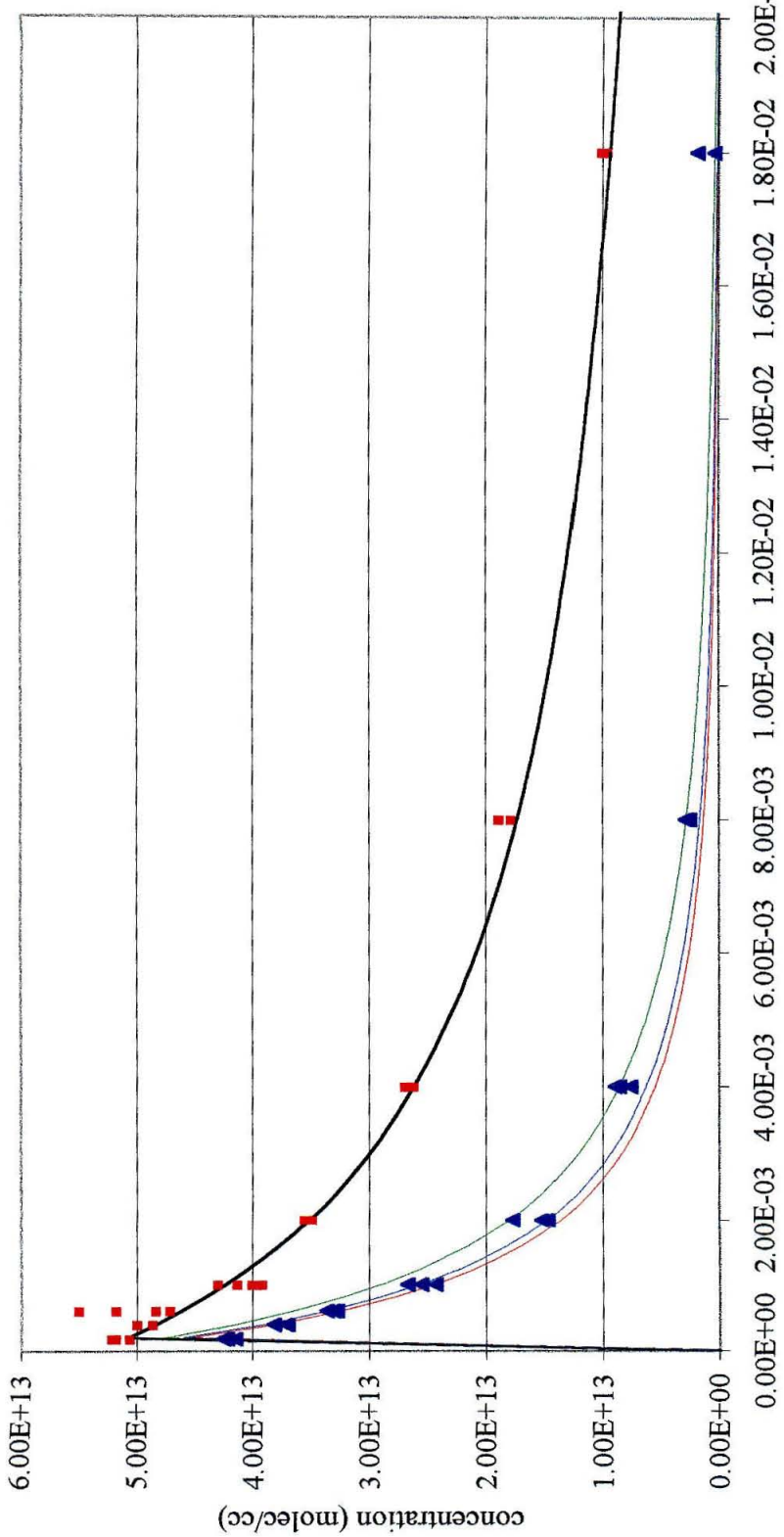

Figure 2.10. HO_2 decays from the reaction of $HO_2 + HO_2$ (red squares) and from a combination of $HO_2 + HO_2$ and $HO_2 +$ ClO (blue triangles). The black line is a time-dependent HO_2 concentration profile from FACSIMILE models of the reaction conditions. The green, blue, and red lines are FACSIMILE models with rate constants for the HO_2 + ClO reaction of $5*10^{-12}$, $7*10^{-12}$, and $8*10^{-12}$ cm^3 $molec^{-1}$ s^{-1}, respectively.

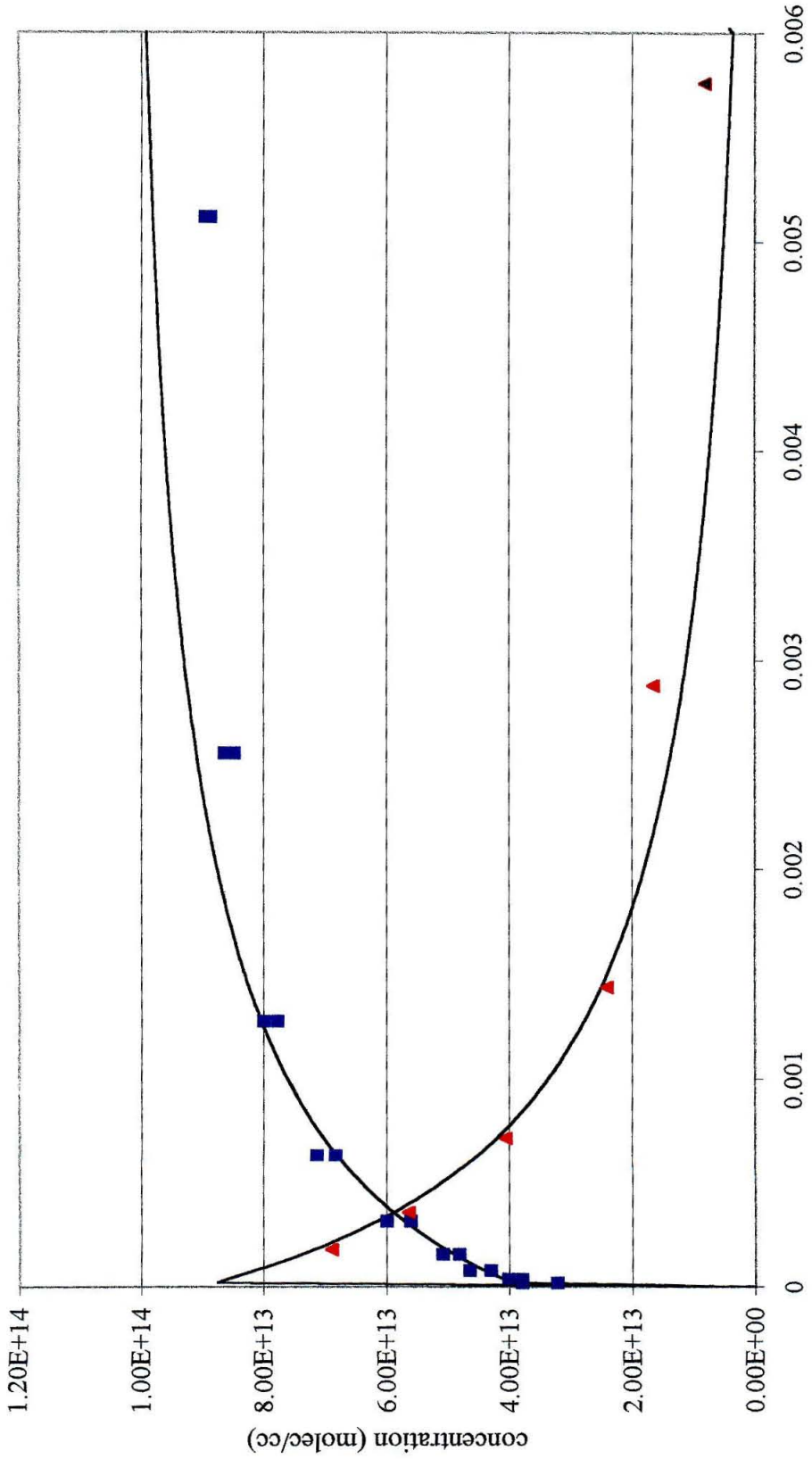

Figure 2.11. Formation of HOCl (blue squares) and decay of HO_2 (red triangles) from the reaction of HO_2 + ClO along with FACSIMILE models (solid lines).

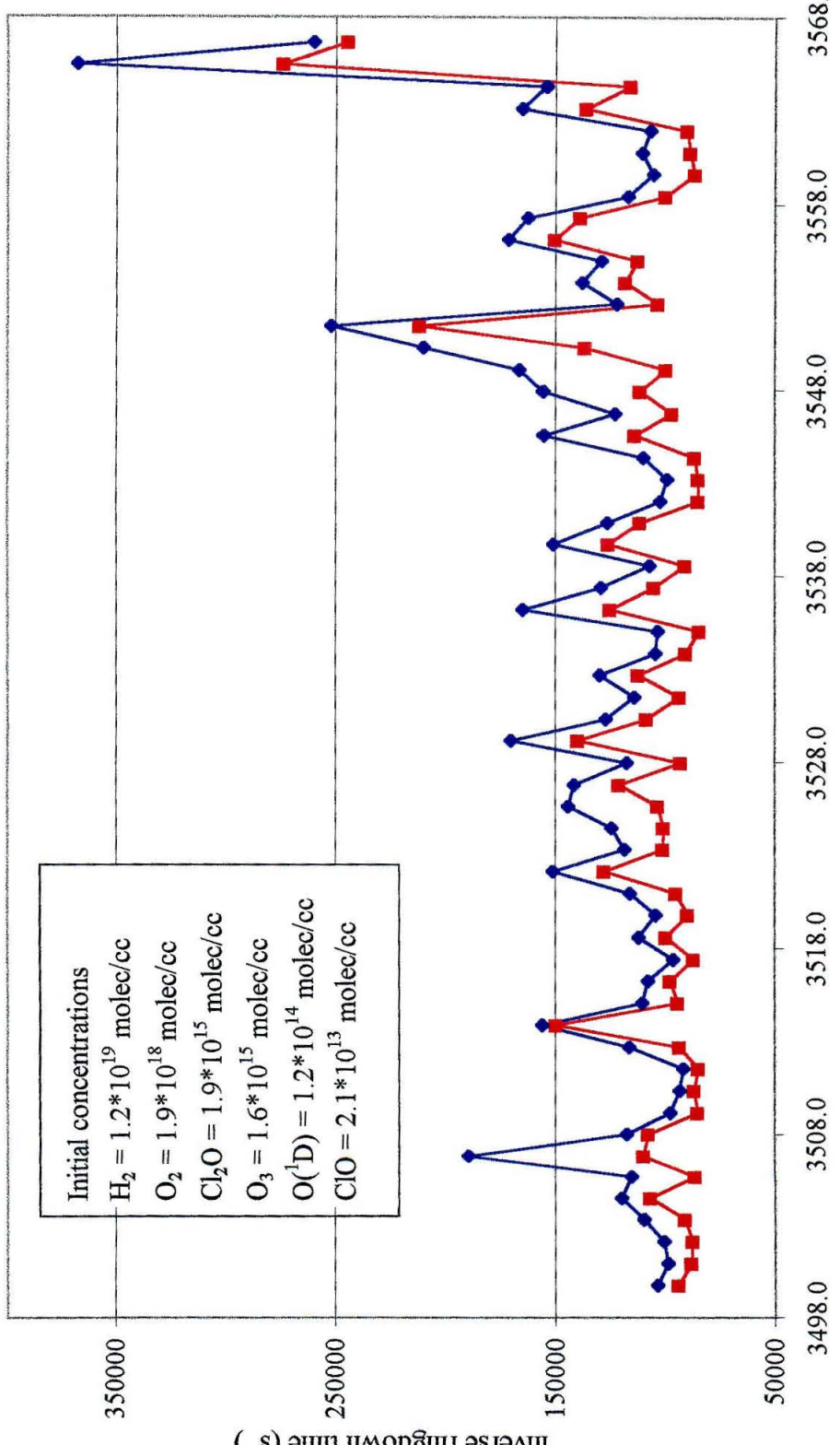

Figure 2.12. Spectra from HO_2 + ClO reaction at 298 K. Blue is excimer on (800 μs delay) and red is excimer off. Background absorptions are due to water and HOCl impurities.

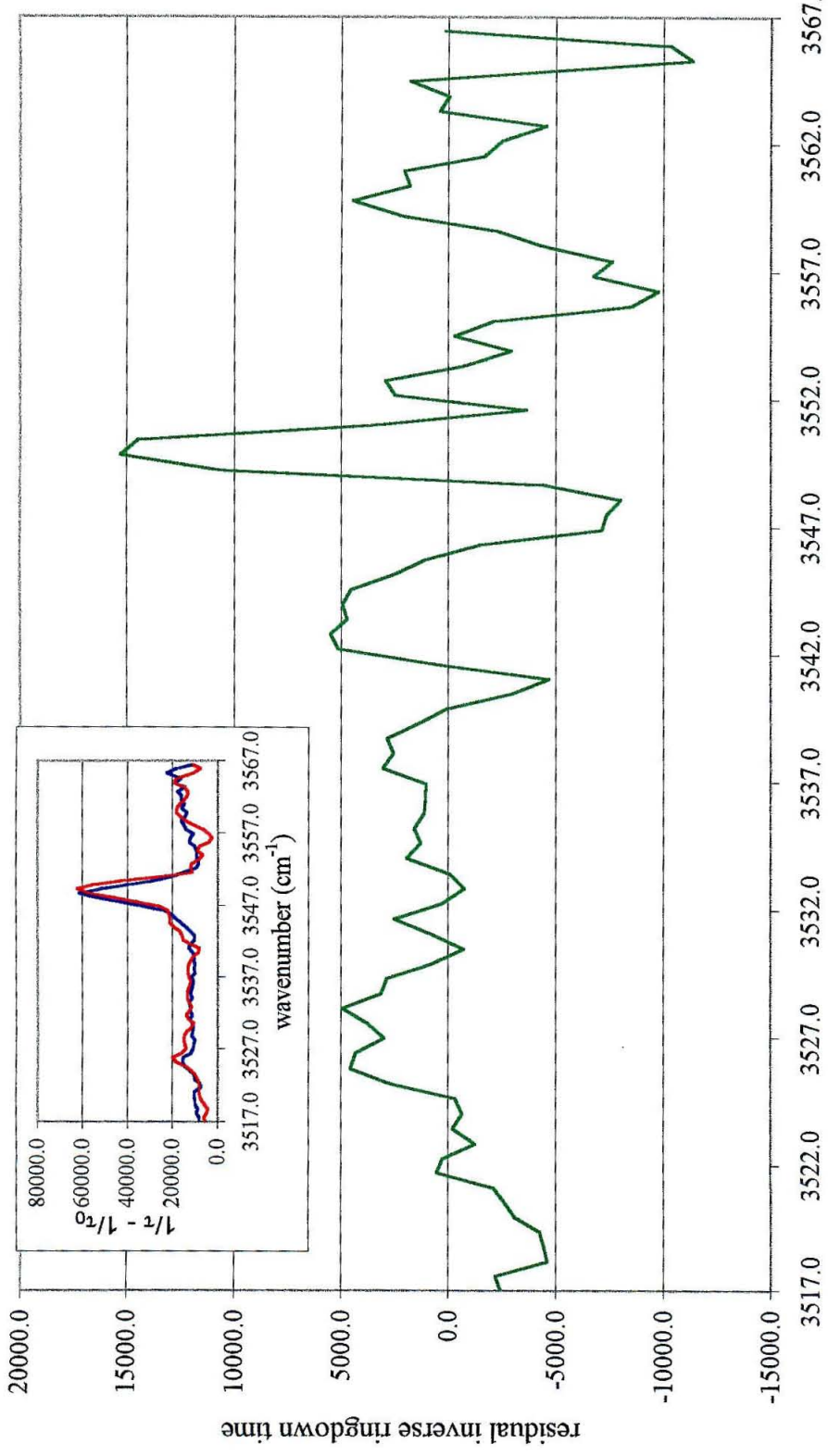

Figure 2.13. Residual of weighted reference spectra of HO_2, H_2O, and HOCl subtracted from experimental spectrum. The inset shows the experimental spectrum in red and the reference spectrum in blue.

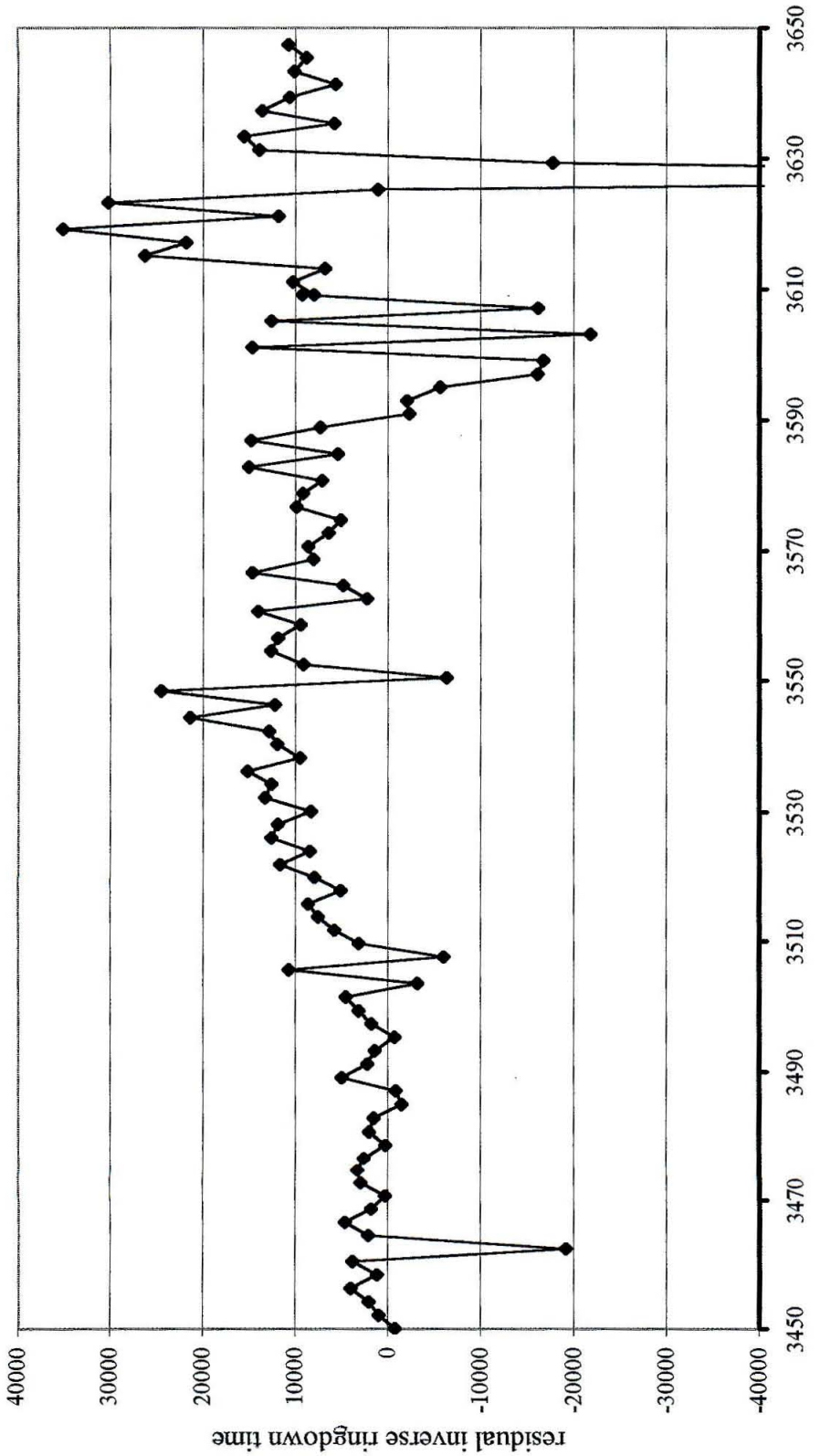

Figure 2.14. Residual spectrum of the HO_2 + ClO reaction at -60 °C {(excimer on - excimer off) - weighted reference spectrum of HO_2, HOCl, and H_2O}.

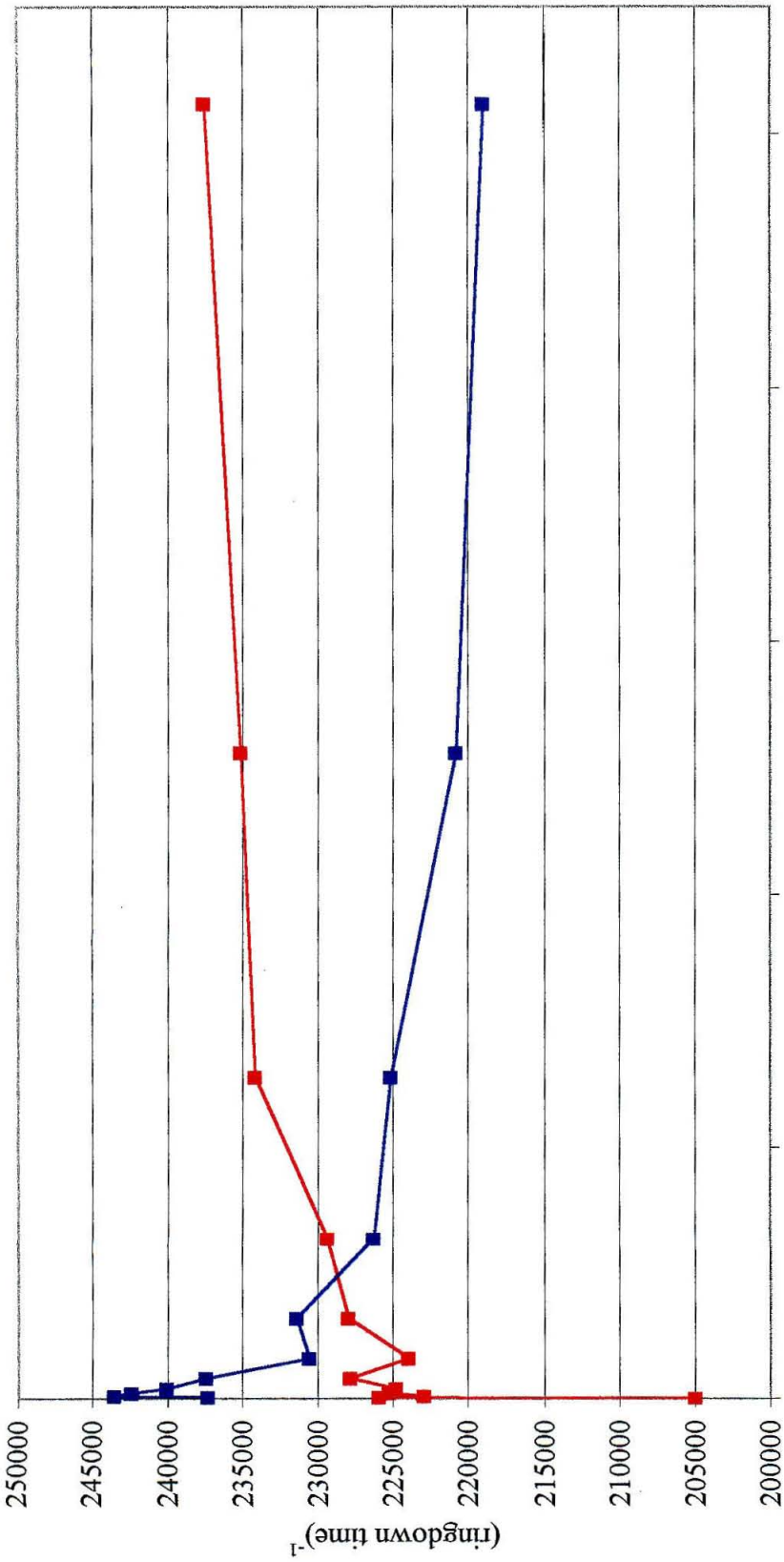

Figure 2.15. Time profiles of peaks from the HO_2 + ClO reaction. Blue data is the time dependence of the absorption at 3417 cm^{-1} (HO_2). Red data is the time dependence of the signal at 3540 cm^{-1}.

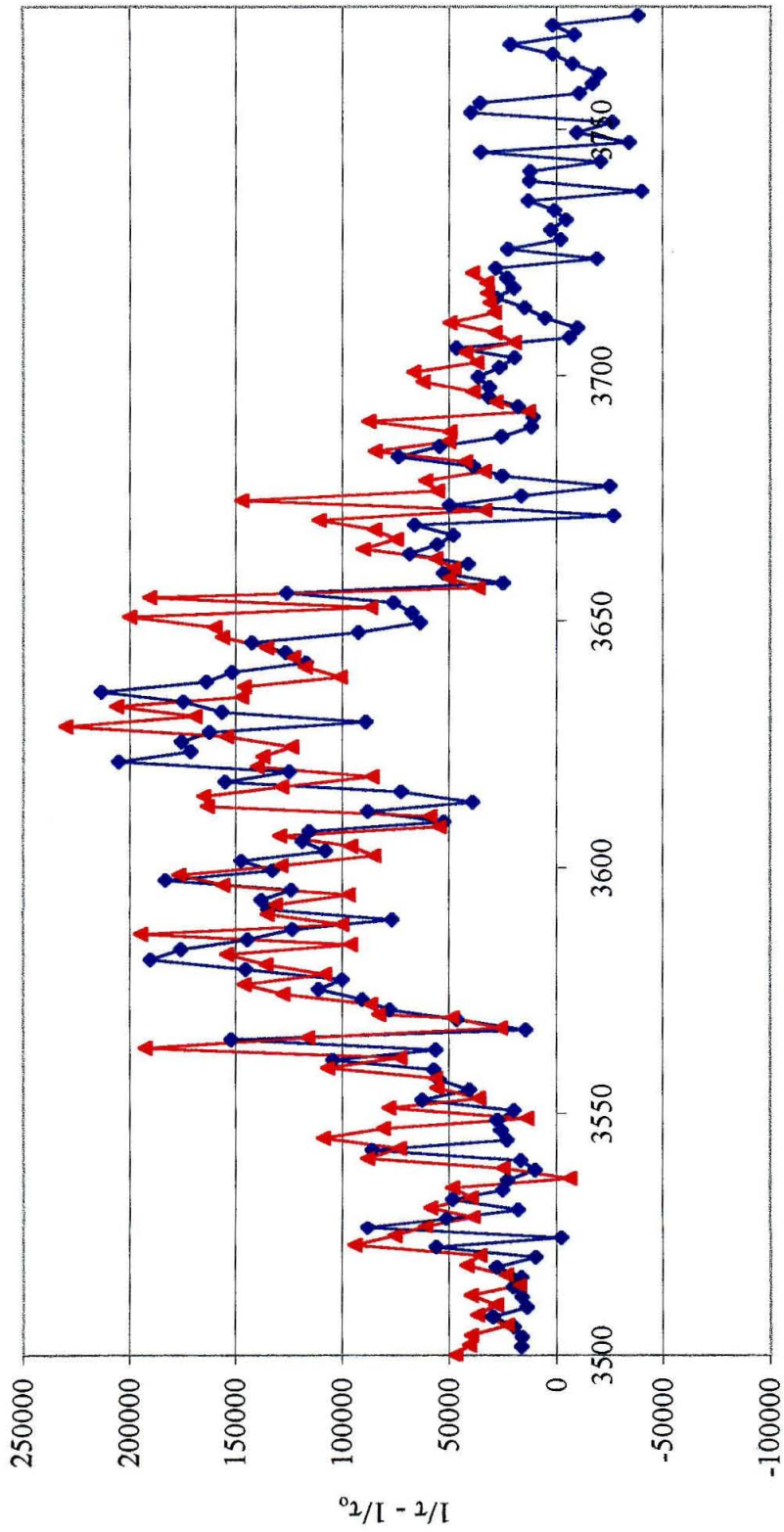

Figure 2.16. Blue data is a difference spectrum (excimer on - excimer off) of HO_2 + ClO reaction at -60 °C with a 10 microsecond delay between the excimer firing and the ringdown detection. Red data is a reference spectrum of H_2O_2 from the photolysis of O_3 in the presence of H_2 and O_2.

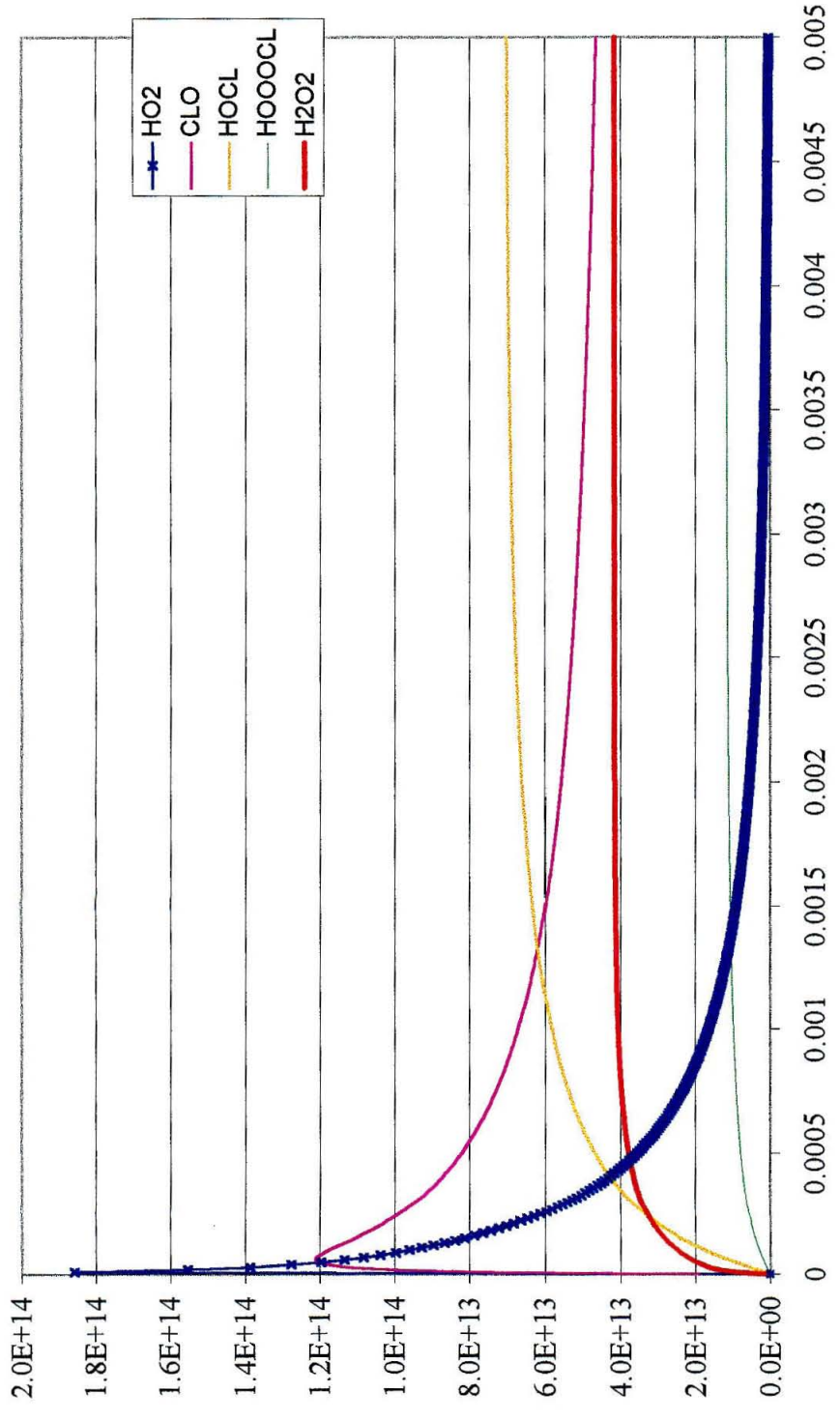

Figure 2.17. FACSIMILE model of HO_2 + ClO including the H_2O_2 product channel. H_2O_2 is six times as large as HOOOCl one millisecond after the photolysis occurs.

CHAPTER 3

STUDIES OF THE REACTION PATHWAYS OF ALKOXY RADICALS

3.1 INTRODUCTION

Investigations into the mechanisms of tropospheric ozone formation have become increasingly important with the realization that ozone poses a critical threat to human health, particularly with respect to its adverse effects on the respiratory system.[1,2,3] Nitrogen oxides and hydrocarbons released from the burning of fossil fuels are involved in a complex series of reactions that lead to the formation of ozone in the troposphere.[4] Alkoxy radicals (RO) are important intermediates in these reactions, yet their reaction pathways are poorly understood.[6] It is essential to determine as precisely as possible reaction rates, branching ratios, and product yields of the reactions leading to the formation of tropospheric ozone so that quantitative models can be developed and steps can be taken to reduce tropospheric ozone formation.[4]

Ozone formation in the troposphere occurs via the photolysis of NO_2 yielding NO and $O(^3P)$ followed by the reaction of $O(^3P)$ with O_2:

$$NO_2 \rightarrow NO + O(^3P) \quad (3.1)$$

$$O(^3P) + O_2 \rightarrow O_3 \quad (3.2)$$

The formation of NO_2 is directly coupled with the oxidation of hydrocarbons in the troposphere, and therefore tropospheric ozone formation requires the presence of hydrocarbons. An example of a reaction scheme leading to the formation of NO_2 is shown below:[5]

$$OH + RCH_3 \rightarrow H_2O + RCH_2 \quad (3.3)$$

$$RCH_2 + O_2 + M \rightarrow RCH_2O_2 + M \quad (3.4)$$

$$RCH_2O_2 + NO \rightarrow RCH_2O + NO_2 \quad (3.5)$$

$$RCH_2O + O_2 \rightarrow RCHO + HO_2 \quad (3.6)$$

$$\underline{HO_2 + NO \rightarrow OH + NO_2 \quad (3.7)}$$

$$\text{Net: } RCH_3 + 2NO + 2O_2 \rightarrow RCHO + 2\,NO_2 + H_2O$$

The aldehyde (RCHO) product can then react with a hydroxy radical:

$$OH + RCHO \rightarrow RCO + H_2O \quad (3.8)$$

The RCO can then directly or indirectly decompose to R + CO. The newly formed hydrocarbon (R) can reenter the above chain reaction (with one less CH_3 group than it had initially) to form additional NO_2 molecules. Furthermore, the CO product may be oxidized to CO_2 via a reaction pathway that is coupled to the conversion of another NO to NO_2. Therefore, the oxidation and decomposition of one hydrocarbon molecule can generate many NO_2 molecules, indirectly leading to the formation of many ozone molecules.

A significant uncertainty in the hydrocarbon oxidation reaction sequence is the fraction of alkoxy radicals that react with O_2 to produce RCHO and HO_2, and the fraction of alkoxy radicals that follow other reaction pathways such as isomerization or decomposition, as shown for the n-butoxy radical:

$$CH_3CH_2CH_2CH_2O \xrightarrow{O_2} CH_3CH_2\,CH_2CHO + HO_2 \quad (3.9)$$

$$CH_3CH_2CH_2CH_2O \rightarrow CH_2CH_2CH_2CH_2OH \text{ [isomerization]} \quad (3.10)$$

$$CH_3CH_2CH_2CH_2O \rightarrow CH_3CH_2CH_2 + HCHO \text{ [decomposition]} \quad (3.11)$$

Recent modeling studies and limited experimental data point to a large discrepancy in the relative pathways depending on the structure of the alkoxy radicals.[6,7,8,9,10] For example, alkoxy radicals that undergo isomerization via a 6-

membered ring transition state such as the n-butoxy radical are predicted to have a relatively large branching ratio for the isomerization pathway. On the other hand, alkoxy radicals that would have a geometrically strained transition state, such as the propoxy and iso-butoxy radicals, are predicted to have little or no isomerization products. Additionally, the isomerization reaction increases when isomerization results in the formation of secondary or tertiary alkyl radicals (e. g., n-pentoxy → 5-hydroxy-pent-2-yl) as opposed to primary alkyl radicals (e. g., n-butoxy → 4-hydroxy-but-1-yl).[6]

We have chosen to focus our studies on reactions of the various isomers of the butoxy radical and of the n-pentoxy radical. These molecules represent alkoxy radicals that are not expected to undergo isomerization (tert-butoxy radical and iso-butoxy radical), a molecule whose rate of isomerization is comparable to the rate of its reaction with O_2 in the presence of 600 Torr of O_2 (n-butoxy radical), and a molecule whose rate of isomerization is expected to be much faster than the rate of its reaction with O_2 in 600 Torr of O_2 (pentoxy radical). Table 3.1 presents a summary of the experimental and calculated values previously obtained of the three reaction pathways available for the tert-butoxy, iso-butoxy, n-butoxy, and n-pentoxy radicals.

Isomerization products have not been observed for the iso-butoxy radical or tert-butoxy radicals, supporting the assumption that a six-membered ring is necessary for isomerization to occur. Smog chamber studies at 300 K and 1 atm have obtained the ratio of the rate of decomposition to the rate of the reaction (k_{O2}/k_d) with O_2 for the iso-butoxy radical of $3.5*10^{-19}$ cm^3 $molec^{-1}$.[11,12] Atkinson calculated rates of various alkoxy radical reactions based on a derived relationship between the rate constant and the exothermicity of alkoxy radical reactions. Atkinson calculated the rate of the

decomposition of the iso-butoxy radical to be $2.3*10^{4}$ s^{-1} and the rate of the reaction of the iso-butoxy radical with O_2 to be $7.8*10^{-15}$ cm^3 $molec^{-1}$ s^{-1}, resulting in a value for (k_{O2}/k_d) of $3.1*10^{-19}$ cm^3 $molec^{-}$.[6] These data are in good agreement with recent experimental data, in which laser-induced fluorescence was used to determine a value of $k_{O2} = 1.2\pm 0.4 *10^{-14}$ cm^3 $molec^{-1}$ s^{-1}at 298 K, and a temperature-dependent rate constant $k_{O2} = 1.33*10^{-15} \exp(5.48/T)$ cm^3 $molec^{-1}$ s^{-1}.[13]

The rate for the decomposition of the tert-butoxy radical at 298 K was determined experimentally by Batt et al.[6] and adjusted by Atkinson[22] based on the rate of the reaction of the tert-butoxy radical with O_2, to yield $7.9*10^{2}$ s^{-1}. We are not aware of any data reported in the literature concerning the rate of the reaction of the tert-butoxy radical with O_2; however, the rate of this reaction is expected to be similar to that of the reaction of O_2 with the iso-butoxy radical.[6]

Experimental studies of the n-butoxy radical at 1 atm have obtained values for k_{O2}/k_{isom} ranging from $5.2*10^{-20}$ to $6.7*10^{-20}$ cm^3 $molec^{-1}$.[7,11,12] A recent study at 50 mbar by Hein et al. monitored the concentrations of NO_2 and OH with LIF and long-path absorption and obtained values of $1.4*10^{-14}$ cm^3 $molec^{-1}$ s^{-1} for k_{O2} and $3.5*10^{4}$ s^{-1} for k_{isom}.[15] At this low pressure, the ration $k_{O2}/k_{isom} = 4.0*10^{-19}$ cm^3 $molec^{-1}$. Calculations by Atkinson of the n-butoxy radical reaction pathways have obtained a rate constant of $5.8*10^{2}$ s^{-1} for the decomposition pathway, $9.3*10^{-15}$ cm^3 $molec^{-1}$ s^{-1} for its reaction with O_2, and $2.0*10^{5}$ s^{-1} for the isomerization pathway.[6]

Theoretical and experimental studies of the n-pentoxy radical have been more limited than for the iso-butoxy and n-butoxy radicals. The rate constant for the addition of O_2 to the n-pentoxy radical generally has been assumed to be similar to that of the

reaction of the n-butoxy radical with O_2.[6] The rate constant for the isomerization of the n-pentoxy radical is predicted to be an order of magnitude larger than for the n-butoxy radical because the product of the n-pentoxy radical isomerization is a secondary alkyl radical, whereas the isomerization product of the n-butoxy radical is a primary alkyl radical.[6] Hein et al. found that the ratio k_{O2}/k_{isom} was smaller than they could detect experimentally, and they placed an upper limit of $1*10^{-13}$ cm^3 $molec^{-1}$ s^{-1} for k_{O2} and a lower limit of $1*10^5$ s^{-1} for k_{isom}.[15]

Many previous experimental studies of the reaction pathways undergone by alkoxy radicals have relied on end-product analysis.[7,8,9,10,14,15,16] Other studies have observed secondary reaction products of alkoxy radical isomerizations and reactions with O_2 such as OH and NO_2.[15] Often, several reaction pathways can generate the same products, and so it can be difficult to deduce reaction mechanisms by relying on end-product data.[17] Some experiments have used laser-induced fluorescence to detect reaction pathways of small alkoxy radicals (up to 2-butoxy).[13, 15, 18]

Here, we report direct studies of butoxy and pentoxy radical reaction pathways, using our infrared cavity ringdown spectroscopy apparatus, in order to compile information about the reaction rates of the various product channels available to the alkoxy radical. Our apparatus enabled us to obtain data on a time scale of tens of microseconds after the formation of the alkoxy radicals, and the range of our ringdown mirrors afforded detection of product absorptions in the 3300 - 3750 cm^{-1} range.

3.2 EXPERIMENTAL

The alkoxy radical was photolyzed in situ from the nitrite precursor with 248 nm or 351 nm radiation from an excimer laser:

$$RONO \rightarrow RO + NO$$

The butyl nitrite precursors were purchased from Aldrich. n-Pentoxy nitrite was synthesized from pentanol in aqueous sodium nitrite, using a modification of the synthesis of n-butyl nitrite described in Organic Syntheses Vol. 2.[19] Briefly, a mixture of 100 mL H_2O, 136 mL concentrated H_2SO_4, and 457 mL pentanol was cooled to 0^0C and then was introduced to a solution of 380 g of sodium nitrite in 1.5 L of H_2O. The resulting mixture separated into two layers. The aqueous layer was removed and the pentyl nitrite layer was washed with a solution of 2 g sodium bicarbonate and 25 g of sodium chloride in 100 mL of water and dried with 20 g of anyhydrous sodium sulfate. The crude product was distilled at 25 °C and 43 mm Hg, and the absence of an alcohol absorption peak in the infrared region confirmed that no residual pentanol remained in the distilled product. The alkyl nitrites were placed in a bubbler, which was subsequently placed in a temperature-controlled methanol bath. Helium or argon was bubbled through the liquid alkyl nitrites in order to introduce the nitrites into the reaction cell. The temperature of the methanol bath was adjusted to control the vapor pressure of the alkyl nitrites, thus controlling the concentration of alkyl nitrites in the helium. Typical temperatures ranged from -40 °C to -10 °C. Nitrogen and oxygen were used as bath gases, and the relative ratios of these gases in the reaction cell were used in the determination of the ratio of $k_{isom}/k_{O2}[O_2]$. A typical ratio of the nitrogen/oxygen mixture

to the argon/alkyl nitrite mixture in the reaction cell was 30:1. Argon was used to purge the ringdown mirrors. Helium, nitrogen, oxygen, and argon gases were purchased from Air Liquide (99% pure). The total flow rate of gases through the cell was approximately 3400 sccm, and the total pressure in the cell was typically at 600 Torr. The residence time of gases in the photolysis region was approximately 0.5 seconds.

The concentration of alkyl nitrites was determined by an absorption measurement of the helium/alkyl nitrite flow at 254 nm. The cross section of methyl nitrite at 254 nm is $1*10^{-18}$ cm^2, and the cross section for the other alkyl nitrites is expected to be similar.[20,21] Alkyl nitrite concentrations in the reaction cell were kept low because the alkyl nitrites absorbed infrared radiation in the 3300-3750 cm^{-1} range which interfered with our detection of reaction products. Typical precursor concentrations in the cell were on the order of 10^{16} molec/cc. The cross sections for alkyl nitrite photolysis at our photolysis wavelengths of 248 nm and 351 nm are $1.3*10^{-18}$ cm^2 and $8*10^{-20}$ cm^2, respectively.[20] Typical excimer energies entering the reaction cell were 125 mJ of 248 nm radiation and 50 mJ of 351 nm radiation, and the rectangular excimer beam was approximately 3 cm x 1 cm. The resulting amount of alkyl nitrite photolysis is 5% at 248 nm and 0.1% at 351 nm.

3.3 RESULTS

A. 248 nm photolysis

Spectra in N_2

Spectra of the end products of the reactions of n-, iso-, and tert-butoxy radicals formed from the photolysis of the butyl nitrite precursors at 248 nm were taken by obtaining infrared cavity ringdown curves at a repetition rate of 10 Hz. The total pressure in the cell was 600 Torr, the residence time of gases in the reaction cell was 0.5 s, and so the 10 Hz experiments probed products that had been formed from several rounds of precursor photolysis. We chose to conduct these end-product analyses as our initial experiments because of the large absorption signals that were generated by observing many rounds of products at once, and experiments were performed more expediently at a higher repetition rate. The 10 Hz data with N_2 as a bath gas are shown in Figure 3.1.

Spectra of products formed 10 microseconds after the photolysis of the precursor were taken by repeating the scans at 2.5 Hz. The spectra of the products that formed within 10 microseconds after photolysis are shown in Figure 3.2. We found that the spectra in Figure 3.2 are scaled-down versions of the 10 Hz spectra shown in Figure 3.1, indicating that the spectra observed at 10 Hz were generated from species formed within the first 10 microseconds after the photolysis of the nitrite precursors. The different butyl nitrite precursor concentrations in the cell were not standardized for these experiments because we were concerned mainly with qualitative identification of the spectral peaks; typical butyl nitrite concentrations were approximately $5*10^{15}$ molec/cc (as calculated

from the absorption of the butyl nitrites at 254 nm prior to introducing them into the reaction cell) for the data in Figure 3.1 and Figure 3.2.

Figures 3.1 and 3.2 reveal two regions of spectroscopic absorption: one at 3470 cm^{-1} for all butoxy radicals and one at 3675 cm^{-1} for the n-butoxy radical reactions. Time profiles were taken of the rise of each peak observed in the spectra of the butoxy radical reactions in N_2. These profiles were obtained by varying the delay between the photolysis of the nitrite precursors and the probe with the cavity ringdown spectrometer. All of the peaks in the spectra were present at their maximum intensity within 10 microseconds of the photolysis, which is the highest time resolution that we can achieve with our apparatus.

The peak at 3675 cm^{-1} in the n-butoxy radical reaction spectrum was identified as an -OH absorption. We assign this peak to the initial isomerization product of the n-butoxy radical, the 4-hydroxy-butyl radical, because the location of the -OH peak of this product is similar to that for butanol, which is centered at 3669 cm^{-1}. The presence of the -OH peak in the n-butoxy radical spectrum, and its absence in the tert-butoxy radical and iso-butoxy radical spectra, indicate that only the n-butoxy radical is undergoing isomerization, as was expected from previous arguments.

Both the n-butoxy and iso-butoxy radicals give products that have an absorption centered at 3471 cm^{-1}, with a strong Q branch. The tert-butoxy radical also has a large absorption around 3460 cm^{-1}, but this absorption does not have a Q branch. The peak observed for the n-butoxy and iso-butoxy radicals at 3471 cm^{-1} was identified as formaldehyde. This identification was established by introducing an aqueous solution of formaldehyde into the ringdown cell and confirming that its absorption spectrum was

identical to that of the n-butoxy radical and iso-butoxy radical spectra. The peak in the tert-butoxy radical product spectrum at 3460 cm^{-1} was identified as acetone based on a comparison to a reference spectrum of acetone.

Formaldehyde is a decomposition product of the n-butoxy radical and the iso-butoxy radical. The n-butoxy radical was not expected to undergo significant decomposition under our reaction conditions because the rate constant for decomposition has been reported to be three orders of magnitude smaller than the rate constant for isomerization.[6] The rate constants for decomposition of n-butoxy radical and iso-butoxy radical would correspond to the formation of formaldehyde over several milliseconds. Therefore, the observation that the formaldehyde was completely formed within 10 microseconds was unexpected. The prompt formaldehyde formation in the n-butoxy radical and iso-butoxy radical spectra suggests that the photolysis at 248 nm may be generating highly energetic butoxy radicals which undergo spontaneous dissociation. Details concerning the plausibility of the spontaneous dissociation of the butoxy radicals at 248 nm using energetics arguments will be discussed later in this chapter.

Acetone is a decomposition product of the tert-butoxy radical. The rate of decomposition of the tert-butoxy radical at 298 K was measured relative to its reaction with NO, and it was reported to be 1100 s^{-1}.[22] Atkins reevaluated the rate constant based on the current value for the rate of the reaction of the tert-butoxy radical with NO, which is $3.8*10^{-11}$ cm^3 $molecule^{-1}$ s^{-1}.[6] The resulting rate constant for the decomposition of the tert-butoxy radical was reported to be 790 s^{-1}. Under our reaction conditions, $2.5*10^{14}$ molec/cc of NO were produced from the photolysis of tert-butyl nitrite. At this NO concentration, the rate for the reaction of the tert-butoxy radical with NO is 9500 s^{-1},

which should dominate over the decomposition reaction. Furthermore, the decomposition channel is slow, and so there should be very little decomposition product observed 10 microseconds after the photolysis of the precursor. These results suggest that, as in the case of the n-butoxy radical, excess energy may be present in the tert-butoxy radical as a result of the photolysis of tert-butyl nitrite at 248 nm, and the tert-butoxy radical may be dissociating immediately after its formation.

Spectra in O_2

End-product spectra of the butoxy radicals in O_2 taken at a 10 Hz repetition rate are shown in Figure 3.3, and spectra taken at 2.5 Hz, 10 microseconds after the photolysis of the nitrite precursor, are shown in Figure 3.4. As with the N_2 spectra, the O_2 spectra at 10 Hz have the same peaks as the 2.5 Hz spectra, and so the spectra observed at 10 Hz were generated from species formed within the first 10 microseconds after the photolysis of the nitrite precursors. For each of the butoxy radicals, all of the peaks that were observed in the N_2 spectra were also present in the O_2 spectra. Additional peaks were also present in the O_2 spectra, presumably due to the reaction of O_2 with the butoxy radicals or the reaction of O_2 with products of other reaction channels of the butoxy radicals, such as decomposition products.

As in the nitrogen spectra, an -OH peak was observed only for the n-butoxy radical, supporting the conclusion that this peak is from an isomerization product. In addition to the peak at 3471 cm^{-1} that was observed in the N_2 spectra and has been assigned to formaldehyde, both the n-butyl radical and the iso-butyl radical contained peaks at 3550 cm^{-1} and 3595 cm^{-1} when oxygen was used as a bath gas. The tert-butoxy

radical contained a formaldehyde peak in the oxygen spectra that was not present in its nitrogen spectra.

Time delay profiles showed that all peaks reached their maximum strengths within 10 microseconds after the photolysis of the precursor, with the notable exception of the peaks at 3550 and 3590 cm^{-1} observed in the n-butoxy and iso-butoxy radical product spectra. Time profiles of the 3550 cm^{-1} and 3595 cm^{-1} peaks are shown in Figure 3.5. The data shows that the 3550 cm^{-1} and 3595 cm^{-1} peaks have similar time profiles, and that they reach half of their maximum value approximately 20 microseconds after the formation of the butoxy radicals. These results indicate that the peaks at 3550 cm^{-1} and 3595 cm^{-1} represent the formation of a product by a slower reaction process than the other spectral peaks. Thus, the 3550 cm^{-1} and 3595 cm^{-1} peaks may result from the reaction of oxygen with a reaction intermediate, such as a decomposition product.

The tert-butyl radical spectra indicate the presence of formaldehyde based on its characteristic Q branch at 3471 cm^{-1}. One possible pathway to the formaldehyde may be initiated by the reaction of the methyl radical (a decomposition product of the tert-butoxy radical) with O_2 to form methyl peroxy radical (Reaction 3.12). The methyl peroxy radical could react with NO to form the methoxy radical, and the methoxy radical could react with O_2 to form formaldehyde and HO_2 (Reaction 3.13). Additionally, the self-reaction of the methyl peroxy radical has a formaldehyde product channel (Reaction 3.14).[23]

$$CH_3 + O_2 \rightarrow CH_3O_2 \quad \text{(Reaction 3.12)}$$

$$CH_3O_2 + NO \rightarrow CH_3O + NO_2 \quad \text{(Reaction 3.13)}$$

$$CH_3O_2 + CH_3O_2 \rightarrow 0.6\,(CH_2O + CH_3OH + O_2) \quad \text{(Reaction 3.14)}$$

These reactions were simulated with a FACSIMILE model to determine the time profile for the formation of formaldehyde. The result of this model is compared to the observed time profile of the formation of the 3471 cm^{-1} peak in the tert-butoxy radical spectrum in O_2 and is shown in Figure 3.6. As is evident in Figure 3.6, the formation of formaldehyde by the above processes is slower than our observed time profile for formaldehyde formation, in which formaldehyde formation occurs immediately after the photolysis of the tert-butyl nitrite precursor. Therefore, this scheme is unlikely to be the mechanism that produces the formaldehyde that we are observing. A different process, such as addition of oxygen to the tert-butyl radical followed by immediate dissociation, is presumably leading to the formation of the observed formaldehyde.

Analysis of 248 nm Data

The 248 nm data indicate that decomposition of the butoxy radicals is occurring to a greater extent than would be expected based solely on the rates of decomposition compared to the rates of other reaction pathways. Thus, we investigated the possibility that photolysis of the butoxy nitrite precursors at 248 nm was introducing excess energy in the butoxy radicals, causing them to undergo immediate decomposition. In the early 1960s, McMillan reported that the fraction of excited radicals produced at 26 °C in nitrogen from the 253 nm photolysis of tert-butyl nitrite was 0.87, whereas at 366 nm photolysis, the fraction of excited tert-butoxy radicals produced was 0.04.[24,25] Subsequent studies by McMillan and coworkers on the photolysis of tert-pentyl nitrite found that the fraction of excited pentoxy radicals produced with 253 nm photolysis was 0.86, while the fraction of excited pentoxy radicals produced with 366 nm photolysis was

0.03 at 26 °C.[26] These and other studies point to a large discrepancy in the amount of excited alkoxy radicals that are produced from photolysis of alkyl nitrites in the 250 nm wavelength range versus the 350 nm wavelength range.[20]

The probability that excess energy from the photolysis at 248 nm was causing the butoxy radicals to spontaneously decompose led us to investigate the behavior of butoxy and pentoxy radicals at a different photolysis wavelengths. We chose to switch to 351 nm photolysis because photolysis of alkyl nitrites at this wavelength would be expected to produce a significantly smaller fraction of excited molecules. Additionally, switching the excimer laser from 248 nm to 351 nm was easily facilitated by changing from a Kr/F mixture to a Xe/F mixture.

B. 351 nm photolysis

The excimer laser output at 351 nm was 100 mJ, as opposed to the 250 mJ that we obtained at 248 nm. Additionally, the absorption cross section for the alkyl nitrites at 351 nm is a factor of 16 smaller than the absorption cross section at 248 nm. Therefore, by switching to 351 nm photolysis, the percent of butyl nitrite photolysis would be decreased by a factor of 40. Because of this decrease in the amount of photolysis of the nitrite precursors at 351 nm, we could only obtain spectra with a reasonable signal-to-noise ratio when running the experiment at 10 Hz. Thus, all spectra reported here at 351 nm are those of end products of the alkoxy radical reactions. We were able to investigate the -OH peak of the isomerization product using a repetition rate of 1 Hz by averaging many ringdown curves to attain an adequate signal-to-noise ratio, and these results are presented following the spectral results.

Spectra in N_2

The spectra of the end-products of the reactions of iso-butoxy, n-butoxy, and n-pentoxy radicals in nitrogen are shown in Figure 3.7. Unlike the spectra obtained at 248 nm, the spectra in Figure 3.7 do not indicate the presence of any formaldehyde peaks. This supports our earlier hypothesis that the formaldehyde observed from the 248 nm photolysis was formed from immediate dissociation of the butoxy radicals because of the excess energy given to them from photolysis at the higher energy wavelength. The spectra in Figure 3.7 have a significantly lower signal-to-noise ratio than the spectra from the photolysis at 248 nm because of the smaller percent of precursor photolysis. Thus, the only peak that is clearly identifiable is the -OH peak at 3650 cm^{-1}. This peak is observed for only the n-butoxy and n-pentoxy radicals, implying that only these molecules undergo isomerization.

Spectra in O_2

The end-product spectra of the butoxy and pentoxy radicals in oxygen are presented in Figure 3.8. The poor signal-to-noise precludes identification of any peaks in the iso-butoxy radical and tert-butoxy radical spectra. Additionally, a large absorption of the tert-butyl nitrite precursor at 3550-3600 cm^{-1} prevents the acquisition of spectra in this region. Both the n-pentoxy and n-butoxy radical spectra contain the peak at 3650 cm^{-1} that was also observed in the N_2 spectra for these molecules. The rest of the n-pentoxy radical spectrum is too noisy to identify any other peaks. On the other hand, the n-butoxy radical spectrum was taken under particularly good conditions (excellent

repeatability of ringdown curves), and so the presence of other peaks in this spectrum was confirmed.

The n-butoxy radical spectrum in O_2 with photolysis at 351 nm is compared to the spectrum taken at 248 nm in Figure 3.9. The spectra were scaled to match their peak strengths at 3650 cm^{-1}. The comparison reveals remarkable similarities in the spectra. They both contain peaks at 3550 and 3595 cm^{-1}, and the source of these peaks is unknown. The presence of these peaks in the 351 nm spectra suggest that they are not a result of the reaction of O_2 with decomposition products because no formaldehyde formation is observed at 351 nm. Both the 351 nm and 248 nm spectra have a broad peak ranging from 3410 to 3500 cm^{-1}. For the 248 nm spectrum, this peak was assigned to formaldehyde because of the characteristic Q branch at 3471 cm^{-1}. In the 351 nm spectrum, however, there is no evidence of a Q branch, and so the source of this broad absorption is unknown.

Isomerization versus Reaction with O_2

For the molecules that undergo isomerization, namely the n-butoxy radical and the n-pentoxy radical, we investigated the relative rates of their reaction with O_2 versus their isomerization rates (k_{O2}/k_{isom}). These two pathways are depicted below for the butoxy radical.

$$C_4H_9O \xrightarrow{k_{isom}} C_4H_8OH \quad \text{(Reaction 3.12)}$$

$$C_4H_9O + O_2 \xrightarrow{k_{O2}} HO_2 + C_4H_8O \quad \text{(Reaction 3.13)}$$

Studies of k_{O2}/k_{isom} were performed by varying the ratio of O_2 and N_2 in the reaction cell and monitoring the strength of the -OH peak at 3654 cm^{-1}. This wavelength was chosen for our experiments because there was minimal interference with water and precursor absorptions.

The value of k_{O2}/k_{isom} was determined using the following method. The concentration of the isomerization product produced in Reaction 3.12 is equal to the initial butoxy radical concentration multiplied by the rate constant of the isomerization reaction (k_{isom}) divided by the summation of the rate constants of both the isomerization reaction and the reaction with oxygen (k_{O2} $[O_2]$):

$$[C_4H_8OH] = \frac{k_{isom}\,[C_4H_9O]}{ko_2\,[O_2] + k_{isom}} \qquad \text{(Equation 3.1)}$$

Equation 3.1 can be rearranged to yield a linear relationship between the inverse of the concentration of the isomerization product and the ratio k_{O2}/k_{isom}:

$$\frac{1}{[C_4H_8OH]} = \frac{ko_2\,[O_2]}{k_{isom}\,[C_4H_9O]} + \frac{1}{[C_4H_9O]} \qquad \text{(Equation 3.2)}$$

From Equation 3.2, it is evident that a plot of $1/[C_4H_8OH]$ versus $[O_2]$ will result in a line with slope $ko_2/(k_{isom}\,[C_4H_9O])$ and a y-intercept of $1/[C_4H_9O]$. Dividing the slope by the y-intercept will yield the ratio ko_2/k_{isom}. The relationship between $1/\tau - 1/\tau_o$, the difference of the inverse ringdown time of the cavity with the absorbing sample and the inverse ringdown time of the empty cell, is related to the concentration of the absorbing species via the following equation, which is discussed in more detail in Chapter 2 of this thesis (c is the speed of light, σ is the absorption cross section, L_{cell} is

the length of the ringdown cell, and L_{phot} is the length of the photolysis region of the ringdown cell):

$$\frac{1}{\tau} - \frac{1}{\tau_o} = \frac{\{c*\sigma*[C_4H_8OH]*L_{phot}\}}{\{L_{cell}\}} \quad \text{(Equation 3.3)}$$

From Equation 3.3, the quantity $(1/\tau - 1/\tau_o)$ is proportional to $[C_4H_8OH]$. Therefore, we plotted $(1/\tau - 1/\tau_o)^{-1}$ as a function of $[O_2]$, and the resulting ratio of the slope to the y-intercept was equal to k_{O_2}/ k_{isom}.

The results of our studies of the amount of n-butoxy radical isomerization as a function of oxygen concentration in the reaction cell are shown in Figure 3.10. The study was performed at both 1 Hz and 10 Hz repetition rates, and the value $(1/\tau - 1/\tau_o)^{-1}$ was plotted as a function of oxygen concentration. The 1 Hz data was obtained using time delays ranging from 10 to 20 microseconds between the firing of the excimer laser and the infrared cavity ringdown detection, and so it probed products formed within the first 20 microseconds of the generation of the butoxy radical. The 10 Hz data probed the end-products of the reaction. For the 10 Hz data, we obtained a value for k_{O_2}/ k_{isom} of $(4.0\pm0.1)*10^{-20}$ cm^3 $molec^{-1}$, and for the 1 Hz data, we obtained $k_{O_2}/ k_{isom} = (3.6\pm1.4)*10^{-20}$ cm^3 $molec^{-1}$.

The consistency of our value for k_{O_2}/ k_{isom} while running the experiment at both 10 Hz and 1 Hz suggest that all of the observed -OH peak at 3554 cm^{-1} is from the isomerization product of the n-butoxy radical. A discrepancy in the value obtained for k_{O_2}/ k_{isom} at 1 Hz and 10 Hz would have implied that there were other mechanisms producing molecules with a peak at 3554 cm^{-1}, such as an additional product with an -OH

group. Thus, our results support the validity of using analysis of -OH absorptions to measure the extent of alkoxy radical isomerization.

Previous measurements of k_{O_2}/ k_{isom} for the butoxy radical at atmospheric pressure range from $5.2*10^{-20}$ to $6.7*10^{-20}$ cm^3 $molec^{-1}$. Hein et al. reported a value for k_{O_2}/ k_{isom} at 50 mbar pressure of $4.0*10^{-19}$ cm^3 $molec^{-1}$, and they suggest that k_{isom} may have a pressure-dependence.[15] If this is the case, then it would stand to reason that our value for k_{O_2}/ k_{isom}, taken at 600 Torr, would be intermediate between the values at atmospheric pressure and at 50 mbar. A summary of experimental values obtained to date of k_{O_2}/ k_{isom} for the butoxy radical are presented in Table 3.2.

The relative rate of the reaction with O_2 versus the rate of isomerization (k_{O2}/k_{isom}) was also investigated for the pentoxy radical. We observed no difference in the strength of the -OH peak of the pentoxy radical isomerization product at 3554 cm^{-1} in 100% N_2 and 100% O_2 at 600 Torr total pressure. Our uncertainty limits were very large due to poor signal, and we estimate our error at 10% of the strength of the ringdown peak. This gives an upper limit for k_{O2}/k_{isom} of $5.6*10^{-21}$ cm^3 $molec^{-1}$. The only previous experiment of which we are aware that measured k_{O_2}/ k_{isom} for the pentoxy radical is the work done by Hein et al. in which they obtained an upper limit of $1*10^{-18}$ cm^3 $molec^{-1}$ for k_{O_2}/ k_{isom}.[15]

Assuming that k_{O2} for the n-pentoxy radical is similar to k_{O2} for the n-butoxy radical, as has been suggested by Atkinson,[6] our value for k_{O_2}/ k_{isom} yields a lower limit for the rate of the n-pentoxy radical isomerization of 2500 s^{-1}. The suggested value for the rate of the n-pentoxy radical isomerization based on theoretical arguments is approximately 5800 s^{-1}.[6] Current work is underway in our laboratory to increase the

sensitivity of our apparatus so that we can directly measure k_{O_2}/ k_{isom} for the n-pentoxy radical. One improvement we intend to implement is to multi-pass the photolysis beam through the reaction cell to increase the fraction of alkyl nitrite photolysis, which will increase the amount of products formed without necessitating an increase in the precursor alkyl nitrite concentration.

3.4 CONCLUSIONS

We have obtained spectra of butoxy radical and pentoxy radical reaction pathways following the photolysis of the alkyl nitrite precursors at both 248 nm and 351 nm. We found that photolysis at 248 nm resulted in an unexpectedly high concentration of decomposition products. We suggest that excess energy in the alkoxy radicals following the photolysis of the nitrite precursor at 248 nm resulted in spontaneous decomposition of these molecules.

Spectra of n-butoxy and n-pentoxy radicals following precursor photolysis at 351 nm indicate the presence of a broad absorption centered at 3675 cm^{-1}. These absorptions were attributed to the -OH of the isomerization products. No formaldehyde absorption was observed for any of the butoxy or pentoxy radicals at 351 nm, supporting that the observation of this product at 248 nm was due to spontaneous decomposition as a result of excess internal energy in the butoxy radicals following the precursor photolysis.

The ratio of the rate constant for the reaction of the n-butoxy radical with O_2 versus its isomerization was obtained under conditions probing both the immediate formation of the isomerization product (10-20 microseconds after photolysis) and end-

product analysis (10 microseconds - 0.5 seconds after photolysis). The end-product analysis resulted in a value for k_{O_2}/ k_{isom} of $(4.0\pm0.1)*10^{-20}$ cm^3 $molec^{-1}$, while a value of $(3.6\pm1.4)*10^{-20}$ cm^3 $molec^{-1}$ was obtained when probing the isomerization product immediately after its formation. We have also placed an upper limit on the ratio of k_{O_2}/ k_{isom} for the n-pentoxy radical of $5.6*10^{-21}$ cm^3 $molec^{-1}$.

3.5 REFERENCES

[1] B. J. Finlayson-Pitts and J. N. Pitts Jr., Atmospheric Chemistry, Wiley-Interscience, 1986.

[2] R. C. Flagan and J. H. Seinfeld, Fundamentals of Air Pollution Engineering, Prentice Hall, New Jersey, 1988.

[3] J. H. Seinfeld and S. N. Pandis, Atmospheric Chemistry and Physics, Wiley-Interscience, New York, 1998.

[4] B. J. Finlayson-Pitts and J. N. Pitts Jr., *Science*, 276, 1045 (1997).

[5] R. P. Wayne, Chemistry of Atmospheres, Oxford University Press, 1991, p. 257.

[6] R. Atkinson, *Int. J. Chem. Kin.*, **29**, 99 (1997).

[7] H. Niki, P. D. Maker, C. M. Savage, L. P. Breitenbach, *J. Phys. Chem.*, **85**, 2698 (1981).

[8] E. S. C. Kwok, J. Arey, R. Atkinson, *J. Phys. Chem.*, **100**, 214 (1996).

[9] R. Atkinson and S. M. Aschmann, *Environ. Sci. Tech.*, **29**, 528 (1995).

[10] R. Atkinson, E. S. C. Kwok, J. Arey, S. M. Aschmann, *Farad. Discuss.*, **100**, 23 (1995).

[11] W. P. L. Carter, A. C. Lloyd, J. L. Spring, J. N. Pitts, Jr., *Int. J Chem. Kin.*, **XI**, 45 (1979).

[12] R. A. Cox, K. F. Patrick, S. A. Chant, *J. Am. Chem. Soc.*, **15 (5)**, 597 (1981).

[13] W. Deng, C. J. Wang, D. R. Katz, G. R. Gawinski, A. J. Davis, T. S. Dibble, *Chem. Phys. Lett.*, **330**, 5-6, 541 (2000)

[14] E. S. C. Kwok, R. Atkinson, J. Arey, *Environ. Sci. Tech.*, **30**, 3 (1996).

[15] H. Hein, A. Hoffmann, R. Zellner, *Phys. Chem. Chem. Phys.*, **1**, 3743 (1999).

[16] A. Heiss and K. Sahetchian, *Int. J. Chem. Kin.*, **28**, 531 (1996).

[17] T. P. W. Jungkamp, J. N. Smith, J. H. Seinfeld, *J. Phys. Chem. A*, **101**, 24, 4392 (1997).

[18] K. J. Hughes, P. D. Lightfoot, and M. J. Pilling, *Chem. Phys. Lett.*, **191**, 6, 581 (1992).

[19] Organic Syntheses, Collective Volume 2, p. 108, John Wiley & Sons, Inc., New York.

[20] J. Heicklen, *Adv. Photochem.*, **14**, 177 (1988).

[21] C. Fittschen, A. Frenzel, K. Imrik, P. Devolder, *Int. J. Chem. Kin.*, **31 (12)**, 860 (1999).

[22] L. Batt, M. W. M. Hisham, M. Mackay, *Int. J. Chem. Kin.*, **21**, 535 (1989).

[23] W. B. DeMore, S. P. Sander, D. M. Golden, R. F. Hampson, M. J. Kurylo, C. J. Howard, A. R. Ravishankara, C. E. Kolb, M. J. Molina, *Chemical Kinetics and Photochemical Data for Use in Stratospheric Modeling*, No. 11, Jet Propulsion Laboratory, Pasadena, CA (1997).

[24] G. R. McMillan, *J. Am. Chem. Soc.*, **83**, 3018 (1961).

[25] G. R. McMillan, *J. Phys. Chem.*, **68**, 116 (1964).

	reaction with O_2 k_{O2}, cm^3 $molec^{-1}$ s^{-1}	isomerization rate $k_{isom,}$ s^{-1}	decomposition rate k_{decomp}, s^{-1}
tert-butoxy	N. A.	N. A.	790
iso-butoxy	$8*10^{-15}$	N. A.	2100-2500
n-Butoxy	$1*10^{-16}$	1.6×10^5	580
n-pentoxy	$< 1*10^{-13}$	$> 1.0*10^5$	N. A.

Table 3.1. Summary of previous measurements of alkoxy reaction rates at 298K.

Rate of k_{isom}/k_{O2} (cm^3 $molec^{-1}$)	Conditions	Reference
$6.25*10^{-20}$	760 Torr, end-product	Carter et al. [11]
$(6.7\pm2.2)*10^{-20}$	760 Torr, end-product	Cox et al. [12]
$(5.2\pm0.5)*10^{-20}$	760 Torr, end-product	Niki et al. [7]
$(4.0\pm3.0)*10^{-19}$	38 Torr, monitoring NO and OH	Hein et al. [14]
$(4.0\pm0.1)*10^{-20}$	600 Torr, end-product	current work
$(3.6\pm1.4)*10^{-20}$	600 Torr, monitoring -OH peak at 3554 cm^{-1} 10-20 μs after the formation of n-butoxy	current work

Table 3.2. Summary of rate constants obtained for k_{isom}/k_{O2} for the n-butoxy radical.

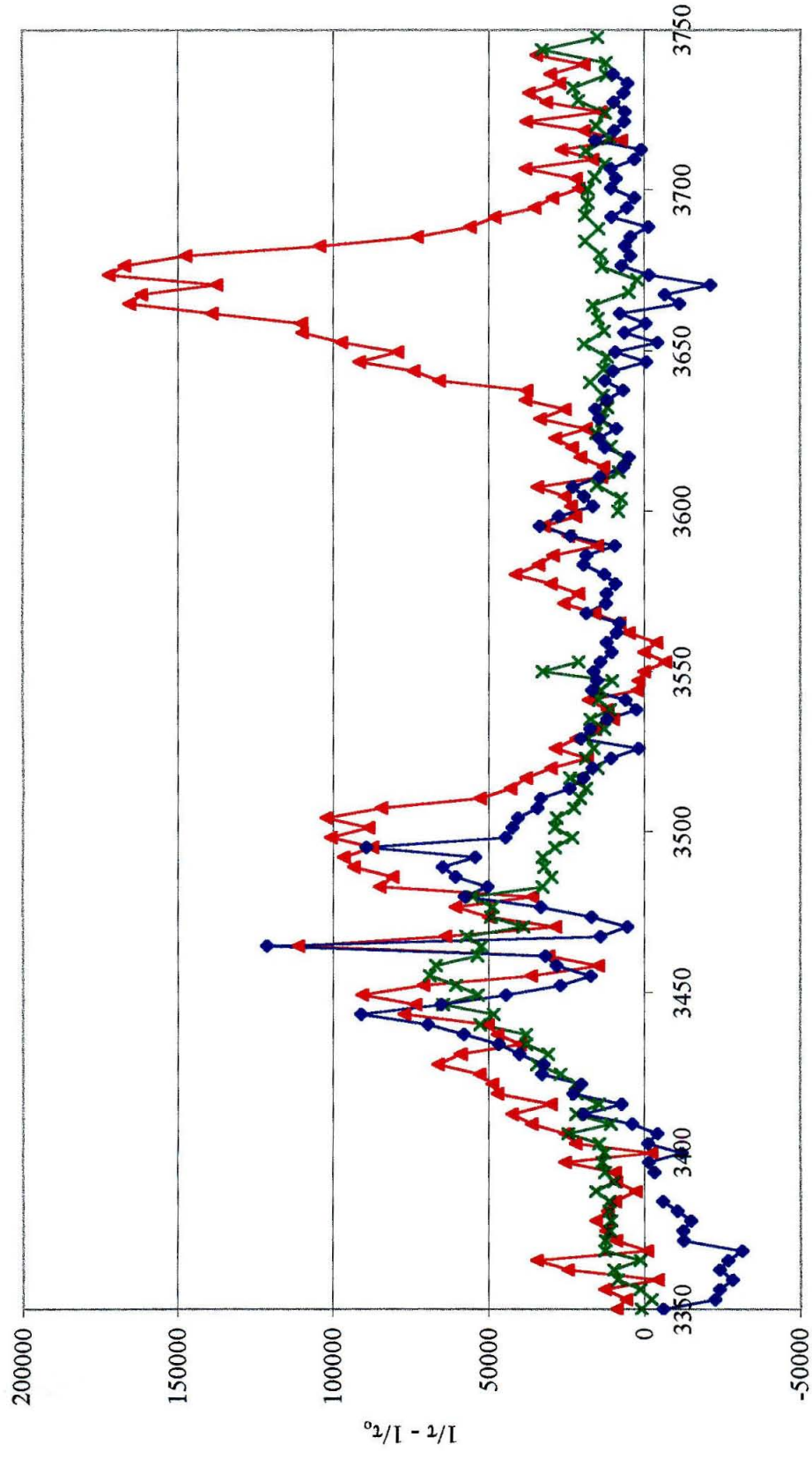

Figure 3.1. Spectra of butoxy radical reaction products in N_2 with the experiment running at 10 Hz and photolysis at 248 nm. The red data (triangles) corresponds to n-butoxy; the blue data (diamonds) corresponds to iso-butoxy, and the green data (x's) corresponds to tert-butoxy.

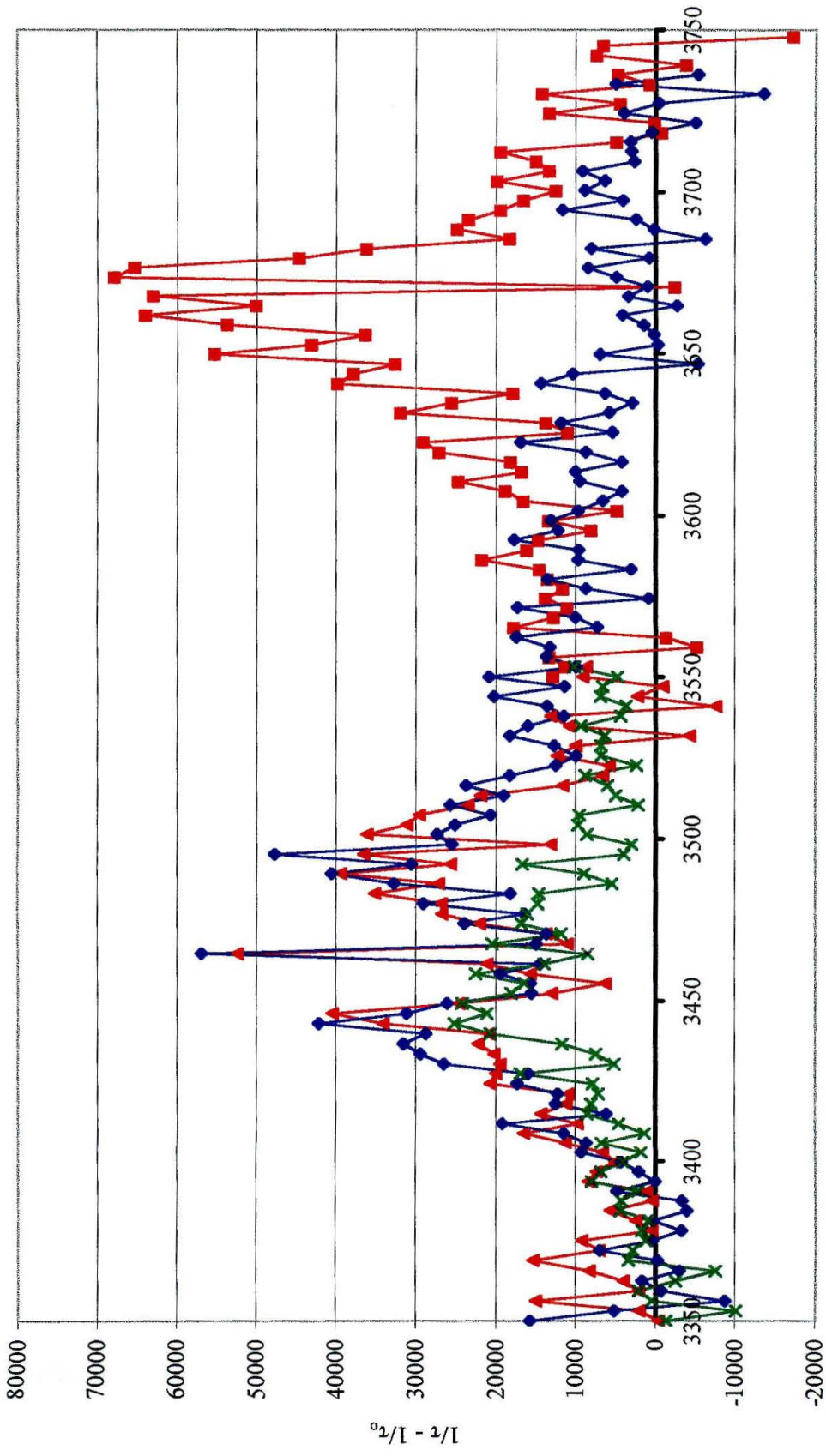

Figure 3.2. Spectra of butoxy radical reaction products in N_2 with the experiment running at 1 Hz and photolysis at 248 nm. The red data (triangles) corresponds to n-butoxy; the blue data (diamonds) corresponds to iso-butoxy, and the green data (x's) corresponds to tert-butoxy.

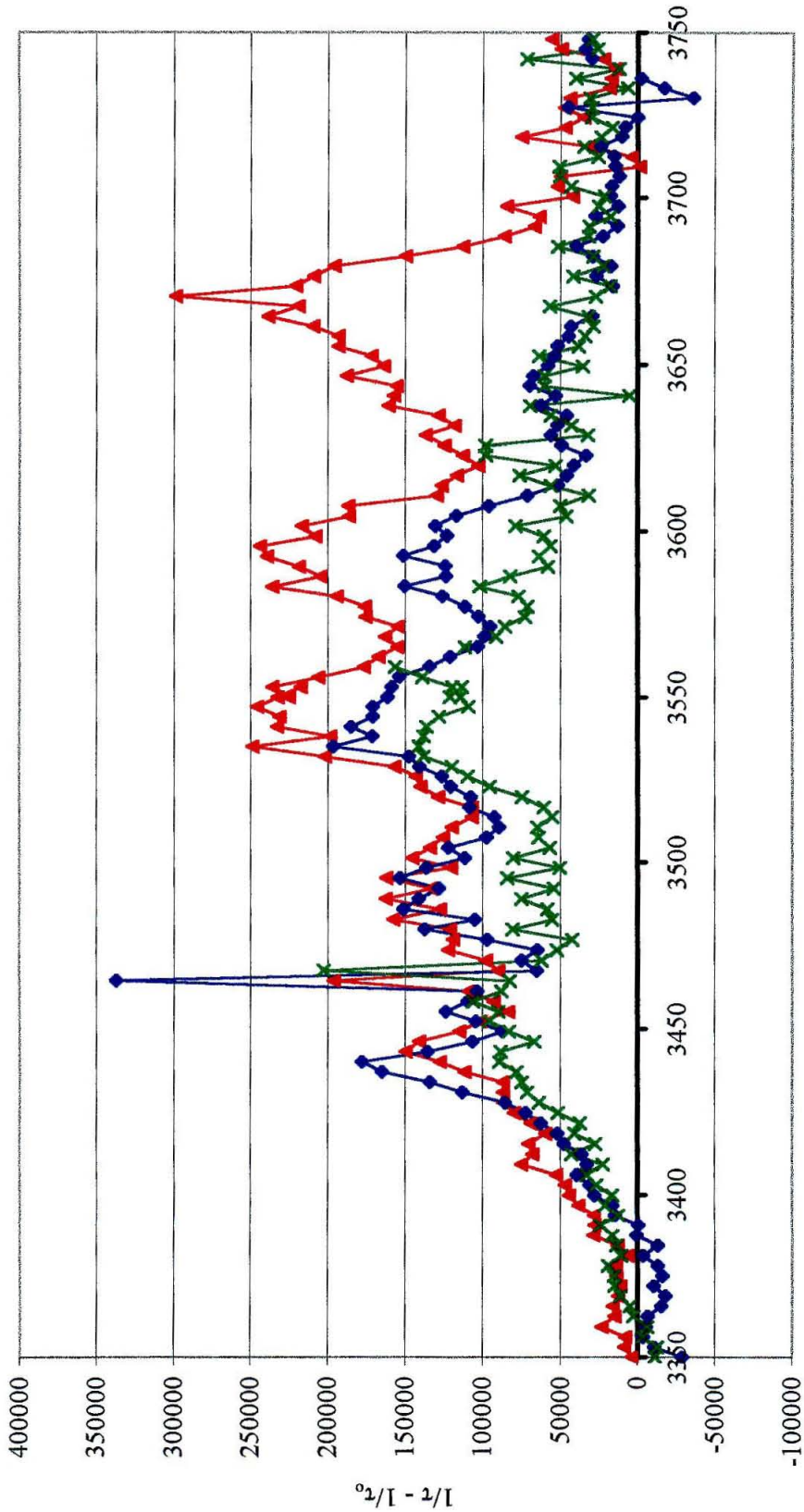

Figure 3.3. Spectra of butoxy radical reaction products in O_2 with the experiment running at 10 Hz and photolysis at 248 nm. The red data (triangles) corresponds to n-butoxy; the blue data (diamonds) corresponds to iso-butoxy, and the green data (x's) corresponds to tert-butoxy.

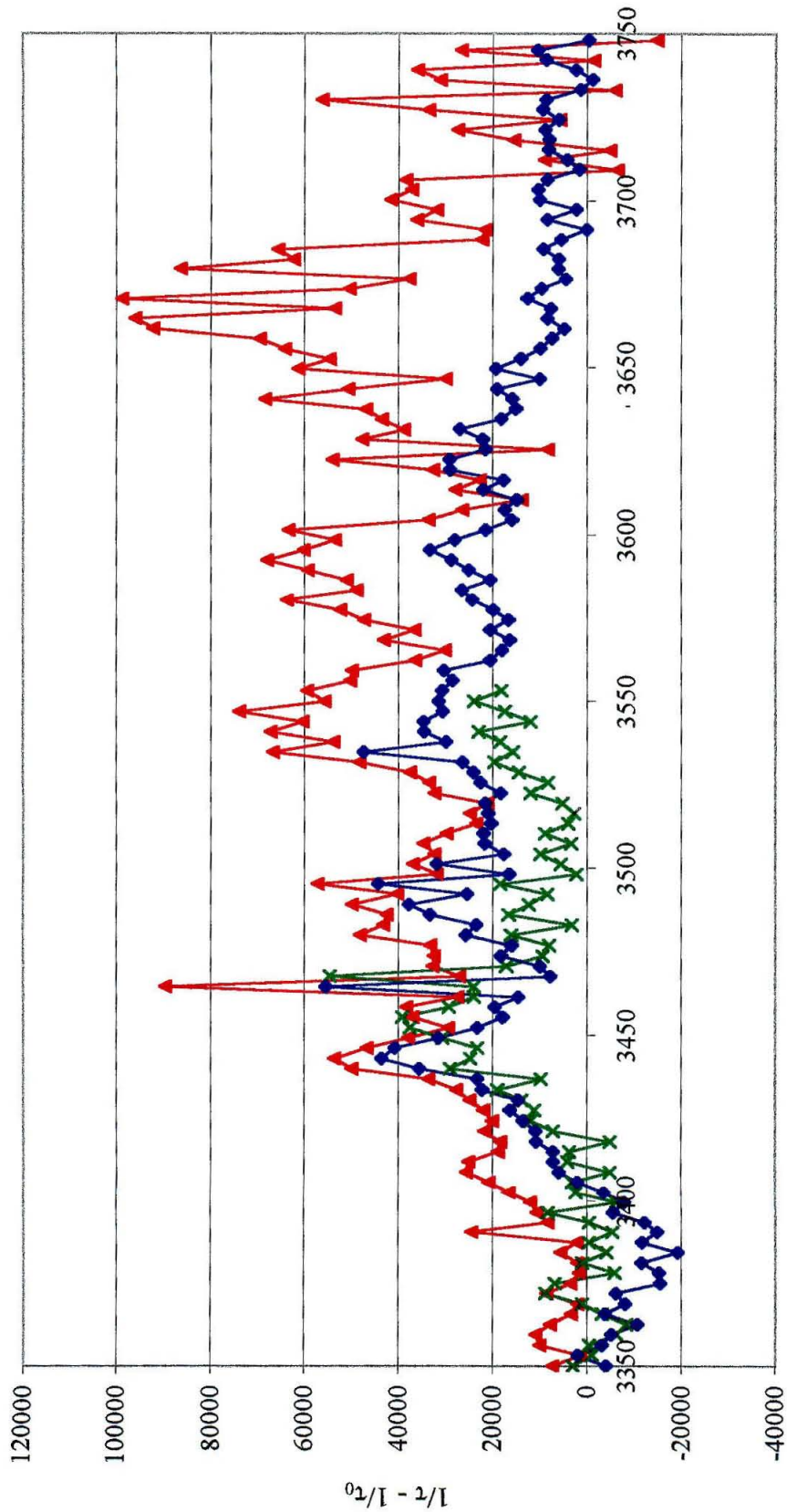

Figure 3.4. Spectra of butoxy radical reaction products in O_2 with the experiment running at 1 Hz and photolysis at 248 nm. The red data (triangles) corresponds to n-butoxy; the blue data (diamonds) corresponds to iso-butoxy, and the green data (x's) corresponds to tert-butoxy.

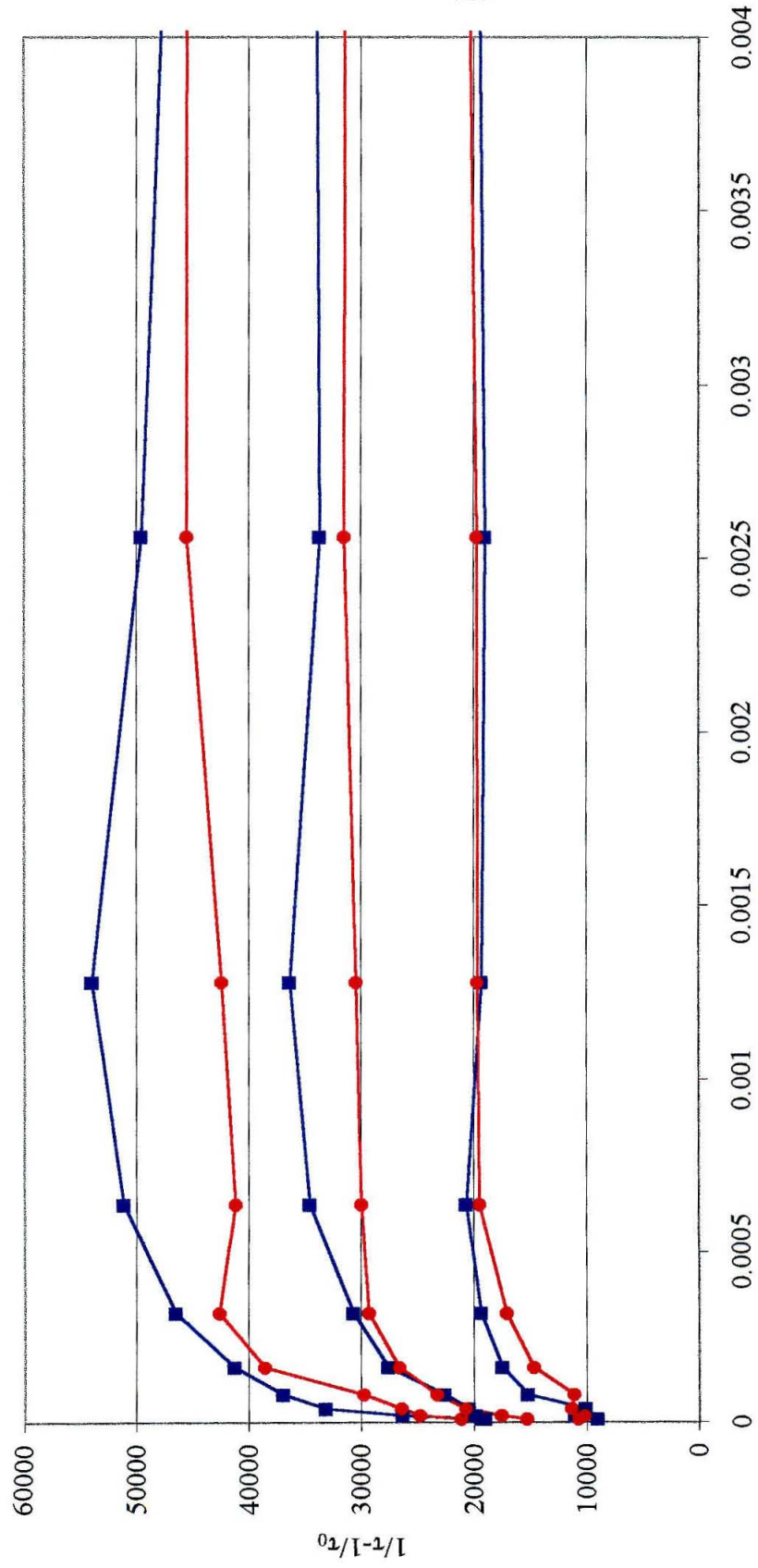

Figure 3.5. Signal at 3550 cm^{-1} and 3595 cm^{-1} as a function of time delay after the firing of the excimer laser at 248 nm. The blue data (squares) correspond to the peak at 3595 cm^{-1}, and the red data (circles) correspond to the peak at 3550 cm^{-1}. n-Butyl nitrite concentrations in order of increasing signal are $1*10^{15}$ molec/cc, $2*10^{15}$ molec/cc, and $3*10^{15}$ molec/cc.

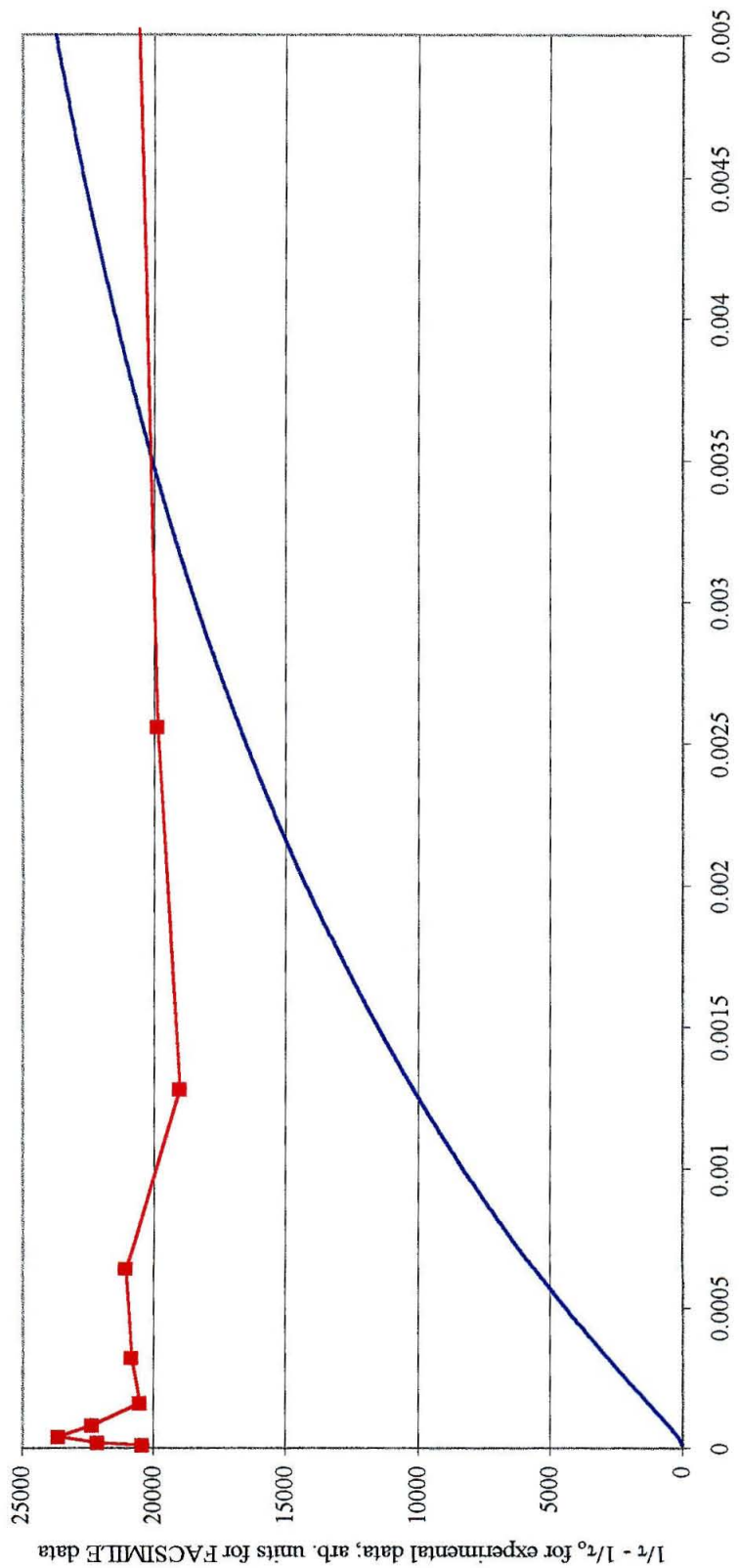

Figure 3.6. Time profile of formaldehyde formation from tert-butoxy in oxygen following photolysis of tert-butyl nitrite at 248 nm (red line with squares) compared to FACSIMILE model of formaldehyde formation following the addition of O_2 to CH_3 formed from the dissociation of tert-butoxy.

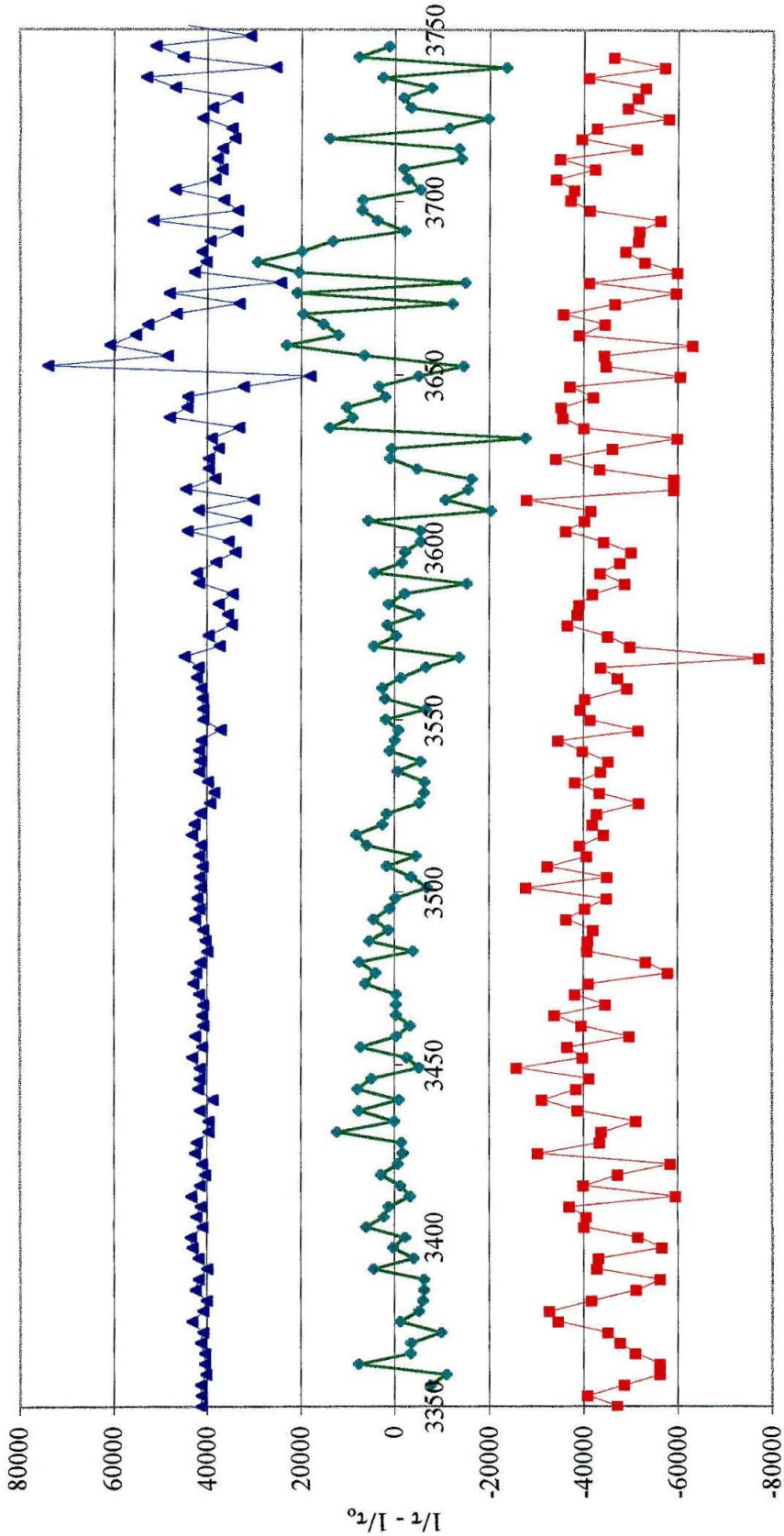

Figure 3.7. Spectra of butoxy and pentoxy radical reaction products in N_2 with the experiment running at 10 Hz and photolysis at 351 nm. The blue data (triangles) is n-pentoxy (zeroed at 40000 and reduced in size to match other spectra); the green data (diamonds) is n-butoxy, and the red data (squares) is iso-butoxy (zeroed at -40000).

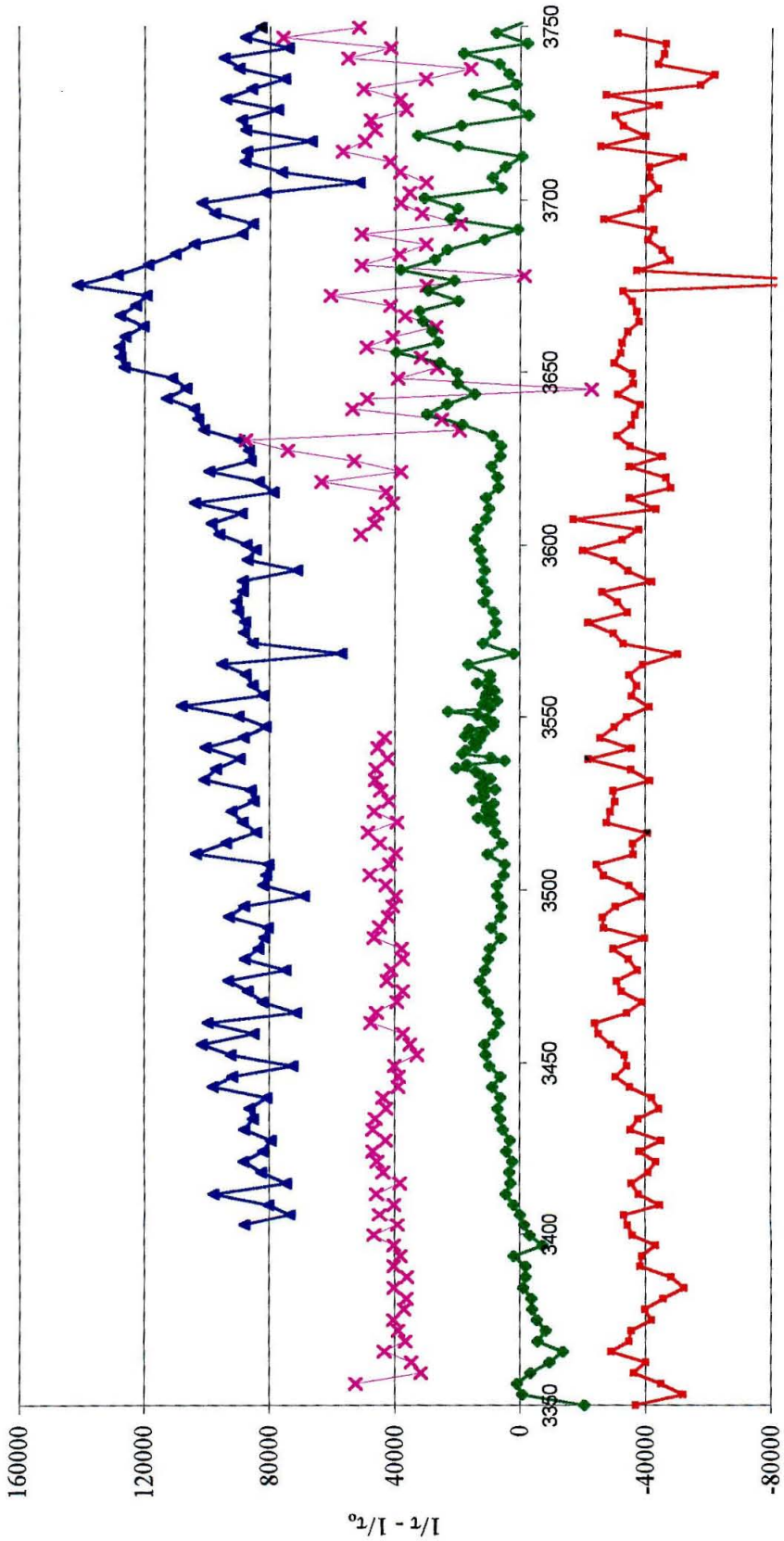

Figure 3.8. Spectra of butoxy and pentoxy radical reaction products in O_2 with the experiment running at 10 Hz and photolysis at 351 nm. The blue data (triangles) is n-pentoxy (zeroed at 80000); the pink data (x's) is tert-butoxy (zeroed at 40000); the green data (diamonds) is n-butoxy, and the red data (squares) is iso-butoxy (zeroed at -40000).

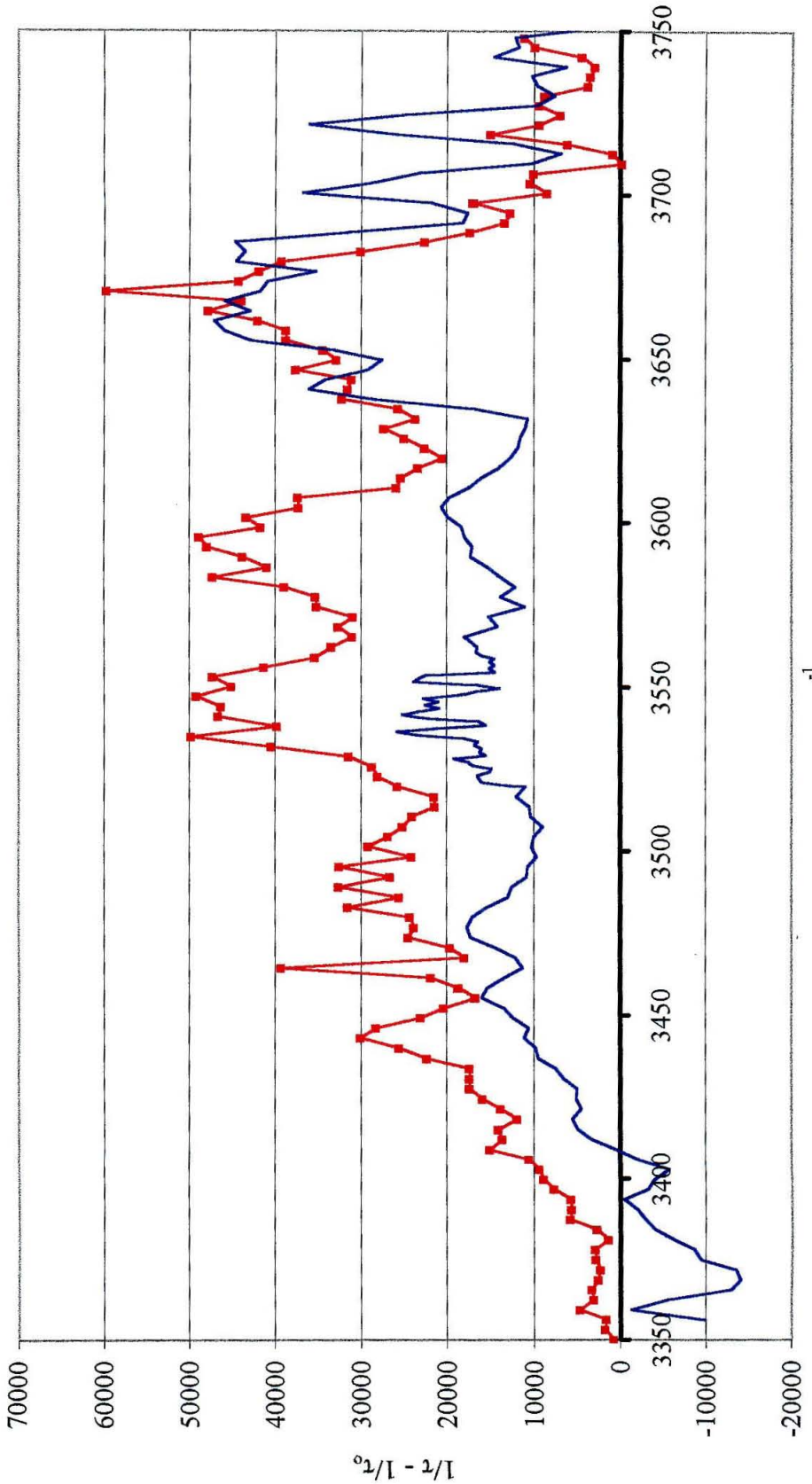

Figure 3.9. Comparison of n-butoxy radical in O_2 with 248 nm photolysis (red squares) and 351 nm photolysis (blue line).

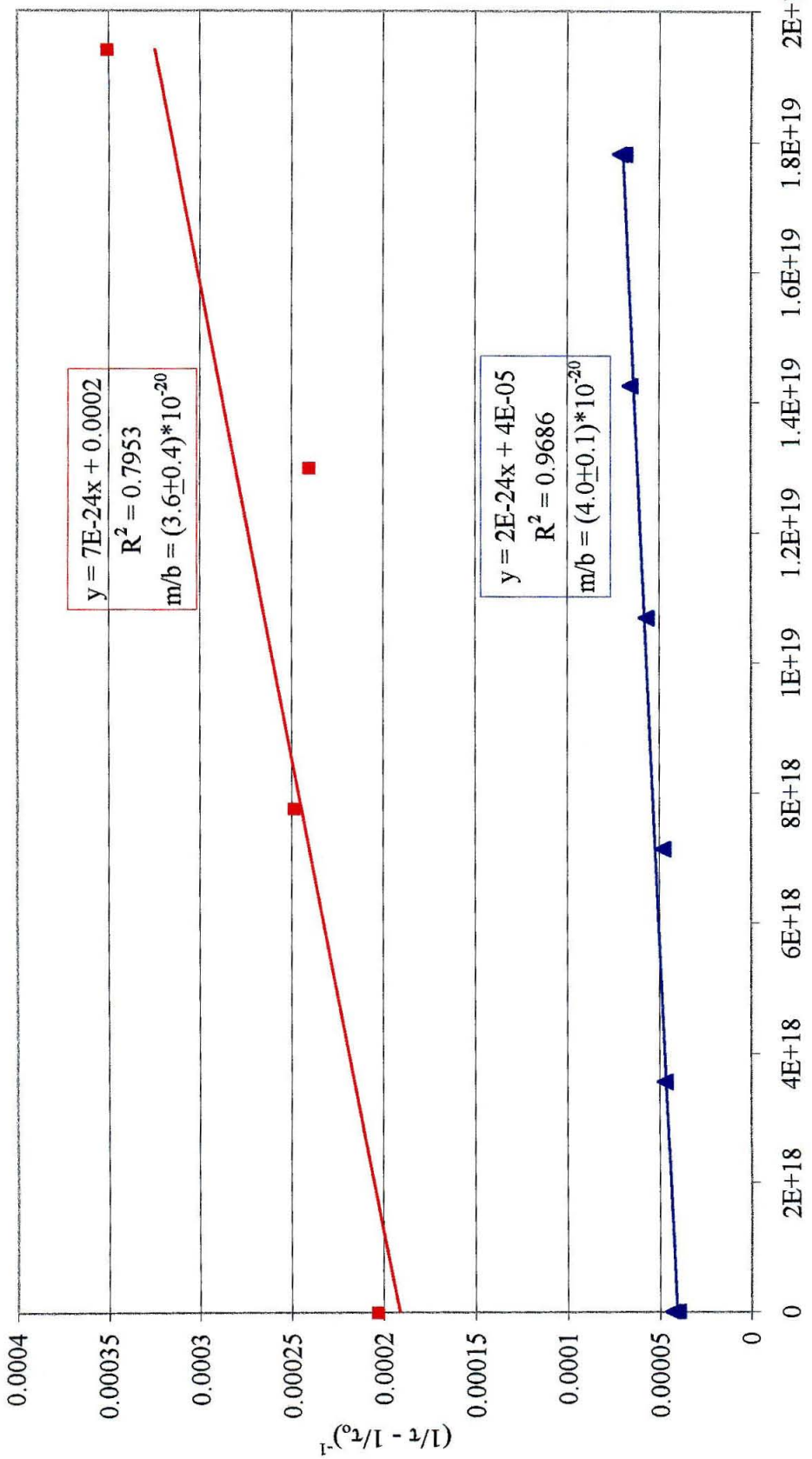

Figure 3.10. Plots of inverse signal at 3554 cm^{-1} as a function of O_2 concentration in the reaction cell. Red data points (squares) correspond to 1 Hz data, and blue data points (triangles) correspond to 10 Hz data.